



FALL/WINTER 2017
VOLUME 9, NUMBER 2

Print ISSN: 2152-4157
Online ISSN: 2152-4165

WWW.IJERI.ORG

International Journal of Engineering Research & Innovation

Editor-in-Chief: Mark Rajai, Ph.D.
California State University Northridge



Published by the
International Association of Journals & Conferences



www.ijeri.org

Print ISSN: 2152-4157
Online ISSN: 2152-4165



www.iajc.org

INTERNATIONAL JOURNAL OF ENGINEERING RESEARCH AND INNOVATION

ABOUT IJERI:

- IJERI is the second official journal of the International Association of Journals and Conferences (IAJC).
- IJERI is a high-quality, independent journal steered by a distinguished board of directors and supported by an international review board representing many well-known universities, colleges, and corporations in the U.S. and abroad.
- IJERI has an impact factor of **1.58**, placing it among an elite group of most-cited engineering journals worldwide.

OTHER IAJC JOURNALS:

- The International Journal of Modern Engineering (IJME)
For more information visit www.ijme.us
- The Technology Interface International Journal (TIIJ)
For more information visit www.tiij.org

IJERI SUBMISSIONS:

- Manuscripts should be sent electronically to the manuscript editor, Dr. Philip Weinsier, at philipw@bgsu.edu.

For submission guidelines visit
www.ijeri.org/submissions

TO JOIN THE REVIEW BOARD:

- Contact the chair of the International Review Board, Dr. Philip Weinsier, at philipw@bgsu.edu.

For more information visit
www.ijeri.org/editorial

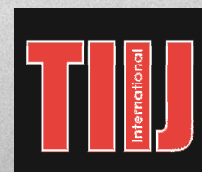
INDEXING ORGANIZATIONS:

- IJERI is indexed by numerous agencies. For a complete listing, please visit us at www.ijeri.org.

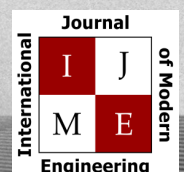
Contact us:

Mark Rajai, Ph.D.

Editor-in-Chief
California State University-Northridge
College of Engineering and Computer Science
Room: JD 4510
Northridge, CA 91330
Office: (818) 677-5003
Email: mrajai@csun.edu



www.tiij.org



www.ijme.us

INTERNATIONAL JOURNAL OF ENGINEERING RESEARCH AND INNOVATION

The INTERNATIONAL JOURNAL OF ENGINEERING RESEARCH AND INNOVATION (IJERI) is an independent and not-for-profit publication, which aims to provide the engineering community with a resource and forum for scholarly expression and reflection.

IJERI is published twice annually (fall and spring issues) and includes peer-reviewed research articles, editorials, and commentary that contribute to our understanding of the issues, problems, and research associated with engineering and related fields. The journal encourages the submission of manuscripts from private, public, and academic sectors. The views expressed are those of the authors and do not necessarily reflect the opinions of the IJERI editors.

EDITORIAL OFFICE:

Mark Rajai, Ph.D.
Editor-in-Chief
Office: (818) 677-2167
Email: ijmeeditor@iajc.org
Dept. of Manufacturing Systems
Engineering & Management
California State University-
Northridge
18111 Nordhoff Street
Northridge, CA 91330-8332

THE INTERNATIONAL JOURNAL OF ENGINEERING RESEARCH AND INNOVATION EDITORS

Editor-in-Chief:

Mark Rajai

California State University-Northridge

Associate Editors:

Paul Wilder

Vincennes University

Li Tan

Purdue University Northwest

Production Editor:

Philip Weinsier

Bowling Green State University-Firelands

Subscription Editor:

Morteza Sadat-Hossieny

Northern Kentucky University

Web Administrator:

Saeed Namyar

Advanced Information Systems

Manuscript Editor:

Philip Weinsier

Bowling Green State University-Firelands

Copy Editors:

Li Tan

Purdue University Northwest

Ahmad Sarfaraz

California State University-Northridge

Technical Editors:

Marilyn Dyrud

Oregon Institute of Technology

Publisher:

Bowling Green State University Firelands

TABLE OF CONTENTS

<i>Editor's Note: A Look Ahead to the 2018 IAJC Conference in Orlando, Florida</i>	3
Philip Weinsier, IJERI Manuscript Editor	
<i>Detection of High-Impedance Line-to-Ground Faults in Overhead Power Distribution Systems Using Wavelet and Fuzzy Logic</i>	5
Abayomi Ajofoyinbo, Texas Southern University	
<i>A Model for Stationary Platform Placement Problems in Military Surveillance</i>	18
Nebil Buyurgan, Missouri State University; Nabil Lehlou, Womply/Oto Analytics; Kevin M. Hubbard, Missouri State University	
<i>Influence of Build Orientation and Heat Treatment on Tensile Strength of EOS Maraging Steel MS1</i>	28
Jennifer G. Michaeli, Old Dominion University; Amit Kulkarni, Old Dominion University; Roman Roxas, Old Dominion University	
<i>Pattern Learning for Economical Prosthetic Hands using Leap Motion Sensors</i>	35
Wutthigrai Boonsuk, Eastern Illinois University; Noah C Przygoda, Eastern Illinois University	
<i>Improving the Cooling Efficiency of Pre-Existing Residential Air Conditioning Systems</i>	41
Ming Li, University of Michigan-Flint; Ayo Abatan, Miami University; Derick Robinson, Miami University; Jeff Weller, Miami University; Matthew Bello, Miami University	
<i>Using Nanoparticles to Modify the Surface Energy of High-Density Polyethylene Films</i>	47
Rex C. Kanu, Purdue Polytechnic Institute; Thomas Spotts, Ball State University	
<i>Instructions for Authors: Manuscript Requirements</i>	52



6TH IAJC INTERNATIONAL CONFERENCE

OCTOBER 11-14, 2018 – ORLANDO, FLORIDA

The leading indexed high-impact-factor conference on engineering and related technologies.

Our Hotel—Embassy Suites



Our 2018 Tour Plan—Disney Underground



Our Previous Tour—NASA's Kennedy Space Center



Editorial Review Board Members

Mohammed Abdallah	State University of New York (NY)	Gengchen Liu	University of California-Davis (CA)
Nasser Alaraje	Michigan Tech (MI)	Guoxiang Liu	University of North Dakota (ND)
Ammar Al-Farga	University of Jiangnan (CHINA)	Louis Liu	University of New Orleans (LA)
Aly Mousaad Aly	Louisiana State University (LA)	Peng Liu	Washington State University (WA)
Paul Akangah	North Carolina A&T State University (NC)	Mani Manivannan	ARUP Corporation
Lawal Anka	Zamfara AC Development (NIGERIA)	G.H. Massiha	University of Louisiana (LA)
Jahangir Ansari	Virginia State University (VA)	Jim Mayrose	Buffalo State College (NY)
Kevin Berisso	Ohio University (OH)	Thomas McDonald	University of Southern Indiana (IN)
Pankaj Bhambri	Guru Nanak Dev Engineering (INDIA)	David Melton	Eastern Illinois University (IL)
Water Buchanan	Texas A&M University (TX)	Shokoufeh Mirzaei	Cal State Poly Pomona (CA)
John Burningham	Clayton State University (GA)	Bashir Morshed	University of Memphis (TN)
Shaobiao Cai	Penn State University (PA)	Sam Mryyan	Excelsior College (NY)
Vigyana Chandra	Eastern Kentucky University (KY)	Jessica Murphy	Jackson State University (MS)
Isaac Chang	Illinois State University (IL)	Wilson Naik	University of Hyderabad (INDIA)
Shu-Hui (Susan) Chang	Iowa State University (IA)	Arun Nambiar	California State University Fresno (CA)
Bin Chen	Purdue University Northwest (IN)	Ramesh Narang	Indiana University-Purdue University (IN)
Wei-Yin Chen	University of Mississippi (MS)	Anand Nayyar	Institute Management and Tech (INDIA)
Rigoberto Chinchilla	Eastern Illinois University (IL)	Aurenice Oliveira	Michigan Tech (MI)
Phil Cochrane	Indiana State University (IN)	Reynaldo Pablo	Indiana University-Purdue University (IN)
Emily Crawford	Southern Wesleyan University (SC)	Basile Panoutsopoulos	Community College of Rhode Island (RI)
Brad Deken	Southeast Missouri State University (MO)	Shahera Patel	Sardar Patel University (INDIA)
Z.T. Deng	Alabama A&M University (AL)	Jose Pena	Purdue University Calumet (IN)
Sagar Deshpande	Ferris State University (MI)	Karl Perusich	Purdue University (IN)
David Domermuth	Appalachian State University (NC)	Thongchai Phairoh	Virginia State University (VA)
Dongliang Duan	University of Wyoming (WY)	Huyu Qu	Honeywell Corporation
Marilyn Dyrud	Oregon Institute of Technology (OR)	John Rajadas	Arizona State University (AZ)
Mehran Elahi	Elizabeth City State University (NC)	Vijaya Ramnath	Sri Sairam Engineering College (CHENNAI)
Ahmed Elsayy	Tennessee Technological University (TN)	Desire Rasolomampionona	Warsaw University of Tech (POLAND)
Rasoul Esfahani	DeVry University (OH)	Mohammad Razani	New York City College of Tech (NY)
Dominick Fazarro	Sam Houston State University (TX)	Sangram Redkar	Arizona State University-Poly (AZ)
Ignatius Fomunung	University of Tennessee Chattanooga (TN)	Michael Reynolds	University of Arkansas Fort Smith (AR)
Ahmed Gawad	Zagazig University EGYPT	Nina Robson	California State University-Fullerton (CA)
Daba Gedafa	University of North Dakota (ND)	Marla Rogers	Wireless Systems Engineer
Mohsen Hamidi	Utah Valley University (UT)	Dale Rowe	Brigham Young University (UT)
Mamoon Hammad	Abu Dhabi University (UAE)	Karen Ruggles	DeSales University (PA)
Gene Harding	Purdue Polytechnic (IN)	Anca Sala	Baker College (MI)
Youcef Himri	Safety Engineer in Sonelgaz (ALGERIA)	Alex Sergeev	Michigan Technological University (MI)
Xiaobing Hou	Central Connecticut State University (CT)	Hiral Shah	St. Cloud State University (MN)
Shelton Houston	University of Louisiana Lafayette (LA)	Siles Singh	St. Joseph University Tanzania (AFRICA)
Kun Hua	Lawrence Technological University (MI)	Ahmad Sleiti	University of North Carolina Charlotte (NC)
Ying Huang	North Dakota State University (ND)	Jiahui Song	Wentworth Institute of Technology (MA)
Dave Hunter	Western Illinois University (IL)	Yuyang Song	Toyota Corporation
Christian Hyeng	North Carolina A&T University (NC)	Carl Spezia	Southern Illinois University (IL)
Pete Hylton	Indiana University Purdue (IN)	Michelle Surerus	Ohio University (OH)
Ghassan Ibrahim	Bloomsburg University (PA)	Jalal Taheri	Bostan Abad Islamic Azad University (IRAN)
John Irwin	Michigan Tech (MI)	Li Tan	Purdue University Northwest (IN)
Toqeer Israr	Eastern Illinois University (IL)	Harold Terano	Camarines Sur Polytechnic (NABUA)
Sudershan Jetley	Bowling Green State University (OH)	Sanjay Tewari	Louisiana Tech University (LA)
Rex Kanu	Ball State University (IN)	Vassilios Tzouanas	University of Houston Downtown (TX)
Tolga Kaya	Central Michigan University (MI)	Jeff Ulmer	University of Central Missouri (MO)
Satish Ketkar	Wayne State University (MI)	Mihaela Vorvoreanu	Purdue University (IN)
Manish Kewalramani	Abu Dhabi University (UAE)	Phillip Waldrop	Georgia Southern University (GA)
Tae-Hoon Kim	Purdue University Northwest (IN)	Abraham Walton	Purdue University (IN)
Chris Kluse	Bowling Green State University (OH)	Haoyu Wang	Central Connecticut State University (CT)
Doug Koch	Southeast Missouri State University (MO)	Liangmo Wang	Nanjing University of Science/Tech (CHINA)
Ognjen Kuljaca	Brodarski Institute (CROATIA)	Boonsap Witchayangkoon	Thammasat University (THAILAND)
Chakresh Kumar	Uttar Pradesh Tech University (INDIA)	Alex Wong	Digilent Inc.
Zaki Kuruppallil	Ohio University (OH)	Shuju Wu	Central Connecticut State University (CT)
Edward Land	Johns Hopkins Medical Institute	Baijian "Justin" Yang	Ball State University (IN)
Jane LeClair	Excelsior College (NY)	Eunice Yang	University of Pittsburgh Johnstown (PA)
Shiyong Lee	Penn State University Berks (PA)	Mijia Yang	North Dakota State University (ND)
Soo-Yen Lee	Central Michigan University (MI)	Xiaoli (Lucy) Yang	Purdue University Northwest (IN)
Solomon Leung	Idaho State University (ID)	Faruk Yildiz	Sam Houston State University (TX)
Chao Li	Florida A&M University (FL)	Yuqiu You	Morehead State University (KY)
Jimmy Linn	Eastern Carolina University (NC)	Pao-Chiang Yuan	Jackson State University (MS)
Dale Litwhiler	Penn State University (PA)	Jinwen Zhu	Missouri Western State University (MO)

DETECTION OF HIGH-IMPEDANCE LINE-TO-GROUND FAULTS IN OVERHEAD POWER DISTRIBUTION SYSTEMS USING WAVELET AND FUZZY LOGIC

Abayomi Ajofoyinbo, Texas Southern University

Abstract

In a review of the literature, researchers have developed several techniques for line-to-ground fault identification, including using discrete wavelet transform (DWT) to separate measured signals into frequency ranges and compute the energy content of wavelet coefficients for fault classification. In stable utility power systems interconnected by power grids, frequency variations are uncommon. For single-frequency signals such as current and voltage signals in 3-phase power systems, the application of DWT is associated with redundant decompositions. In this paper, the author addresses this concern, among others, via a presentation of a new detection methodology for high-impedance line-to-ground faults in overhead power distribution systems using wavelet and fuzzy logic. Net time-average power of wavelet and current signals were computed at specific time intervals as a basis for identifying fault current. Depending on the difference between computed net power pre-occurrence and during-occurrence of line-to-ground faults, the measured current value was either forwarded to the fuzzy logic module or the traditional fault-current detection module. A fuzzy logic scheme was integrated into the detection system design because of the uncertainty in current signals and to provide capability for effective tripping of the protective system. Also presented in this paper is the detection system design, including: (i) current transformer, (ii) current sensor, (iii) microcontroller, (iv) relay driver chip, (v) protective relays, and (vi) circuit breaker. The effectiveness of this detection system was tested via a numerical analysis implemented in MATLAB and fuzzy logic toolbox. It was found that the detection scheme could effectively detect high-impedance line-to-ground faults at all levels of fault current and isolate-affected segments from the rest of the power distribution system.

Introduction

Electrical power is usually generated at voltages greater than 10 kV and transmitted over long distances at voltages ranging from 200 kV to over 700 kV. Local power distribution to neighborhoods (homes, industries, etc.) goes through transmission substations and is transmitted over short dis-

tances at voltages ranging from 5 kV to 13 kV, which is subsequently reduced to 120V (or 240V) for safety at individual user locations. Protective systems in power networks consist mainly of relays and their associated circuit breakers. Protective relays detect faults in power systems through current and voltage transformers, and subsequently operate circuit breakers to isolate the fault section from the rest of the power distribution system. High-impedance line-to-ground faults (HIF) in overhead power distribution systems are often caused by tree branches touching conductors and conductors losing supports and falling on poorly conductive surfaces, thereby making unwanted electrical contact with, for example, the road surface, sidewalk, or some other surface that restricts the flow of fault current to a level that is much smaller than detection thresholds of traditional fault-detection devices.

Reliable detection of these high-impedance line-to-ground faults has remained a real challenge. Without timely correction, high-impedance line-to-ground faults can indeed be hazardous to human life and property. A line-to-ground fault is characterized by a decaying current sinusoidal signal. The methodology presented in this paper detects occurrence of such a signal by comparing the time-average pre-fault and during-fault power of current and wavelet signals. A wavelet is defined as a waveform of effectively limited duration [1]. Whereas a fuzzy set is defined as a class of objects with a continuum of grades of membership and characterized by a membership function that assigns to each object a membership grade between 0 and 1, fuzzy logic defines modes of reasoning that are imprecise rather than precise. Fuzzy logic is integrated into this detection system design because of the uncertainty in current signals and to provide effective tripping of circuit breakers.

Review of Related Literature

In a review of the literature, the author found that researchers have investigated challenges associated with the detection of faults and protection of power transmission and distribution networks. For example, Prasada and Srinivasua [2] presented a fault-detection method for protection of transmission lines using root-mean-square values of 3-phase instantaneous power at both sending and receiving ends. An

adaptive distance protection scheme was presented by Ma et al. [3] to improve the performance of the conventional distance protection scheme under a high-resistance fault. Majidi et al. [4] presented a methodology for fault location in distribution networks using compressive sensing. During-fault and pre-fault voltages were measured by smart meters along the feeders. The voltage sag vector and impedance matrix produced a current vector that was sparse enough with one nonzero element. This element corresponds to the bus at which a fault occurred. Bains and Dadash Zadeh [5] investigated the problem of offline fault location using a technique based on prony analysis and discrete Fourier transform to estimate voltage and current phasors. Prony analysis extends Fourier analysis by directly estimating the frequency, damping, strength, and relative phase of the modal components present in a recorded signal.

Alyami [6] examined transient measures and their effects in transmission lines and the overall stability of the power system. In an interesting contribution, Kumar et al. [7] presented a method for detecting high-impedance faults in radial distribution systems. Magnitudes of third- and fifth-harmonic components of voltages and currents were used as a feature vector for fault discrimination. This methodology uses a back propagation neural network as a classifier for identifying high-impedance arc-type faults. Khandare and Khatri [8] analyzed and modeled high-impedance faults using MATLAB's Simulink tool for deploying proper protection schemes in distribution systems. Milioudis et al. [9] extended previous work aimed at achieving detection and location of high-impedance faults in multi-conductor overhead distribution networks utilizing power-line communication devices. Moreover, Sarvi and Torabi [10] presented a method for determination of fault location and fault type in power distribution systems by neural networks. This method uses neural networks to classify and locate normal and composite types of faults, such as phase-to-earth, two-phases-to-earth, and phase-to-phase. Nowicki et al. [11] conducted a series of experiments that simulated the most common high-impedance faults. Milioudis et al. [12] utilized power-line communication technology to offer both high-impedance fault detection and location.

In another contribution, Milioudis et al. [13] presented a method for dealing with the exact location of high-impedance faults using an installed power-line communication system. This method injects a specific test signal into the power grid after a high-impedance fault alarm is set. Using impulse responses that are recorded by the power-line communication devices, the location of the fault can be determined. According to Zadeh [14], fuzzy logic is based on the notion of fuzzy-set theory, which provides a natural way of dealing with problems in which the source of imprecision

is the lack of sharply defined criteria of class membership rather than the presence of randomness. Fuzzy-set theory and fuzzy logic have proven to have a wide scope of applicability in engineering, medicine, biomedical instrumentation, decision analysis, etc.

For example, Olunloyo et al. [15] developed an embedded fuzzy controller for the case of triangular and Gaussian membership functions. In another interesting contribution, Ajofoyinbo and Olowokere [16] developed a fuzzy control model for structural health monitoring of civil infrastructure systems. Kamel [17] developed a fuzzy modeling and control strategy of random disturbances, based on an estimated margin of variations in state variables of a studied power system affected by such random disturbances. Moreover, Jain et al. [18] applied artificial neural network (ANN) techniques for detection of single line-to-ground faults and fault-type classification on double-circuit transmission lines with remote-end in-feed. The technique takes into account the effects of mutual coupling, high fault resistance, varying fault location, fault inception angle, and remote-source in-feed. In an interesting contribution, a fuzzy logic-based algorithm and discrete wavelet transform (DWT) was utilized by Jamil et al. [19] to identify various faults in an electrical distribution system for an unbalanced distribution electrical power system. DWT was used to calculate the changes in energy of measured signals that were then used as inputs into the fuzzy logic system.

Badran et al. [20] presented an approach for detecting and classifying the HIF in distribution systems by using DWT-based pattern recognition for extracting the current signals. The simulation results showed that this approach could detect and classify the fault location and the fault type. Furthermore, Mahajan and Sharma [21] reviewed the most recent techniques used for transmission line protection, including artificial neural networks (ANN), fuzzy logic adaptive neuro-fuzzy, wavelet, genetic algorithm, and phasor measurement unit (PMU). According to this study, 80%-90% of faults occur on the transmission or distribution line, with the rest occurring on substation equipment and bus bars combined.

The percentage of occurrence of various types of faults are given as follows: single-line-to-ground fault (70%-80%), line-to-line-to-ground fault (10%-17%), line-to-line fault (8%-10%), and three-phase fault (3%). Occurrence (and detection) of high-impedance line-to-ground faults on any one phase in a 3-phase power distribution system is a sufficient condition for triggering a circuit breaker in order to isolate the affected section from the rest of a power distribution system.

Research Methodology and Problem Solution

Line-to-Ground Fault Detection Scheme

In a balanced 3-phase power transmission and distribution system, the voltage of each phase is displaced from the others by 120° ; and three currents exist simultaneously, one in each phase. The current in each line is equal in amplitude and frequency, and is 120° out-of-phase with the other two line currents. An unbalanced load on a single-phase in a 3-phase electrical power distribution system is the main cause of unbalanced voltages or distribution currents. A power system imbalance affects the magnitude and phase angle of current waveform. Since the detection scheme is deployed on each of the three phases, abnormality in distribution current on any of the phases of an unbalanced power system is also detected. This means that the detection scheme can detect single line-to-ground, double line-to-ground, and three line-to-ground faults, when implemented on all phases of a power distribution system. It should be noted that, during a line-to-ground fault (or earth fault), current flows into the earth (or other surfaces that restrict the flow of fault currents).

In Figure 1, $i(t)$ is the current signal, $\psi(t)$ is the wavelet signal, and k_i represents points in time. In addition, P_a and P_ψ represent time-average power of the current and wavelet signals, respectively, while k_i to k_{i+1} denote time intervals.

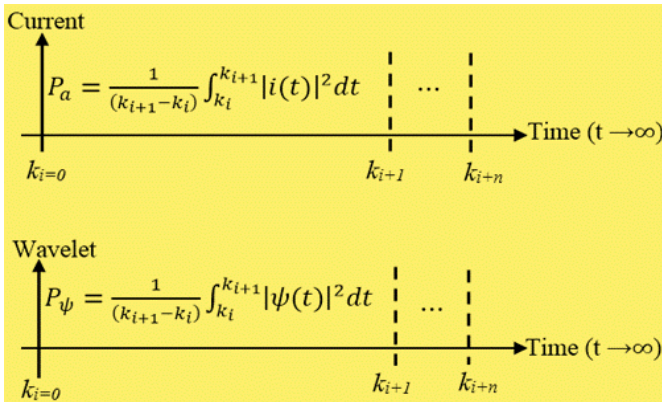


Figure 1. Sampling and Computation of Time-Average Power of Current and Wavelet Signals

The time-average power of the measured current and wavelet signals are determined for the time interval k_i to k_{i+1} , and the net time-average power that represents the difference between these two values, is computed. This is a one-time baseline net time-average power, which is computed during normal power-line operation and stored as a refer-

ence value. The time-average power of measured current signals is assumed not to change significantly in relation to line loadings during normal power-line operation. Subsequent net time-average power of measured current signals is computed, and the difference between this calculated value and the stored baseline value is determined. This difference, the decision-input, is the basis for operation of the fuzzy logic module. Figure 2 shows the flowchart for the fault detection system. If the difference is positive (i.e., the computed net time-average power is less than the stored threshold value) then a line-to-ground fault is detected and the measured current value is forwarded to the fuzzy logic-based control module for further processing. Depending on the value of the measured current, the fuzzy logic-based control module determines whether or not the applicable circuit breaker should be operated to isolate the affected segment.

The flowchart of Figure 2 for the line-to-ground detection system shows the time-domain current signals $i_1(t)$, $i_2(t)$, and $i_3(t)$ for phases 1, 2, and 3, respectively. Moreover, P_{i1} , P_{i2} , and P_{i3} denote the time-average power of current signal in phases 1, 2, and 3, respectively, while P_{n1} , P_{n2} , and P_{n3} denote net time-average power of current signal in phases 1, 2, and 3, respectively. P_w represents time-average power of the wavelet signal. The indexing variable n ranges from zero to infinity.

High-Impedance Line-to-Ground Fault-Detection System Design

Figure 3 shows the design of a high-impedance line-to-ground fault detection system. The detection system design is comprised of instrument transformers (current and voltage transformers), the ACS712 current sensor module [22], a ULN2003 relay driver chip [23], along with a microcontroller, relays, and circuit breaker. Instrument transformers step down the voltage or current to a standardized value, when voltage or current becomes too large to be conveniently used by a measurement, control, or protection device (or system). A current transformer, CT, transforms the current on the power system from a large primary value to a safe secondary value in which the secondary current is proportional (in ratio) to the primary current. In the CT, the primary winding is connected in series with the conductor carrying the current to be measured or controlled. Secondary windings of the CT have a standard rating of 5A. Moreover, a voltage transformer, VT, transforms the voltage on the power system from a large primary value to a safe secondary value at a ratio proportional to the primary value. The secondary voltage of a VT is usually 69.3V for relaying and 120V for metering [24].

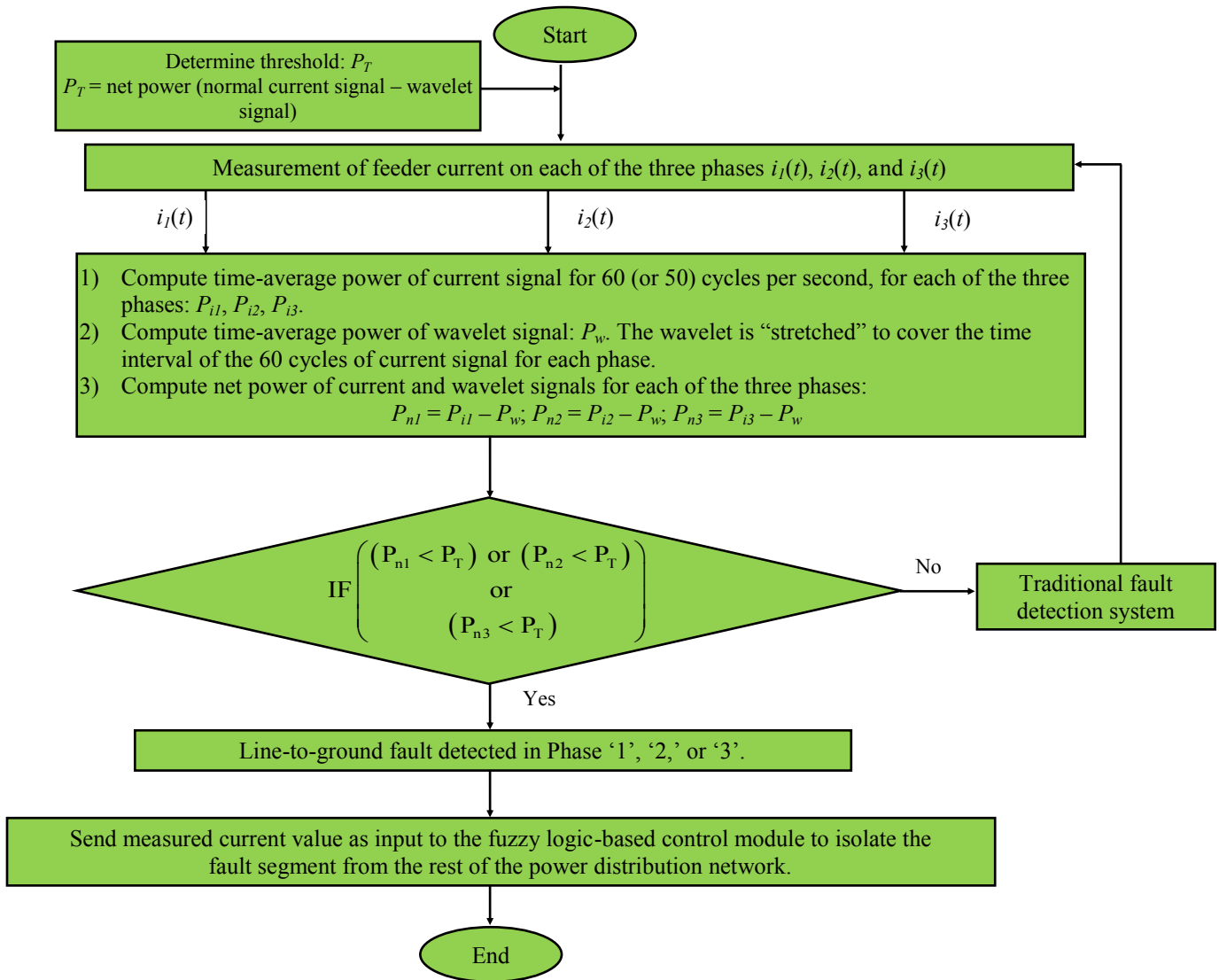


Figure 2. Detection System Design Flowchart

In Figure 3, the power supply to the detection system is derived from the substation direct current (DC) battery that supplies 125/250 Vdc. To meet the power requirements of the current sensor, microcontroller, and relays, appropriate DC-DC converters are deployed to deliver 12 Vdc and 5 Vdc. For example, an SEL-9321 low-voltage DC power supply converts 125/250 Vdc to 5 Vdc [25], or a Wilmore DC-DC converter converts 130 Vdc to 12 Vdc [26]. The ACS712-05B current sensor module is an analog input that provides accurate measurement of AC and DC currents. This current sensor module can handle AC or DC currents up to 5A and operates at 5V. Manufacturers of current sensors incorporate technique for addressing current overloading in the system designs, thereby preventing current sen-

sors from being damaged. The secondary windings of the CT connects to the current sensor module, and a single analog output signal from the current sensor module to the microcontroller provides the sensor's readings. The analog output signal from the current sensor is proportional to the amount of measured current.

Digital levels (low or high) from the microcontroller unit to one of the digital input pins of the relay driver chip drive Relay1, which operates Switch_S of the tripping circuit (see Figure 3). It is important to note that the signal on an output pin of the relay driver chip, ULN2003, is inverted from the signal on the corresponding input pin of the relay driver chip.

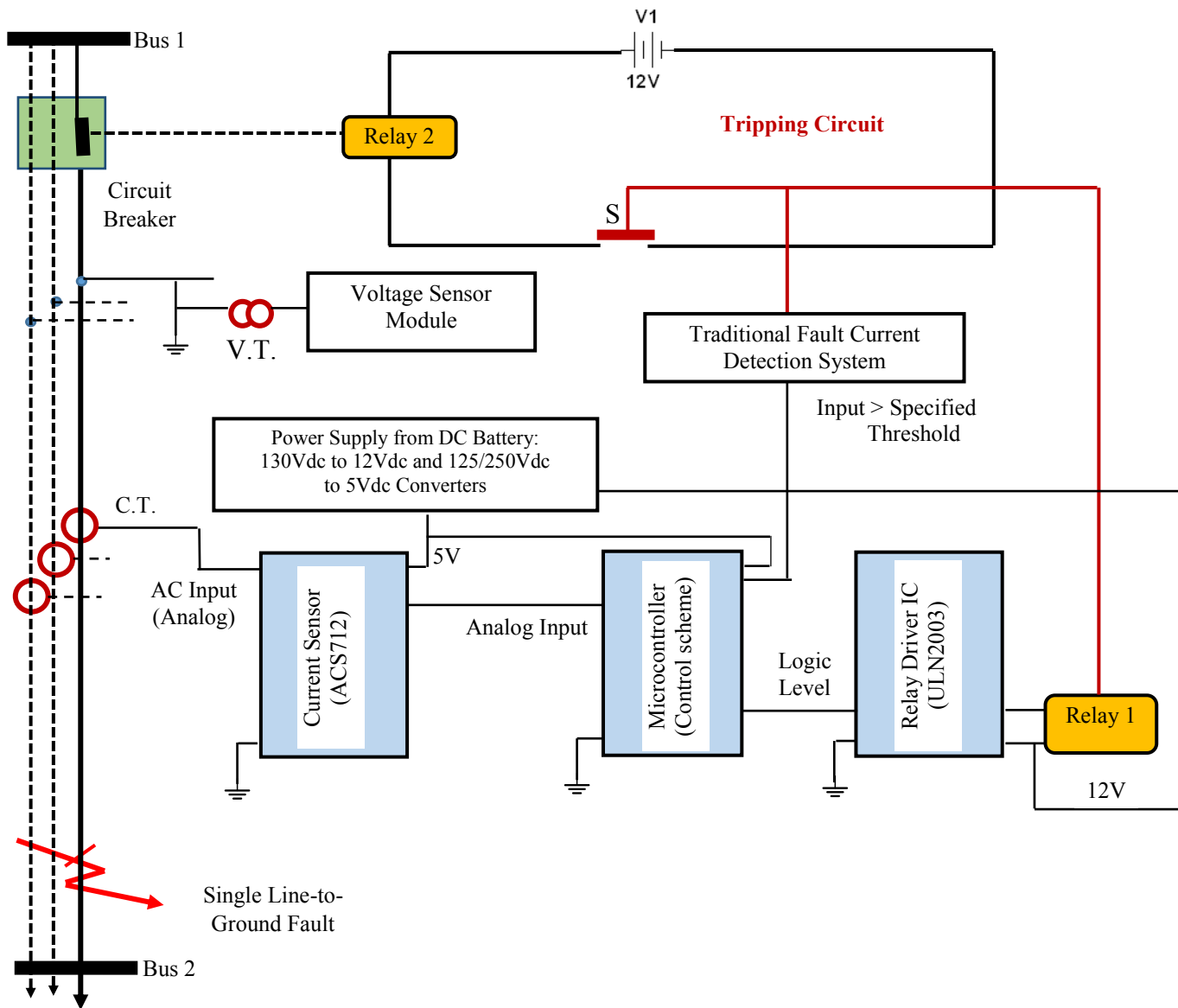


Figure 3. High-Impedance Single Line-to-Ground Fault-Detection System Design

In Figure 3, Relay1 operates Switch_S of the tripping circuit, while Relay2 in the tripping circuit operates (open/close) the applicable circuit breaker. The ULN2003 relay driver chip supports a logic input interface, thus making it compatible to a wide range of microcontrollers and other logic interfaces. When a line-to-ground fault occurs, due to the downing of a live conductor for example, the fault current decreases to a level that cannot operate the overcurrent relay (or a traditional fault-current detection system). The current measured by the current sensor is provided as an analog input to the microcontroller, where the analog-to-

digital converter (ADC) converts the analog input to digital form. The output from the microcontroller is either sent as logic levels to the relay driver chip or as an analog output to the traditional fault-current detection system. A low logic level input to the relay driver chip produces a high logic level output from the relay driver chip to Relay1 and vice versa. A high logic level input to Relay1 energizes this relay and closes Switch_S of the tripping circuit, which subsequently causes Relay2 to open the circuit breaker, thereby isolating the fault segment from the rest of the power distribution system. A non-line-to-ground fault will lead to lower

measured voltage or greater line current compared to a steady-state load condition. Traditional detection systems have the capability to detect and activate relays when the fault current becomes greater than the specified threshold line current. It is important to note that this traditional fault-current detection system will only operate when the impedance of the line (voltage-to-current ratio) becomes less than a predetermined value.

Operational Sequence of the Line-to-Ground Fault-Detection System

The applicable operational sequence of the line-to-ground fault-detection system from Figure 3 is as follows.

1. The current sensor module continuously measures the AC current in the secondary windings of the CT and sends a proportional analog signal representing the measured current value as an input to the microcontroller. If this analog input is greater than the set threshold, it is forwarded to the traditional fault-current detection system; otherwise, the operational sequence goes to Step 2.
2. The microcontroller converts the analog input value to its digital equivalent and executes an embedded fuzzy logic control code.
3. Depending on the logic levels (low or high) from the microcontroller to the relay driver chip, Relay1 is energized or de-energized. For example, if the logic level input to the relay driver chip is low then its corresponding output pin is high and Relay1 is energized. Conversely, if the logic level from the microcontroller to the relay driver is high then the corresponding output from the relay driver is low, and Relay1 is not energized.
4. If Relay1 becomes energized, it causes Switch_S of the tripping circuit to close, thereby energizing Relay2 of the tripping circuit, which subsequently operates the circuit breaker to open its circuit. The opening of the circuit breaker isolates the fault section (or segment) from the rest of the power distribution system.

Modeling Fault Current

An abrupt occurrence of a short-circuit in an AC power distribution system yields a DC component in addition to the AC component. The total fault current is affected by decreases in both AC and DC before reaching a steady-state value. Moreover, addition of DC and AC components yields an asymmetrical current wave about the zero axis. This asymmetrical current is at its maximum during the first cy-

cle after the fault occurs, and gradually becomes symmetrical a few cycles thereafter. It is important to note that the analyses in this study were based on symmetrical currents, where it was assumed that the DC component had decayed to zero. High-impedance fault (HIF) current $i(t)$ is characterized by a decaying sinusoid and described by Equation (1):

$$i(t) = \left(\frac{v_m}{z_0 e^{t/\tau}} \right) \cos(\omega t + \beta - \theta) \quad (1)$$

where, $(v_m/(z_0 e^{t/\tau}))$ is the amplitude of the current signal; θ is the angle by which the steady-state current lags voltage; β provides control for timing of when the fault occurs; v_m represents the magnitude of the line voltage; z_0 represents the line impedance value up to the point of occurrence of a fault; and, τ is a time constant.

Equation (1) is the short-circuit fault-current equation from Makran and Bohmann [27], where the denominator of the amplitude of the current signal has been modified. The modeling of the line impedance in the denominator of Equation (1) shows that the line impedance grows by a factor of $e \cong 2.7183$ every τ , given that z_0 is the line impedance up to the point when the line-to-ground fault occurs. The growth of the line impedance on the occurrence of a line-to-ground fault depends on whether the ground fault was caused by tree branches touching a conductor, a conductor losing its supports and falling on a poorly conductive surface, or others. Variable t denotes time, which is measured in cycles, where one cycle is 1/60 of a second (0.0167 seconds) for a traditional 60 Hz power line. From the point of occurrence of a line-to-ground fault, impedance increases in relation to the time constant. The increasing impedance implies that the current decreases but not to zero. This means that for a high-impedance fault current associated with line-to-ground faults, there cannot be a fault overcurrent on the affected line.

Time-Average Power of a Fault-Current Signal

Time-average power of the fault-current signal ($P_{fcurrent}$) over the time interval $t_1 \leq t \leq t_2$ is given by Equation (2):

$$P_{fcurrent} = \left(\frac{1}{t_2 - t_1} \right) \int_{t_1}^{t_2} \left| \frac{v_m}{z(t)} \cos(\omega t + \beta - \theta) \right|^2 dt \quad (2)$$

where, $z(t) = z_0 e^{t/\tau}$.

By letting $\phi = \beta - \theta$, Equation (2) can be re-written as Equation (3), which, upon using the trigonometric identity $\cos^2 t = 1/2[1 - \cos(2t)]$, yields Equation (4):

$$P_{fcurrent} = \left(\frac{1}{t_2 - t_1} \right) \int_{t_1}^{t_2} \left(\frac{v_m}{z_0 e^{t/\tau}} \right)^2 (\cos(\omega t + \varphi))^2 dt \quad (3)$$

$$P_{fcurrent} = \left(\frac{1}{t_2 - t_1} \right) \int_{t_1}^{t_2} \left(\frac{v_m^2}{z_0^2 e^{2t/\tau}} \right) \frac{1}{2} [1 + \cos(2\omega t + 2\varphi)] dt \quad (4)$$

Using integration by parts twice to solve Equation (4), gives the solution shown in Equation (5):

$$\begin{aligned} P_{fcurrent} = & \left(\frac{1}{t_2 - t_1} \right) \left(\frac{v_m^2}{2z_0^2} \right) \left\{ -\frac{\tau}{2} (e^{2t_2/\tau} - e^{2t_1/\tau}) \right. \\ & + \frac{1}{2} \left(\frac{\omega\tau}{\omega\tau + 1} \right) \left\{ \frac{e^{-2t_2/\tau}}{2\omega} \sin(2\omega t_2 + 2\varphi) \right. \\ & - \left(\frac{e^{-2t_2/\tau}}{2\omega} \right) \cos(2\omega t_2 + 2\varphi) \\ & - \left(\frac{e^{-2t_1/\tau}}{2\omega} \right) \cos(2\omega t_1 + 2\varphi) \\ & \left. \left. + \left(\frac{e^{-2t_1/\tau}}{\omega\tau} \right) \cos(2\omega t_1 + 2\varphi) \right\} \right\} \end{aligned} \quad (5)$$

Time-Average Power of the Current Signal during Normal Power Line Operation

Time-average power of the current signal during normal power line operation ($P_{ncurrent}$) over the time interval $t_1 \leq t \leq t_2$ is given by Equation (6):

$$P_{ncurrent} = \left(\frac{1}{t_2 - t_1} \right) \int_{t_1}^{t_2} \left| \frac{v_m}{z} \cos(\omega t + \beta - \theta) \right|^2 dt \quad (6)$$

where, z is the line impedance.

By letting $\varphi = \beta - \theta$, Equation (6) can be re-written as Equation (7):

$$P_{ncurrent} = \left(\frac{1}{t_2 - t_1} \right) \int_{t_1}^{t_2} \left(\frac{v_m}{z} \right)^2 (\cos(\omega t + \varphi))^2 dt \quad (7)$$

Utilizing the trigonometric identity $\cos^2 t = 1/2[1 - \cos(2t)]$ in Equation (7) and then solving gives the solution shown in Equation (8):

$$\begin{aligned} P_{ncurrent} = & \left(\frac{1}{t_2 - t_1} \right) \left(\frac{v_m^2}{2z^2} \right) \left\{ (t_2 \right. \\ & \left. + \left(\frac{1}{2\omega} \right) \sin(2\omega t_2 + 2\varphi) \right) \\ & \left. - \left(t_1 + \left(\frac{1}{2\omega} \right) \sin(2\omega t_1 + 2\varphi) \right) \right\} \end{aligned} \quad (8)$$

Time-Average Power of the Morlet Wavelet Signal

The ‘‘mother’’ wavelet used for analysis in this study was the Morlet wavelet [1], which is shown in Equation (9):

$$\psi(t) = \left(e^{-t^2/2} \right) (\cos(5t)) \quad (9)$$

Wavelet functions include Daubechies, Morlet, Haar, Symlets, Meyer, Mexcan Hats, and Gaussian wavelets. The Morlet wavelet function was selected because it has no scaling function and is explicit.

It should be noted that the Morlet wavelet is not related to the current signal, but only used to compare oscillations of the current signal at different times. This means that the wavelet was used in this study as a window function for analysis of the current signal.

Time-average power of the wavelet signal $P_{wavelet}$ over the time interval $t_1 \leq t \leq t_2$ is given by Equation (10):

$$\begin{aligned} P_{wavelet} = & \left(\frac{1}{t_2 - t_1} \right) \int_{t_1}^{t_2} \left| \left(e^{-t^2/2} \right) (\cos(5t)) \right|^2 dt \\ = & \left(\frac{1}{t_2 - t_1} \right) \int_{t_1}^{t_2} \left(e^{-t^2/2} \right)^2 (\cos(5t))^2 dt \end{aligned} \quad (10)$$

Recalling the trigonometric identity $\cos^2 t = 1/2[1 - \cos(2t)]$, the $P_{wavelet}$ function can be written as shown in Equations (11)-(13):

$$P_{wavelet} = \left(\frac{1}{t_2 - t_1} \right) \int_{t_1}^{t_2} \left(e^{-2t^2/2} \right) (\cos^2(5t)) dt \quad (11)$$

$$P_{wavelet} = \left(\frac{1}{t_2 - t_1} \right) \int_{t_1}^{t_2} \left(e^{-2t^2/2} \right) (1/2) [1 - \cos(2(5t))] dt \quad (12)$$

$$P_{wavelet} = \left(\frac{1}{t_2 - t_1} \right) \left(\frac{1}{2} \right) \int_{t_1}^{t_2} \left(e^{-t^2} \right) [1 - \cos(10t)] dt \quad (13)$$

By using power series expansion for the exponential term and integration by parts yields Equation (14):

$$\begin{aligned} P_{wavelet} = & \left(\frac{1}{t_2 - t_1} \right) \left\{ \frac{1}{2} (t_2 - t_1) - \frac{1}{2} (t_2^2 - t_1^2) \right. \\ & \left. + \frac{1}{4} (t_2^4 - t_1^4) - \frac{1}{12} (t_2^6 - t_1^6) + \frac{1}{48} (t_2^8 - t_1^8) \right\} \end{aligned} \quad (14)$$

The analysis of the HIF fault-current detection methodology was implemented in MATLAB using the Fuzzy Logic Toolbox. Figure 4 shows a plot of the current and wavelet signals during normal power-line operation in the time interval of 0-1 seconds, while Figures 5-7 show plots of the line-to-ground fault-current signals (for different values of time constant τ) and wavelet signal during the same time interval.

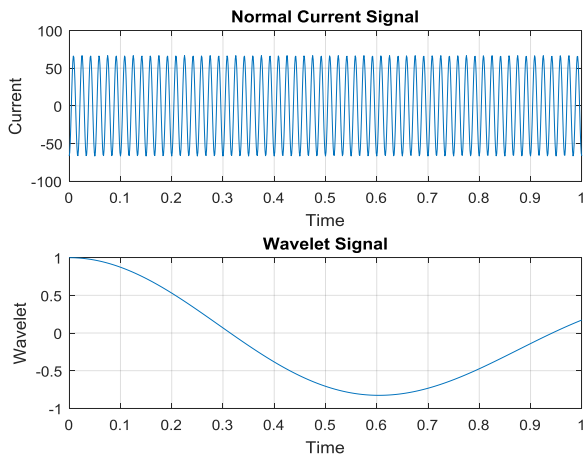


Figure 4. Power-Line Operation (wavelet and normal current signals)

[Case: Equation (8); $f = 60$ Hz, $v_m = 3000$ V, $z = 45\Omega$]

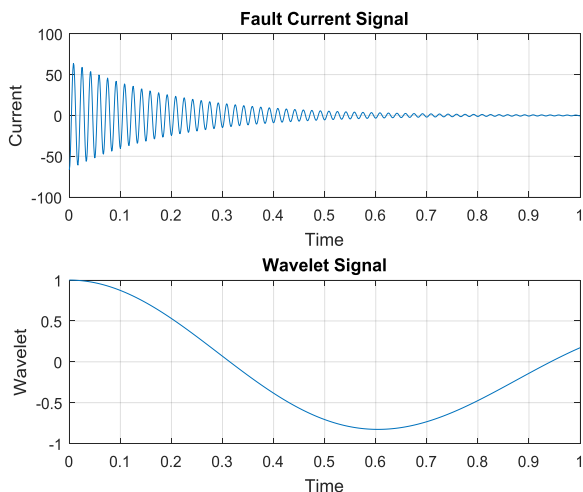


Figure 5. Power-Line Operation (wavelet and line-to-ground fault-current signals)

[Case: Equation (5); $f = 60$ Hz, $v_m = 3000$ V, $z_0 = 45\Omega$, $\tau = 0.2$]

Figures 5-7 show a decaying AC current signal, indicative of high-impedance line-to-ground faults for time constants $\tau = 0.2$, $\tau = 0.3$, and $\tau = 0.4$, respectively. It should be noted that the wavelet plot is identical in all three cases, because

the Morlet wavelet function was used as a window function for analysis of the current signal.

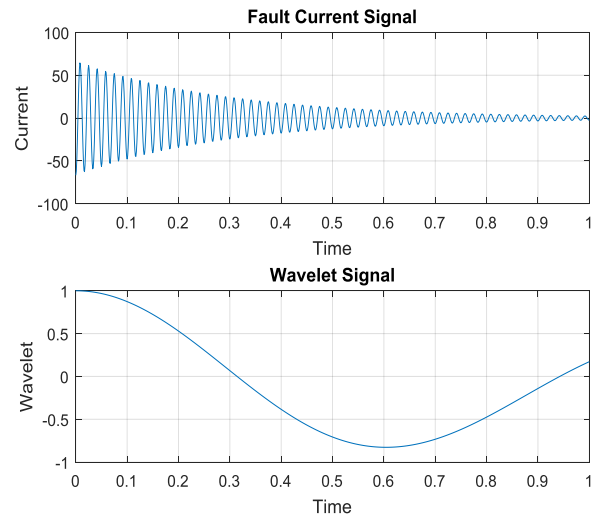


Figure 6. Power-Line Operation (wavelet and line-to-ground fault-current signals)

[Case: Equation (5); $f = 60$ Hz, $v_m = 3000$ V, $z_0 = 45\Omega$, $\tau = 0.3$]

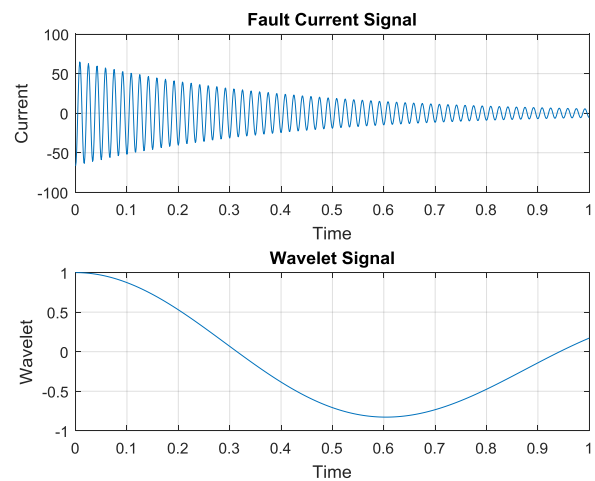


Figure 7. Power-Line Operation (wavelet and line-to-ground fault-current signals)

[Case: Equation (5); $f = 60$ Hz, $v_m = 3000$ V, $z_0 = 45\Omega$, $\tau = 0.4$]

Fuzzy Logic-Based Control Scheme

With respect to Figures 2 and 3, if the computed net time-average power is less than the stored threshold value, then a line-to-ground fault has been detected and the measured current value is forwarded to the fuzzy logic-based module. The fuzzy logic-based control scheme was implemented in MATLAB's Fuzzy Logic Toolbox. The linguistic variable

is the “measured current,” with linguistic values of “low” and “high.” The input variable “measured current” is characterized by a trapezoidal membership function with parameters [0 0 0.84 1.488] for a linguistic low value and parameters [1.24 1.673 5 5] for a linguistic high value. Figure 8 shows the fuzzification of the input variable.



Figure 8. Fuzzification of the Input Variable “Measured Current”

The fuzzy logic system design uses the Mamdani-type inference system, where the output membership functions are fuzzy sets (see Figure 9). Moreover, fuzzy sets representing the output of each fuzzy rule are aggregated into a single fuzzy set. The aggregated output fuzzy set is characterized by trapezoidal membership function with parameters [0 0 0.84 1.488] for a linguistic low value and parameters [1.24 1.673 5 5] for a linguistic high value. The aggregated output fuzzy set is subsequently defuzzified using the centroid method in order to obtain a single output value.



Figure 9. Output Fuzzy Set for “Measured Current”

Fuzzy rules are specified as follows:

Rule 1: IF (Measured-Current is low) then (Aggregated-Output is low)

Rule 2: IF (Measured-Current is high) then (Aggregated-Output is high)

For purposes of illustration, a measured current value less than or equal to 1.5A is considered low and cannot be detected by the traditional fault-current detection system. If the “measured current” input is low [i.e., $i(t) \leq 1.5A$] then the aggregated output is low, and a low logic level is sent from an output pin of the microcontroller to an input pin of the relay driver. Similarly, when “measured current” is high [i.e., $i(t) > 1.5A$] then the aggregated output is high, and a high logic level is sent from an output pin of the microcontroller to an input pin of the relay driver.

Discussion of the Numerical Results

Table 1 shows the numerical parameters and results. Units of the numerical parameters are defined as follows: net power (i.e., $P_{ncurrent}$, $P_{fcurrent}$, and $P_{wavelet}$) is in watts; voltage (v_m) is in volts; time (t_1 or t_2) is in seconds; impedance (z_0) is in Ω ; and, frequency (f) is in Hz. For purposes of illustration, the unit of power for the wavelet signal is assumed to be watts. With a distribution line voltage of 3000 volts, a line supply frequency of 60 Hz, and an assumed line impedance of 45Ω during normal line operation and varying values of the time constant, Table 1 shows the computed values of time-average power (normal current), time-average power (fault current), time-average power (wavelet) and net time-average power (i.e., time-average power of current signal – time average power of wavelet signal). The values used for the numerical analysis, shown in Table 1, are only for purposes of illustration. Figure 10 shows a graph of net power for normal and fault currents sampled over the time interval of 0-1 second. For this time interval, the time-average power of the current signal during normal operation and time-average power of the wavelet signal are computed separately; the net time-average power is determined and stored as a baseline value.

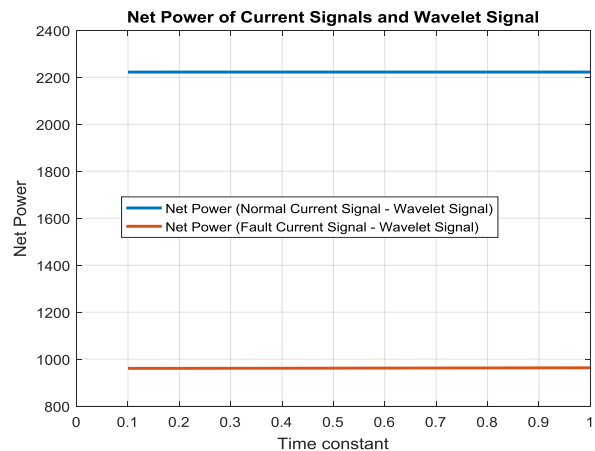


Figure 10. Net Power of Normal and Fault-Current Signals during the Same Time Interval

Table 1. Numerical Parameters and Results for Wavelet, Normal-Current and Fault-Current Analyses

t_1	t_2	β	θ	τ	v_m	f	$z_0; z$	$P_{ncurrent}$	$P_{fcurrent}$	$P_{wavelet}$	$P_{fcurrent}-P_{wavelet}$
0	1	$\pi/4$	$\pi/2$		3,000	60	45	2,222.5		0.1875	2,222.31
0	1	$\pi/4$	$\pi/2$	0.1	3,000	60	45		960.91	0.1875	960.72
0	1	$\pi/4$	$\pi/2$	0.2	3,000	60	45		961.03	0.1875	960.84
0	1	$\pi/4$	$\pi/2$	0.3	3,000	60	45		961.22	0.1875	961.03
0	1	$\pi/4$	$\pi/2$	0.4	3,000	60	45		961.46	0.1875	961.27
0	1	$\pi/4$	$\pi/2$	0.5	3,000	60	45		961.72	0.1875	961.53
0	1	$\pi/4$	$\pi/2$	0.6	3,000	60	45		962.02	0.1875	961.83
0	1	$\pi/4$	$\pi/2$	0.7	3,000	60	45		962.33	0.1875	962.14
0	1	$\pi/4$	$\pi/2$	0.8	3,000	60	45		962.65	0.1875	962.46
0	1	$\pi/4$	$\pi/2$	0.9	3,000	60	45		962.97	0.1875	962.78
0	1	$\pi/4$	$\pi/2$	1.0	3,000	60	45		963.30	0.1875	963.11

With respect to Table 1, whereas the net power of the current signal during normal line operation is 2,222.31W, the net power of the current signal during a line-to-ground fault ranges from 960.91W to 963.30W for a time constant varying from 0.1 to 1.0. The robustness of the high-impedance line-to-ground fault (HIF) detection system design is further demonstrated by capabilities of the integrated fuzzy logic control scheme. The fuzzy logic-based HIF detection system design (see again Figure 3), the universe of discourse is 0-5A, since the current transformer (CT) is capable of handling AC currents up to 5A. Figures 11-14 show the results of the activation of the fuzzy rules. In Figures 11-13, the graphs in the left column represent input fuzzy sets with linguistic values of low (top) and high (bottom), while the graphs in the right column represent aggregated output fuzzy sets with linguistic values of low (top) and high (next graph). The red vertical line in each graph indicates applicable values of measured current shown at the top of each graph.

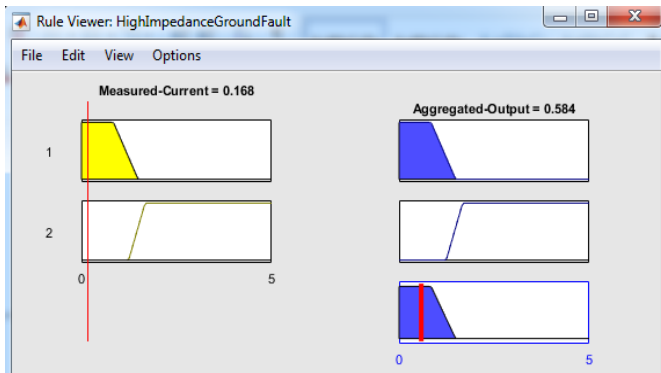


Figure 11. Activation of Fuzzy Rules (Rule Viewer 1)

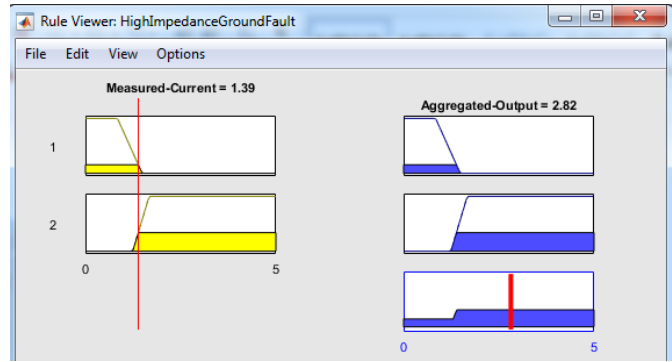


Figure 12. Activation of Fuzzy Rules (Rule Viewer 2)

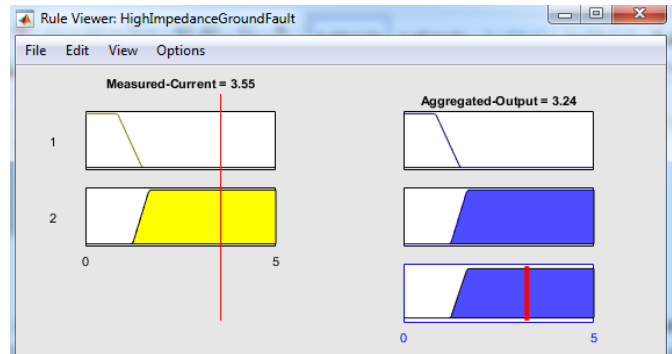


Figure 13. Activation of Fuzzy Rules (Rule Viewer 3)

In Figure 11, for example, at a measured fault current of 0.168A (low), the aggregated output from the microcontroller is 0.584 (low). This means that a low output signal from the microcontroller to the relay driver chip causes a corresponding output pin of the relay driver chip to have a high signal. A high signal on an output pin of the relay driver

chip causes Relay1 to become energized and subsequently closes Switch_S of the tripping circuit. Similarly, a measured current of 1.39A (low) in Figure 12, yields an aggregated output of 2.82 (low). This means that a low output signal from the microcontroller to the relay driver chip causes a corresponding output pin of the relay driver chip to have a high signal. A high signal on the output pin of the relay driver chip causes Relay1 to become energized, which closes Switch_S of the tripping circuit (refer again to Figure 3).

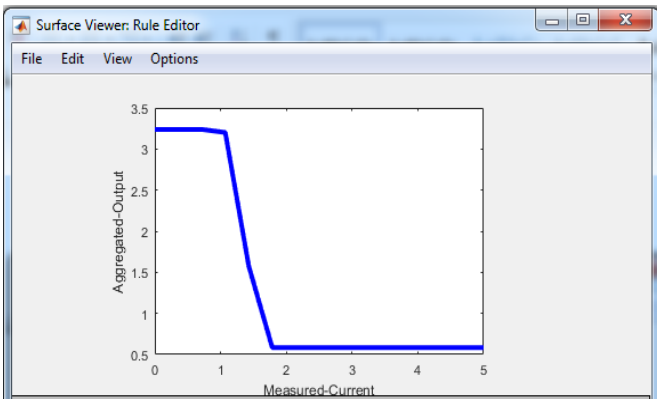


Figure 14. Activation of Fuzzy Rules (Surface Viewer)

However, at a measured fault current of 3.55A (high) in Figure 13, the aggregated output from the microcontroller is 3.24 (high). This means that a high output signal from the microcontroller to the relay driver chip causes a corresponding output pin of the relay driver chip to have a low signal. A low signal on the output pin of the relay driver chip cannot energize or activate Relay1. It is important to note that a high output signal from the microcontroller indicates that a measured current is greater than the set threshold of 1.5A. In this case, the traditional fault-current detection system handles the measured current. Figure 14 shows the surface viewer of the activation of the fuzzy rules. This plot demonstrates the responsiveness of the defuzzified aggregated output to changes in input (“measured current”). For example, for a measured current greater than the specified threshold of 1.5A, the defuzzified aggregated output value is 3.24 (high). However, for a measured current of 1.23A, which is lower than the specified threshold of 1.5A, the defuzzified aggregated output value is 0.67 (low).

Contributions of This Study

Commercial and industrial facilities as well as households may have balanced incoming supply voltages, but imbalances can develop within buildings due to single-phase overloading. Unbalanced loads are the main cause of unbalanced voltages and distribution currents. This paper addresses de-

tection of high-impedance line-to-ground faults in both balanced and unbalanced 3-phase electrical power distribution systems. The work of Jamil et al. [19] for example, focused on identifying various faults in electrical distribution systems for an unbalanced distribution electrical power system, using discrete wavelet transform (DWT) to calculate the change in energy of a particular energy level for a measured current signal. Wavelet transform was used to compute wavelet coefficients, and the calculated energy of the wavelet coefficients was then used as an input into the fuzzy logic system. Energy content was computed as the sum of the squared magnitude of the wavelet coefficients.

Application of DWT to current signal breaks down this function (signal) into both an approximation signal at a certain decomposition level n (i.e., a_n) and n detail signals (i.e., d_k , with k varying from 1 to n). DWT will normally filter a measured signal into different details and approximations, using specified frequency sub-bands (or ranges). For a stable utility power system interconnected by the power grid, frequency variations are extremely uncommon. Frequency variation is more common at sites with standby generators or poor power infrastructure. For a single-frequency signal (for example, 60 Hz in USA or 50 Hz in Europe and other regions), DWT decomposition does have a fundamental weakness, as only a wavelet coefficient will reflect the evolution of the entire component of the original current signal. The rest of the wavelet coefficients will be approximately zero, since no other frequency components exist in the original current signal. Consequently, application of DWT to single-frequency signals (current or voltage) leads to computational redundancy and inefficiency. In this paper, the author addresses this weakness along with other contributions to the greater body of knowledge.

The high-impedance line-to-ground fault-detection system is designed for implementation on all three phases of the power distribution system in order to monitor abnormalities in line currents. Since power system imbalances affect the magnitude and phase angle of the current waveform, it follows that the detection scheme works for both balanced and unbalanced systems, as it detects changes in magnitude of line current on each phase. When implemented on all three phases of a power distribution system, it means the scheme can detect single line-to-ground, double line-to-ground, and three line-to-ground faults. For both balanced and unbalanced electrical power distribution systems, this method can compute time-average power of current signals and Morlet wavelet signals separately over a time interval of one second. Depending on the result of the comparison between the stored baseline net power and subsequently calculated net power, a decision can be made whether or not to use the measured current value as input to the fuzzy logic system.

The main contributions of this study can be summarized as follows:

1. The method provides a new approach for the application of wavelets in detection of high-impedance line-to-ground fault current and protection of both balanced and unbalanced distribution power systems. Indeed, frequency variation does not affect the applicability of the technique, as the current signal is sampled for a period of 0-1 second. In addition, frequency is captured as a parameter in the computations of power of the measured current signal both pre-fault and during fault; that is, $\cos(\omega t + \varphi) = \cos(2\pi ft + \varphi)$.
2. The method provides an effective means for detecting high-impedance line-to-ground faults at all levels of fault current (i.e., $0 < i(t) \leq 5A$), and open a circuit breaker to isolate the fault section from the rest of the power distribution system.
3. The integrated fuzzy control scheme allows smooth transition between different classifications of fault current, thereby providing effective isolation of the fault section from the rest of the power distribution system. For example, within the overlap region of the fuzzy sets (i.e., linguistic terms low and high), the fuzzy logic module invokes the fuzzy min- and max-operators for fuzzy interpolative inferencing [14].
4. When the technique is implemented on all three phases of a 3-phase power distribution system, the approach can detect high-impedance line-to-ground faults in any of the three phases and operate applicable circuit breakers to isolate the fault section (or segment) from the rest of the power distribution system. Thus, the occurrence of a high-impedance fault current in any one of the three phases is a necessary and sufficient condition for the operation of the applicable circuit breaker to effectively protect the power distribution system.

In addition to the above contributions, the author also presents a detection system design and implementation framework for fuzzy logic-based line-to-ground fault detection and protection of power distribution systems.

Conclusions

In this paper, the author presents a new approach for detection of high-impedance line-to-ground faults and protection of electrical power distribution systems as well as an implementation framework. The fault-detection system design utilizes instrument transformers, a microcontroller, relay driver IC, current sensor, relays, fuzzy logic system, and circuit breaker. The detection system continuously

monitors deviations caused to detection metrics that are associated with the line impedance when a line-to-ground fault occurs, as compared to normal operating conditions. Moreover, the detection system was tested via numerical analysis using MATLAB and the Fuzzy Logic Toolbox. The results obtained show that this study contributes in the following ways: (i) the research provides a new approach for the application of wavelets in detection of line-to-ground faults and protection of power distribution systems; (ii) the research provides an effective methodology for detecting high-impedance line-to-ground faults at all levels of fault current, and opens applicable circuit breakers to isolate fault section from the rest of the power distribution system; (iii) the integrated fuzzy control scheme allows for a smooth transition between different classifications of fault current, thereby providing effective isolation of the fault section from the rest of the power distribution system; and, (iv) when the technique is implemented on all three phases of a 3-phase power distribution system, the approach can detect HIF in any of the three phases and operate circuit breakers to isolate the affected section or segment.

Future research will investigate high-impedance line-to-ground faults in power distribution systems, based on asymmetrical fault currents.

References

- [1] Misiti, M., Misiti, Y., Oppenheim, G., & Poggi, J-M. (1996-1997). Wavelet Toolbox for use with MATLAB, *The Mathworks Inc.*, www.mathworks.com, 1, 7-15.
- [2] Prasada, C. D., & Srinivasua, N. (2015). Fault Detection in Transmission Lines using Instantaneous Power with ED based Fault Index. *Procedia Technology, Elsevier*, 21, 132-138.
- [3] Ma, J., Ma, W., Qiu, Y., & Thorp, J. S. (August, 2015). An Adaptive Distance Protection Scheme Based on the Voltage Drop Equation. *IEEE Transactions on Power Delivery*, 30(4), 1931-1940.
- [4] Majidi, M., Arabali, A., & Etezadi-Amoli, M. (August, 2015). Fault Location in Distribution Networks by Compressive Sensing. *IEEE Transactions on Power Delivery*, 30(4), 1761-1769.
- [5] Bains, T. P. S., & DadashZadeh, M. R. (August, 2015). Enhanced Phasor Estimation Technique for Fault Location in Series-Compensated Lines. *IEEE Transactions on Power Delivery*, 30(4), 2058-2060.
- [6] Alyami, H. H. (2015). Protective Relay Models for Electromagnetic Transient Simulation. *International Journal of Innovative Research in Advanced Engineering*, 2(1), 43-51.

- [7] Kumar, R., Saini, N., & Saini, A. (October, 2014). An Artificial intelligence Approach to Detection of High Impedance Fault. *International Journal of Advanced Research in Computer and Communication Engineering*, 3(10), 8092-8094.
- [8] Khandare, N., & Khatri, P. (March, 2015). Analysis and Modeling of High Impedance Fault. *SSRG International Journal of Electrical and Electronics Engineering*, 2(3), 1-5.
- [9] Milioudis, A. N., Andreou, G. T., & Labridis, D. P. (March, 2015). Detection and Location of High Impedance Faults in Multi-conductor Overhead Distribution Lines Using Power Line Communication Devices. *IEEE Transactions on Smart Grid*, 6(2), 894-902.
- [10] Sarvi, M., & Torabi, S. M. (August, 2012). Determination of Fault Location and Type in Distribution Systems using Clark Transformation and Neural Network. *International Journal of Applied Power Engineering*, 1(2), 75-86.
- [11] Nowicki, T., Swirszcz, G., & Yao, M. (May 22-27, 2011). Developing Methods for the Detection of High Impedance Faults in Distribution Power Grids. Paper presented at *ENERGY 2011: The First International Conference on Smart Grids. Green Communications and IT Energy-aware Technologies*, Venice/Mestre, Italy, 114-119.
- [12] Milioudis, A., Andreou, G., & Labridis, D. (2012). Enhanced Protection Scheme for Smart Grids using Power Line Communications Techniques—Part I: Detection of High Impedance Fault Occurrence. *IEEE Transaction on Smart Grid*, 3(4), 1621-1630.
- [13] Milioudis, A., Andreou, G., & Labridis, D. (2012). Enhanced Protection Scheme for Smart Grids using Power Line Communications Techniques—Part II: Location of High Impedance Fault Position. *IEEE Transaction on Smart Grid*, 3(4), 1631-1640.
- [14] Zadeh, L. A. (1965). Fuzzy Sets. *Information and Control*, 8, 338-353.
- [15] Olunloyo, V. O. S., Ajofoyinbo, A. M., & Ibidapo-Obe, O. (2011). On Development of Fuzzy Controller: The Case of Gaussian and Triangular Membership Functions. *Journal of Signal and Information Processing*, 2, 257-265.
- [16] Ajofoyinbo, A. M., & Olowokere, D. O. (2015). Fuzzy Control Model for Structural Health Monitoring of Civil Infrastructure Systems. *Journal of Control Science and Engineering*, 1, 9-20.
- [17] Kamel, J. (2014). New Approach for Modeling Random Disturbances. *Journal of Control Science and Engineering*, 2, 16-27.
- [18] Jain, A., Thoke, A. S., & Patel, R. N. (2009). Classification of Single Line-to-Ground Faults on Double-Circuit Transmission Line using Artificial Neural Networks (ANN). *International Journal of Computers and Electrical Engineering*, 1(2), 196-202.
- [19] Jamil, M., Singh, R., & Sharma, S. K. (2015). Fault Identification in Electrical Power Distribution System using Combined Discrete Wavelet Transform and Fuzzy Logic. *Journal of Electrical and Information Technology*, 2, 257-267.
- [20] Badran, E. A., Abdallah, E., & Shebl, K. M. (2011). A complete General Logic-based Intelligent Approach for High Impedance (HIF) Detection and Classification in Distribution Systems. *Journal of American Science*, 7(9), 951-959.
- [21] Mahajan, H., & Sharma, A. (April, 2014). Various Techniques used for protection of transmission line – A review. *International Journal of Innovations in Engineering and Technology*, 3(4), 32-39.
- [22] ACS712 Current Sensor Datasheet. Retrieved from <http://www.allegromicro.com>
- [23] ULN2003 Relay Driver Chip Datasheet. Retrieved from *STMicroelectronics*, <http://www.st.com>
- [24] IEEE C57.13. *IEEE Standard Requirements for Instrument Transformers*. Retrieved from <https://standards.ieee.org>
- [25] Schweitzer Engineering Laboratories, Inc. PF00082 - 20150529. *SEL-932I Low-Voltage DC Power Supply*. Retrieved from <https://www.selinc.com>
- [26] Wilmore Electronics. DC-DC Converter Series 1720. Retrieved from <https://www.wilmoreelectronics.com>
- [27] Makran, E. B., & Bohmann, L. (September 7-12, 2003). Short Circuit Calculations, Unsymmetrical Faults. Paper presented at the *2003 IEEE Transmission and Distribution Conference, Education Tract*, Dallas, Texas, USA.

Biography

ABAYOMI AJOFOYINBO received his PhD in systems engineering (Electrical and Electronics System) from the University of Lagos, Nigeria, in 2008. Dr. Ajofoyinbo is a faculty member in the Department of Engineering (Electrical & Computer) at Texas Southern University. He teaches courses and conducts research in electrical/electronic and computer engineering. Dr. Ajofoyinbo worked for TSU as a postdoctoral fellow at the NSF CREST Centre for Research on Complex Networks. His research interests include electrical power transmission and distribution systems, intelligent control, embedded systems, and wireless communications. He has published peer-reviewed papers in referred journals and has made presentations in numerous conferences worldwide. Dr. Ajofoyinbo may be reached at ajofoyinboa@tsu.edu

A MODEL FOR STATIONARY PLATFORM PLACEMENT PROBLEMS IN MILITARY SURVEILLANCE

Nebil Buyurgan, Missouri State University; Nabil Lehlou, Womply/Oto Analytics; Kevin M. Hubbard, Missouri State University

Abstract

In this paper, the authors present an analytical and flexible stationary system placement method for military surveillance outposts to improve the effectiveness of their use. Based on the geo-location of a military outpost and its associated surveillance parameters, this method employs a heuristic model to provide optimum and cost-effective surveillance coverage. Coverage ranges for stationary systems are calculated using their field-of-view projections on the ground. Starting from a designed surveillance area as a form of surveillance, a tape that surrounds the perimeter of an outpost, the coverage contributions of the system are maximized, while minimizing inefficient overlaps to provide a base structure for the needed surveillance coverage. Stationary systems are then placed within the surveillance tape with a specified lack of coverage allowance to avoid generating overkill (expensive) solutions. The proposed method was applied in the area of Combat Outpost Kahler in Afghanistan, an outpost that was the target of a heavy insurgent attack in 2008. The results indicated that image resolution level, surveillance tape thickness, and coverage allowance had impacts to a certain degree on the number of required stationary systems, which can be optimized under certain conditions to maximize the coverage.

Introduction

When U.S. armed forces deploy troops in a new area, they use installations called Forwarding Operating Bases to support tactical operations [1, 2]. In addition to these well-protected bases, temporary bases, called Outposts, are used to attain wider area protection. As military operations become more distributed, outposts are commonly used as permanent deployment locations. In some cases, they are located in disadvantageous regions, where terrain is rough, villagers sympathize with insurgents, and a transportation network is distant. Therefore, the use of camera- and sensor-based surveillance systems that can operate continuously to detect and identify insurgent activities becomes an important part of military operations. Surveillance system platforms can be categorized as: 1) stationary platforms, such as towers and aerostats; 2) mobile platforms, such as fixed-wing and rotary-wing vehicles; and, 3) both, such as tethered or free-flying lighter-than-air (LTA) platforms. Towers and aerostats, which were the focus of this study,

are commonly used as platforms for stare (or persistent surveillance) systems, as they offer full-motion video, long-distance monitoring, and wide-area coverage.

Stationary platforms offer a convenient technological means to monitor the surrounding terrain; however, because of their immobility, these platforms have to be somehow protected. From a cost perspective, stationary platforms offer affordable solutions. Towers (also referred to as rapidly erected towers) are considered inexpensive and easily deployable surveillance platforms. They present an important alternative to free-flying aerial platforms, since data and power can be supplied via cables from the ground. The most significant disadvantage of towers, however, is the time required to erect them. Moreover, they can hold only small cameras and sensors with small coverage ranges. Aerostats, which are aerodynamically shaped tethered balloons, are considered more capable platforms for large-area military surveillance. They are capable of transmitting and receiving power and data through the tether and can go significantly higher than towers [3]. However, they need periodic servicing, a reason for which they cannot remain airborne for longer periods of time. They also lack an effective means of steering. Most aerostats have several maintenance and manpower requirements, which may result in costs over \$2.5 million per year [4].

In this paper, the authors present a method for stationary platform placement to provide optimum and cost-effective surveillance range and coverage for irregularly shaped outposts by locating and positioning them. The method systematically uses a heuristic model with a set of algorithms to assess and evaluate the surveillance area accurately, and determine the position of platforms efficiently. Starting from a designed surveillance area, the coverage of each platform is maximized, while minimizing coverage overlap between platforms for optimum platform placement.

Background

Camera and sensor systems are typically employed for large-area surveillance to collect and disseminate real-time information or to monitor resources for better situational awareness. They also provide perimeter security in hostile environments, where aerial technology is not available [5-7]. Platform and mission package selection is typically performed based on mission requirements, cost limitations,

and required surveillance levels. A cost-benefit analysis for a number of platforms was presented by Everly and Limmer [8] for different military operations, including humanitarian aid/disaster relief, long-range information exchange, and tactical communication. Automated surveillance systems are used to detect suspicious ship behavior by monitoring their movements continuously in military harbors [9]. They are also used in mobile surveillance systems to enhance the sight of pursuers and reveal evaders by informing them about the relative positions and movements of evaders [10]. Similarly, 2D sensor surveillance systems are designed with inexpensive sensors to detect and identify intruders [11].

Each camera or sensor in a surveillance system has both field-of-view (FoV) and depth-of-view (DoV) attributes. These are the major attributes of a system that are used to optimize camera locations. Using these attributes, many military surveillance studies focus on developing optimized placement strategies by minimizing FoV overlap in 2D applications, while maximizing DoV coverage in 3D applications [12, 13]. In addition to FoV and DoV, object and motion observability (detection), effective system communication and control, and sensor coverage density are also used as performance indicators for optimal sensor placement. The method used in this current study was designed to address the stationary platform placement problem for sensor-based military surveillance systems. A heuristic model was developed to optimize the coverage in a surveillance area, given as a thick tape (also referred to as a virtual wall) around an outpost that acts as an alarm zone. The surveillance coverage for each platform was then formulated based on sensor FoV and DoV and a required surveillance level (e.g., image resolution). The coverage of sensors was evaluated based on their contribution to overall surveillance and FoV overlap. This information was used to determine platform locations by filling the surveillance tape with sensor ranges to maximize the overall coverage.

Platform Placement Problem Method

The first step of the method is to design a virtual wall that surrounds the perimeter of an outpost. The virtual wall structure provides a defensible surveillance area for irregularly shaped outposts. The information required to achieve a virtual wall structure includes the height and width of the inner rectangle, as demonstrated in Figure 1(a), the thickness of the wall (i.e., the range), an allowance for lack of coverage, as shown in Figure 1(b), and the (x, y) coordinates of the center of the inner rectangle. Once a virtual wall is designed, sensor ranges are positioned to maximize coverage. This task is referred to as the Platform Placement Problem (P^3); an optimization problem in that it targets covering a certain percentage of the area with the least number

of sensors. A surveillance plan that is based strictly on tower-mounted cameras can be constructed by placing sensor ranges all over the virtual wall. However, including an aerostat in this plan may significantly change the placement of sensors based on added coverage. Figure 2 depicts three different aerostat coverage scenarios.

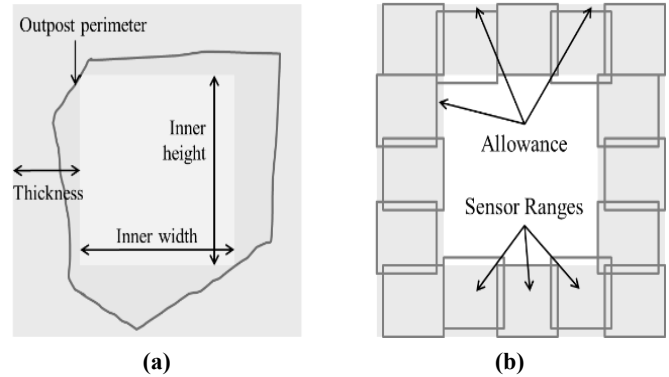


Figure 1. Method for Enveloping the Irregular Perimeter of the Outpost with a Virtual Wall

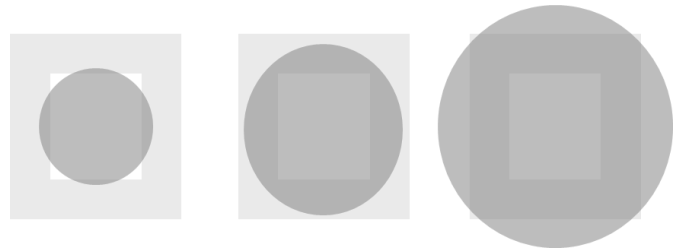


Figure 2. Aerostat Coverage Scenarios

The first plan requires significant use of tower-mounted cameras; the second plan needs the help of tower-mounted cameras to cover the entire surface; the third plan does not require any additional coverage.

Platform Coverage

In this study, the coverage of a stationary platform means the projection sensor's FoV on the ground. As a result, platform coverage is a function of a sensor's DoV, slant range, and angle-of-view (AoV), as shown in Figures 3 and 4. An increase in DoV leads to a larger coverage but reduces image resolution. In addition, a change in AoV results in inconsistencies in resolution. To handle this tradeoff, AoV is set fixed to a specific value, and DoV is evaluated at three different resolution levels: vehicle detection level (DV), dismount detection level (DD), and dismount identification level (ID). An aerostat typically carries its sensors with an AoV of 90° and FoV of 120° . This fact allows the FoV of the dominant sensor to have a circular projection. The radi-

us of the circle can be set to r_{ID} in order to identify dismounts; to r_{DD} in order to detect dismounts; or, to r_{DV} in order to detect vehicles by increasing or reducing DoV accordingly. Note that $r_{ID} = 250\text{m}$, $r_{DD} = 1000\text{m}$, and $r_{DV} = 4000\text{m}$ are the values used by the military. The FoV concept is applied differently for tower-mounted cameras, since the slant of the dominant sensor is set almost horizontally. Cameras are assumed to have a panning capability of 360° and r_{ID} , r_{DD} , and r_{DV} are estimated using the capabilities of comparable mobile surveillance platforms. A comparable mobile platform, the Raven-IR, typically has the following values: $r_{ID} = 40\text{m}$, $r_{DD} = 160\text{m}$, and $r_{DV} = 640\text{m}$.

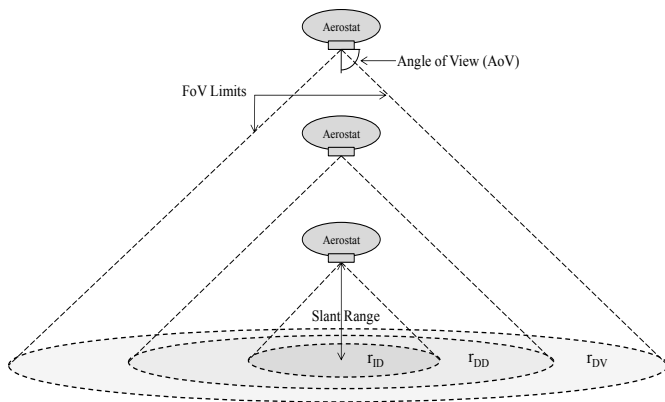


Figure 3. FoV Representation for an Aerostat Sensor at Three Different Levels of Surveillance

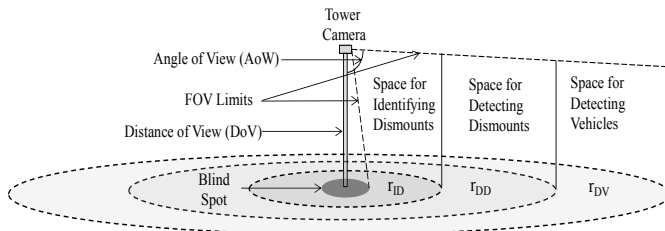


Figure 4. FoV Representation of a Tower Camera at Three Different Levels of Surveillance

FoV projection for tower-mounted cameras is modeled as a filled square rather than a circle. Figure 5 shows how these squares are acquired by maximizing their dimensions, while still staying inside the circular shape. This is a conservative approach for developing a surveillance plan so that it is not prone to vulnerabilities [see Figure 1(b)]. Moreover, after camera placement, the original shape of the coverage area is restored for more accurate reports.

Coverage Overlap

Two types of overlaps were considered in this study. Type 1 overlap, which is referred to as the coverage contri-

bution, is the intersection between the sensors' FoV projections and segments of the virtual wall. It determines the portion of a sensor's range that is actually meeting the demand for coverage. This type of overlap is desired and, therefore, should be maximized. Type 2 overlap refers to an intersection between any two or more sensor coverage contributions. Depending on the case, this type of overlap may or may not be desired. If more overlap means increased coverage redundancy without increasing cost, then that is ideal. However, if Type 2 overlap is a result of positioning cameras inefficiently close to each other, requiring more platforms to cover the target area, then that is not a desirable condition. The formulation of Type 2 overlap depends heavily on the formula associated with Type 1 overlap. The overlap of two sensor ranges is strictly the portion of their intersection area that is situated inside the virtual wall. As a result, the coverage contributions of two sensors must be obtained by acquiring their Type 1 overlap, and then the two coverage contributions can be used to determine Type 2 overlap through their intersection.

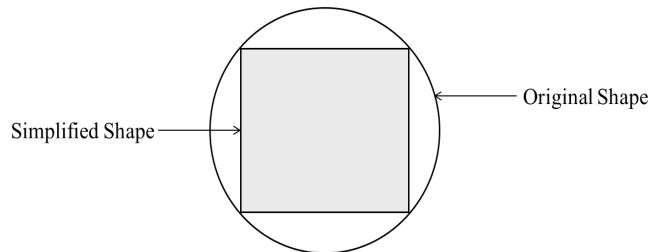


Figure 5. Trimming the Circular Shape of the Camera's Coverage to Obtain a Square

Since virtual wall segments and sensor ranges are assumed to have a rectangular shape, both kinds of overlaps yield simple area computations, as the intersection of two rectangles is a rectangle. Nevertheless, there is some complexity in formulating this intersection, since the dimensions of the virtual wall segments and the FoV projections can, in theory, hold any value. Figure 6 depicts how the overlap formulation is constructed in a generic fashion and specifically for the following scenarios: a) two rectangles, i and j , are far away from each other; b) rectangle j is completely inside rectangle i ; c) rectangle j is partially inside rectangle i ; and, d) rectangles i and j cross each other with maximum overlap without one fitting inside the other.

To formulate a two-shape overlap, regardless of its type, let (x_{ij}, y_{ij}) be the center coordinates of the rectangular intersection of rectangles i and j , where w_{ij} is its width and h_{ij} is its height. In the first scenario, x_{ij} does not exist, whereas $x_{ij} = x_j$ in the second scenario. In the third scenario, $x_{ij} = x_i + (w_i/2 - w_{ij}/2)$, if $x_i < x_j$ and $x_{ij} = x_i - (w_i/2 - w_{ij}/2)$, if $x_i > x_j$. In the fourth scenario, $x_{ij} = x_i$, if $w_{ij} = w_i$ and $x_{ij} = x_j$, if $w_{ij} = w_j$. To render the formulation process, each of the

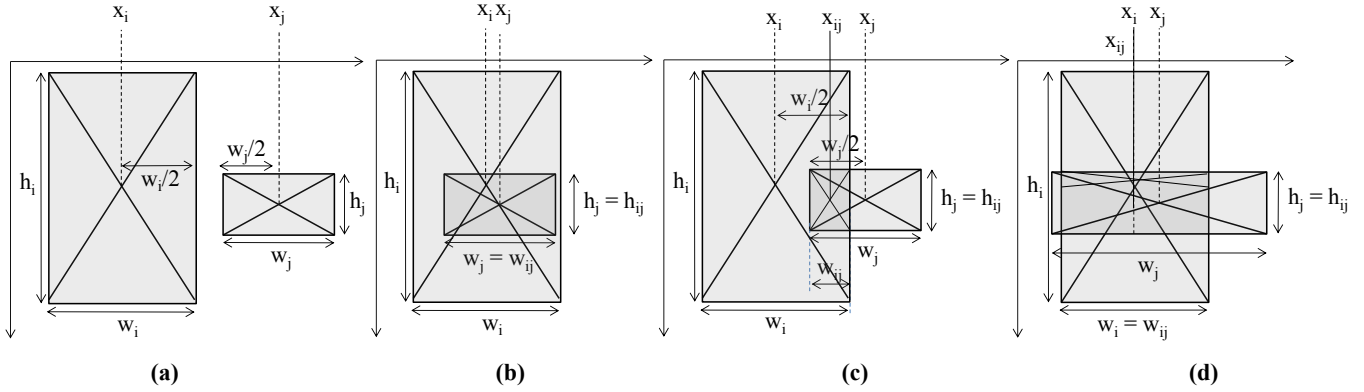


Figure 6. The Four Scenarios of Overlap with Regards to the Width, w_{ij} , and x-Coordinate, x_{ij}

aforementioned cases is applied on w_{ij} , as h_{ij} can be attained with the same steps as w_{ij} . To proceed with a complete formulation, let i and j have widths w_i and w_j , heights h_i and h_j , an x-coordinate x_i and x_j , and a y-coordinate y_i and y_j , respectively. Both w_{ij} , and h_{ij} can be formulated as Equations (1) and (2):

$$w_{ij} = F_w(i,j) = \min\{w_i, w_j, \max(0, w_i/2 + w_j/2 - |x_i - x_j|)\} \quad (1)$$

$$h_{ij} = F_h(i,j) = \min\{h_i, h_j, \max(0, h_i/2 + h_j/2 - |y_i - y_j|)\} \quad (2)$$

Assuming that an overlap between rectangles i and j is verified, the x-coordinate and the y-coordinate of the overlap, x_{ij} and y_{ij} , can be computed using Equations (3) and (4):

$$F_x(i,j) = \begin{cases} x_i & \text{if } w_{ij} = w_i \\ x_j & \text{if } w_{ij} = w_j \\ x_i + (w_i/2 - w_{ij}/2) & \text{if } x_i < x_j, w_{ij} \neq w_i, w_{ij} \neq w_j \\ x_i - (w_i/2 - w_{ij}/2) & \text{if } x_i > x_j, w_{ij} \neq w_i, w_{ij} \neq w_j \end{cases} \quad (3)$$

$$F_y(i,j) = \begin{cases} y_i & \text{if } h_{ij} = h_i \\ y_j & \text{if } h_{ij} = h_j \\ y_i + (h_i/2 - h_{ij}/2) & \text{if } y_i < y_j, h_{ij} \neq h_i, h_{ij} \neq h_j \\ y_i - (h_i/2 - h_{ij}/2) & \text{if } y_i > y_j, h_{ij} \neq h_i, h_{ij} \neq h_j \end{cases} \quad (4)$$

Coverage Contribution

In order to construct a solution for P^3 , a well-established coverage measure is necessary. In this context, Equations (3) and (4) were employed as a foundation to compute a certain layout coverage of sensor range yields. First, assume

that a 2D space is to be covered, A , and has a rectangular shape where the top left corner is the origin of the frame $(0, 0)$, as depicted in Figure 7. Let W be the width of this rectangle and H its height.

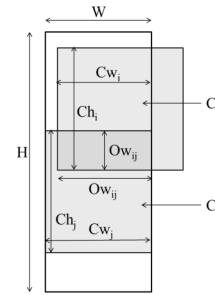


Figure 7. Two Overlapping Sensor Ranges Positioned over a Segment of the Virtual Wall

Also, for any sensor i , let $s_i = s$ be its coverage side's length, x_i its x-coordinate, and y_i its y-coordinate. Furthermore, let C_i be the sensor's coverage contribution (i.e., the FoV's intersection with space A), and $Cw_i, Ch_i, (Cx_i, Cy_i)$ be its width, height, and coordinates, respectively. Finally, let O_{ij} be the overlap between sensors i and j (i.e., the intersection of their coverage contributions) with Ow_{ij} and Oh_{ij} as its width and height, respectively. Next, use Equations (5)-(9) to calculate the coverage contribution parameters.

$$Cx_i = F_x(i,A) \quad (5)$$

$$Cy_i = F_y(i,A) \quad (6)$$

$$Cw_i = F_w(i,A) = \min\{W, s, \max(0, W/2 + s/2 - |W/2 - x_i|)\} \quad (7)$$

$$Ch_i = F_h(i,A) = \min\{H, s, \max(0, H/2 + s/2 - |H/2 - y_i|)\} \quad (8)$$

$$C_i = Cw_i \times Ch_i \quad (9)$$

The overlap between any two sensors i and j can be calculated using Equations (10)-(12):

$$Ow_{ij} = \min\{Cw_i, Cw_j, \max(0, Cw_i/2 + Cw_j/2 - |Cx_i - Cx_j|)\} \quad (10)$$

$$Oh_{ij} = \min\{Ch_i, Ch_j, \max(0, Ch_i/2 + Ch_j/2 - |Cy_i - Cy_j|)\} \quad (11)$$

$$O_{ij} = Ow_{ij} \times Oh_{ij} \quad (12)$$

Assuming there are N sensors, the overall coverage contribution of the surveillance plan (CC_T) can then be calculated using Equations (13)-(15):

$$O_T = 1/2 \times \sum_{\{i \text{ in } 1..N, j \text{ in } 1..N, i \neq j, |x_i - x_j| \leq (w_i + w_j)/2\}} O_{ij} \quad (13)$$

$$C_T = \sum_{\{i \text{ in } 1..N\}} C_i \quad (14)$$

$$CC_T = C_T - O_T \quad (15)$$

Note that because the overlap between two sensors is counted twice in the O_T summation, for O_{ij} and for O_{ji} , this summation is divided by 2.

Platform Placement Process

The task of placing FoV projections on the virtual wall can be achieved by separating the wall into four segments and filling each one separately. Since each of these segments has a rectangular shape, it adheres to the assumptions established above, and qualifies for the developed overlap and coverage contribution computations. However, these four parts overlap at the corners, and so the platform positioning process has to avoid allocating duplicates for the same spots.

The P^3 heuristic model uses the virtual wall's four rectangular shapes. First assume that the side length of a sensor's range is larger or equal to the thickness of the virtual wall. Because a corner of the virtual wall is where the two segments meet, placing a sensor there yields the best use of the platform, as the sensor range leads to the highest Type 2 overlap possible. Therefore, the process starts by placing four towers in the four corners of the wall. The second step is to compute the CC_T for each segment and check whether the $CC_T \geq A_{segment} \times (1 - a)$ condition holds, where $A_{segment}$ is the area of the segment and a is the allowance for lack of coverage. If this condition is verified, the segment is finalized by stopping the associated iteration and recovering the original circular shape of the FoV projections, as depicted in Figure 8. If the condition is not verified, the process determines N new platforms that are to be added to the segment by computing N using Equation (16):

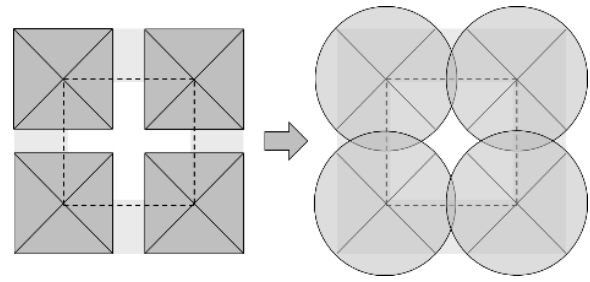


Figure 8. Solution for an Instance where Four Sensors Suffice to Provide Apt Coverage

$$N = \lceil (A_{segment} \times (1 - a) - CC_T) / (\min(H, s) \times s) \rceil \quad (16)$$

The process then continues by filling the uncovered surface by positioning the centroids of the newly added camera ranges on the line that passes through the centroids of the corner sensors' ranges, such that the adjacent ones are equidistant from one another, as shown in Figure 9.

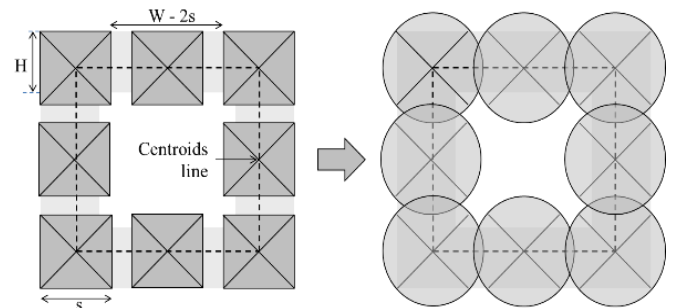


Figure 9. Solution for an Instance where a Layer of FoVs Suffices to Provide Apt Coverage

Consider the case where the thickness of the virtual wall is larger than the side length of the sensor's range, as depicted in Figure 10. If the coverage demand is not met, then the virtual wall is divided into a set of layers that have the same thickness. Given this division, each layer can be considered as a virtual mini wall. Subsequently, the previously described process can be applied to each layer separately in order to acquire a set of ranges whose centroids are all aligned in each segment.

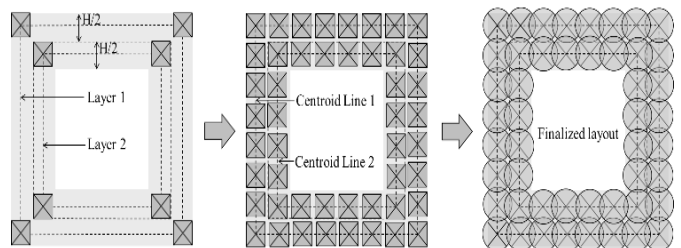


Figure 10. Solution for an Instance where Two Layers of FoVs Are Needed for Apt Coverage

Let M be the minimum number of layers required to meet the coverage demand. As long as $W \geq H$, M is acquired by dividing H , the height of the segment, by s , the length of the sensor's range side, as given in Equation (17):

$$M = H / s = T / s \quad (17)$$

Notice that the quotient of the division may contain a fraction. In this case, the floor of the number is used first; if it does not meet the coverage demand, then it is replaced by the ceiling. A holistic algorithm that positions the sensors inside the virtual wall may be compiled using the following steps:

0. Obtain the length of the sensor's range, s , and the virtual wall's established parameters—including width and height of the outer rectangle, coordinates of its center, allowance for lack of coverage, and its thickness.
1. Assign M the floor of T/s . If $M = 0$, then assign $M = 1$.
2. Divide the virtual wall into M layers.
3. For each of the M layers:
 - a. Place a sensor at each corner to maximize Type 1 overlap.
 - b. For each of the four mini-segments of the layer, compute the total coverage contribution, and check if the coverage demand is met.
 - c. For each of the four mini-segments that has insufficient coverage, place N additional sensors equidistantly along the centroids line.
4. If the overall coverage demand is met, finalize the constructed layout. Otherwise, assign M the ceiling of T/s and re-execute steps (2)-(4).

If the use of an aerostat is justified, the surveillance plan requires the employment of both aerostat and tower cameras. The approach for building a surveillance plan with one aerostat and a set of tower cameras can be divided into three steps:

1. Build a layout solution for a surveillance alternative that contains only mounted cameras.
2. Position the aerostat such that the center of its range coincides with the centroid of the virtual wall.
3. Remove the cameras whose coverage is deemed unnecessary (see example in Figure 11).

To explain the last step, consider two circular sensor ranges that overlap, as depicted in Figure 12. The line that passes through their centers intersects with their overlap in a segment whose length shall be called d_o . Then, d_o can be obtained by subtracting the distance between the two rang-

es' centers from the sum of their radii ($d_o = r_1 + r_2 - d$). Note that d_o is positively correlated with the intersection between the sensors and can, therefore, be employed as a means for determining whether or not the amount of overlap is considerable. To be more specific, if d_o is larger than a certain threshold, then the intersection area between the FoV projections is regarded as significant. If such a situation is identified when evaluating the overlap, the second platform is removed from the hybrid surveillance plan. This approach is iterated for each mounted sensor until the coverage provided by the aerostat and tower-mounted cameras is optimized.

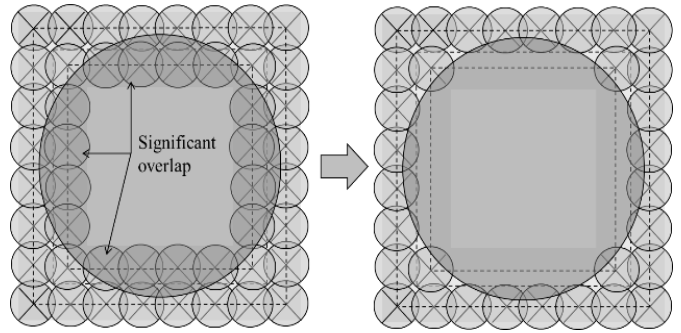


Figure 11. Solution for Tower-Mounted Cameras and Aerostat

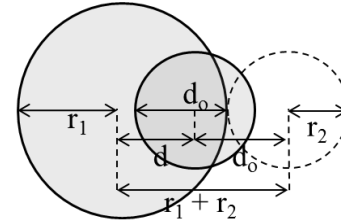


Figure 12. The Geometric Situation of Two Overlapping Circular Ranges with r_1 and r_2 as Radii

Case Study

The model described previously was applied on a geographical area to validate its output solution as well as showcase its powerful utility. The chosen area was in the Wanat region in Afghanistan, where combat outpost (COP) Kahler was located. This outpost was the target of an insurgent attack in 2008, which resulted in a number of casualties and wounded soldiers. Although the weak protection of the outpost may have been a contributor to the failed defense, it is believed that the geographical structure of the location and the fight against swift insurgents also played a significant role [14]. The virtual wall was designed based on the geo-location and 2D physical shape of the outpost. The wall was arranged around the center of the outpost to cover its irregular boundaries. The width and the height of the virtual

wall were set to 600m and 1000m in order to secure a large coverage. The thickness of the virtual wall varied (50m, 150m, and 250m) in the experiment in order to test the utility of the method in different tower placements with and without the use of an aerostat. Since tower FoV radii were $r_{ID} = 40m$, $r_{DD} = 160m$, and $r_{DV} = 640m$, varying the virtual wall's thickness would provide solutions with different numbers of tower layers, as noted earlier. Figure 13 shows the irregular borders of COP Kahler and the designed virtual wall with its parameters.

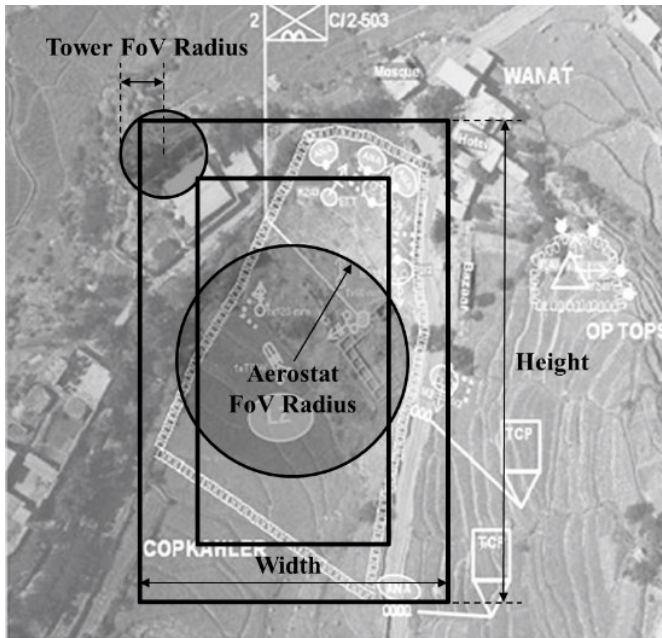


Figure 13. Borders of COP Kahler

The P^3 heuristic model was used to provide two solution alternatives, without and with the deployment of one aerostat that was tethered at the center of the outpost. Using these alternatives, two sets of experiments were conducted for different image resolution levels by changing the tower FoV radii and coverage allowance to analyze the number of required towers for virtual wall coverage. The results of the first set of experiments are given in Table 1, where the variable "a" represents allowance.

As delineated in the table, the number of towers was significantly higher when the tower FoV radius was kept at the dismount-identification level. When the tower FoV radius increased to the dismount-detection level or vehicle-detection level, the majority of the area was covered by the four towers that the model placed at the four corners of the wall. In addition, there was Type 2 overlap in many of those cases, especially at the vehicle-detection level, where the tower coverage was larger.

An intuitive result is that the number of towers increases significantly as the wall thickness increases or coverage allowance decreases. As the wall thickness increases, the area that towers must cover also increases; therefore, more towers are needed. Similarly, as the coverage allowance decreases, the uncovered area inside the wall also decreases and that also requires more towers. It was also observed that the number of towers decreased more rapidly at the dismount-identification level as the coverage allowance decreased. In order to investigate the sensitivity of the number of towers at the dismount-identification level, the data for different coverage allowances are plotted in Figure 14 with their respective regression lines.

Table 1. First Set of Experimental Results

Virtual Wall Thickness 50m				Virtual Wall Thickness 150m				Virtual Wall Thickness 250m			
Tower FoV Radii				Tower FoV Radii				Tower FoV Radii			
a	640	160	40	a	640	160	40	a	640	160	40
0%	4	4	50	0%	6	10	132	0%	4	16	188
5%	4	4	50	5%	4	10	128	5%	4	16	182
10%	4	4	46	10%	4	10	118	10%	4	12	168
15%	4	4	44	15%	4	10	114	15%	4	12	152
20%	4	4	40	20%	4	10	106	20%	4	10	144
25%	4	4	36	25%	4	6	96	25%	4	10	134
30%	4	4	36	30%	4	6	90	30%	4	10	126
35%	4	4	32	35%	4	6	84	35%	4	8	116
40%	4	4	30	40%	4	6	78	40%	4	6	108
45%	4	4	26	45%	4	6	68	45%	4	6	98
50%	4	4	26	50%	4	6	64	50%	4	6	90
55%	4	4	22	55%	4	4	56	55%	4	6	80
60%	4	4	20	60%	4	4	50	60%	4	4	70
65%	4	4	16	65%	4	4	44	65%	4	4	62
70%	4	4	14	70%	4	4	36	70%	4	4	52
75%	4	4	12	75%	4	4	30	75%	4	4	42
80%	4	4	10	80%	4	4	24	80%	4	4	36
85%	4	4	6	85%	4	4	18	85%	4	4	26
90%	4	4	4	90%	4	4	10	90%	4	4	16
95%	4	4	4	95%	4	4	8	95%	4	4	16
100%	4	4	4	100%	4	4	8	100%	4	4	16

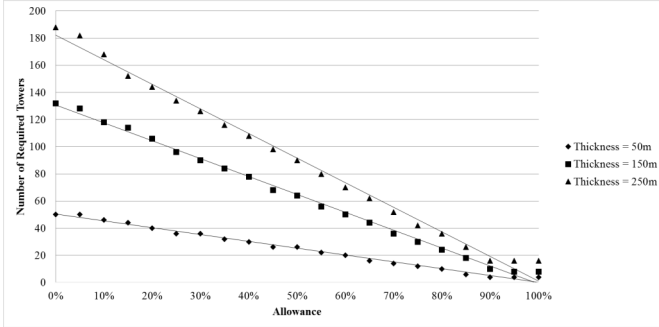


Figure 14. Number of Towers for Coverage Allowance Levels

Analyses on the figure and the regression line equations (R^2 values were higher than 99.21%) reveal that the sensitivity of the number of towers varied with respect to the square of the virtual wall thickness. A small increase in the coverage allowance resulted in a large decrease in the number of towers, when the virtual wall thickness was 250m. However, when the virtual wall thickness was 150m, the same amount of increase in the coverage allowance resulted in smaller decreases in the required number of towers. The number of required towers was even less when the virtual wall thickness was 50m. In addition, the number of towers decreased more rapidly when the coverage allowance was low for every virtual wall thickness. In contrast, there was minimal change when coverage allowance was 90% or higher.

The second set of experiments was conducted for the solution alternative that included one tethered aerostat and tower mounted cameras. The same variables as the first set were varied in order to investigate different solutions. Aerostat FoV radii were changed to $r_{ID} = 250m$, $r_{DD} = 1000m$, and $r_{DV} = 4000m$ for the dismount-identification level, dismount-detection level, and vehicle-detection level, respectively. During the experiment, it was observed that the aerostat provided 100% coverage over the outpost when the radius was set at the dismount-detection level or vehicle-detection level, due to its large coverage area. Therefore, the experimental results only at the dismount-identification level of aerostat coverage were considered for further analysis. The results are given in Table 2. The number of towers for different coverage allowances are shown in Figure 15 for the dismount-identification level along with their regression lines. As demonstrated in the table and the figure, the results of the second set of experiments were similar to those from the first set; the number of towers increased significantly as the virtual wall thickness increased or coverage allowance decreased. However, since the aerostat provided a certain coverage inside the virtual wall, the number of towers was relatively small for virtual wall thicknesses of 150m and 250m. When the wall thickness was 50m, however, there was no change in the number of towers with or without the

use of an aerostat. It was also observed that the minimum number of towers at higher coverage allowances were the same for the alternatives with or without the use of an aerostat. Analyses on regression line equations (R^2 values were higher than 98.41%) revealed that the sensitivity of the number of towers varied with respect to the square of the virtual wall thickness as in the first set of experimentation, but in a markedly more pronounced manner. The difference between the results of the two experiments are tabulated in Table 3 for further sensitivity analysis. The table shows the number of required additional towers when an aerostat is not used.

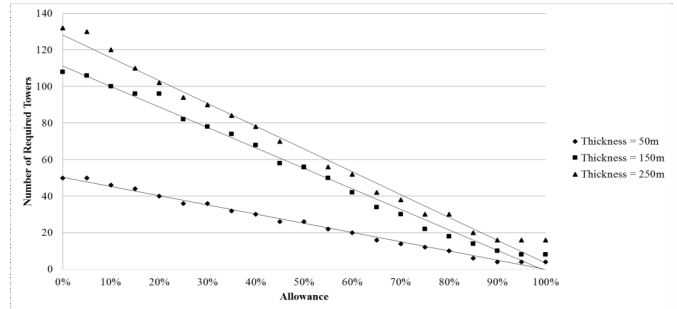


Figure 15. Number of Towers for Allowance Levels with Aerostat

Table 2. Second Set of Experimental Results for an Aerostat FoV Radius Equal to 250m

	Virtual Wall Thickness 50m			Virtual Wall Thickness 150m			Virtual Wall Thickness 250m					
	Tower FoV Radii	Tower FoV Radii	Tower FoV Radii	Tower FoV Radii	Tower FoV Radii	Tower FoV Radii	Tower FoV Radii	Tower FoV Radii	Tower FoV Radii			
	a	640	160	40	a	640	160	40	a	640	160	40
0%	4	4	50	0%	6	6	108	0%	4	6	132	
5%	4	4	50	5%	4	6	106	5%	4	6	130	
10%	4	4	46	10%	4	6	100	10%	4	6	120	
15%	4	4	44	15%	4	6	96	15%	4	6	110	
20%	4	4	40	20%	4	6	96	20%	4	6	102	
25%	4	4	36	25%	4	4	82	25%	4	6	94	
30%	4	4	36	30%	4	4	78	30%	4	6	90	
35%	4	4	32	35%	4	4	74	35%	4	4	84	
40%	4	4	30	40%	4	4	68	40%	4	4	78	
45%	4	4	26	45%	4	4	58	45%	4	4	70	
50%	4	4	26	50%	4	4	56	50%	4	4	56	
55%	4	4	22	55%	4	4	50	55%	4	4	56	
60%	4	4	20	60%	4	4	42	60%	4	4	52	
65%	4	4	16	65%	4	4	34	65%	4	4	42	
70%	4	4	14	70%	4	4	30	70%	4	4	38	
75%	4	4	12	75%	4	4	22	75%	4	4	30	
80%	4	4	10	80%	4	4	18	80%	4	4	30	
85%	4	4	6	85%	4	4	14	85%	4	4	20	
90%	4	4	4	90%	4	4	10	90%	4	4	16	
95%	4	4	4	95%	4	4	8	95%	4	4	16	
100%	4	4	4	100%	4	4	8	100%	4	4	16	

Table 3. Difference between the Two Experimental Results

Virtual Wall Thickness 50m				Virtual Wall Thickness 150m				Virtual Wall Thickness 250m			
Tower FoV Radii				Tower FoV Radii				Tower FoV Radii			
a	640	160	40	a	640	160	40	a	640	160	40
0%	0	0	0	0%	0	4	24	0%	0	10	56
5%	0	0	0	5%	0	4	22	5%	0	10	52
10%	0	0	0	10%	0	4	18	10%	0	6	48
15%	0	0	0	15%	0	4	18	15%	0	6	42
20%	0	0	0	20%	0	4	10	20%	0	4	42
25%	0	0	0	25%	0	2	14	25%	0	4	40
30%	0	0	0	30%	0	2	12	30%	0	4	36
35%	0	0	0	35%	0	2	10	35%	0	4	32
40%	0	0	0	40%	0	2	10	40%	0	2	30
45%	0	0	0	45%	0	2	10	45%	0	2	28
50%	0	0	0	50%	0	2	8	50%	0	2	34
55%	0	0	0	55%	0	0	6	55%	0	2	24
60%	0	0	0	60%	0	0	8	60%	0	0	18
65%	0	0	0	65%	0	0	10	65%	0	0	20
70%	0	0	0	70%	0	0	6	70%	0	0	14
75%	0	0	0	75%	0	0	8	75%	0	0	12
80%	0	0	0	80%	0	0	6	80%	0	0	6
85%	0	0	0	85%	0	0	4	85%	0	0	6
90%	0	0	0	90%	0	0	0	90%	0	0	0
95%	0	0	0	95%	0	0	0	95%	0	0	0
100%	0	0	0	100%	0	0	0	100%	0	0	0

The sensitivity analysis of the results revealed that when the virtual wall thickness was 250m at the dismount-identification level, the number of additional towers decreased linearly with respect to coverage allowance. As the allowance increased, the number of additional towers decreased. When the virtual wall thickness was 150m, however, the number of required additional towers did not change significantly with the increase in coverage allowance between 25% and 65%. If the coverage allowance was less than 25% or more than 65%, the number of additional towers increased significantly with an increase in allowance.

Conclusions

In this study, a unique analytical and flexible placement method for stationary military surveillance platforms was developed that used a heuristic model to evaluate and provide required coverage for outposts. The method is flexible in the sense that it is easy to customize the surveillance system for specific outposts with irregular borders. The method also allows the use of different types of sensors on different platforms. A surveillance architect can determine the shape and thickness of the virtual wall, provided that the image resolution level and the allowance percentage associated with the lack of coverage are known. The DoV can be changed for each platform, based on the specifications of different sensors for the required surveillance level. The method then determines the location of each platform, considering coverage areas and coverage overlap.

When the method was applied on the area of COP Kahler in Afghanistan, the results provided sufficient surveillance coverage under different assumptions and surveillance levels. The analyses of the results indicated the image resolution level, the virtual wall thickness, the coverage allowance, and the use of aerostats have impacts, to a certain degree, on the number of required towers to provide the desired surveillance. When there is no aerostat in the solution, a small change in the coverage allowance leads to a large decrease in the number of towers when the virtual wall is thicker. However, the change in the coverage allowance has less impact on the number of towers when the virtual wall is set to a thinner value. Therefore, the security level may be increased significantly with a small investment by using lower coverage allowance and adding new towers when the virtual wall must be thin due to geographical constraints. In contrast, when the virtual wall thickness may be set to a thicker value, the security level may be dropped slightly and very large savings may be realized by increasing the coverage allowance and using a smaller number of towers.

The deployment of an aerostat may not add a significant surveillance value if the virtual wall is not thick or the desired image resolution is low. On the other hand, the surveillance plan may not need the use of towers when an aerostat is employed and the image resolution is low. The number of required towers may be optimized by varying the coverage allowance with an established virtual wall thickness. As demonstrated in the case study, the number of required towers may not change significantly within certain coverage allowance levels. In that case, the security level may be maximized with a small investment by minimizing the coverage allowance within the limits and adding a small number of new towers to the surveillance plan.

References

- [1] Miles, D. (2006). Concept perfected in Iraq, Afghanistan Used along U.S. Border, National Guard American Forces Press Service. Retrieved from <http://www.nationalguard.mil/News/Article-View/Article/572837/concept-perfected-in-iraq-afghanistan-used-along-us-border>
- [2] The Washington Times. (2008). BRIEFING: FOBs the closest thing to home in Iraq. Retrieved from <http://www.washingtontimes.com/news/2008/mar/26/briefing-fobs-the-closest-thing-to-home-in-iraq>
- [3] Everly, R. E., Limmer, D. C., & MacKenzie, C. A. (2015). Cost-Effectiveness Analysis of Autonomous Aerial Platforms and Communication Payloads. In F. Melese, A. Richter, & B. Solomon (Eds.), *Military Cost-Benefit Analysis: Theory and Practice*, (401-423). Routledge, New York.
- [4] Air Combat Command. (2007). Tethered aerostat radar system. Retrieved from <http://www.acc.af.mil/About-Us/Fact-Sheets/Display/Article/199135/tethered-aerostat-radar-system>
- [5] Ruggles, R., & Ruggles, K. (2016). Using Lidar and Animation to Develop Surveillance Strategies. *International Journal of Engineering Research and Innovation*, 8(2), 46-53.
- [6] Hu, W., Tan, T., Wang, L., & Maybank, S. (2004). A Survey on Visual Surveillance of Object Motion and Behaviors. *IEEE Transactions on Systems, Man, and Cybernetics-Part C: Application and Reviews*, 34(3), 334-352.
- [7] Kumar, R., Sawhney, H., Samarasekera, S., Hsu, S., Tao, H., Guo, Y., et al. (2001). Aerial Video Surveillance and Exploitation. *Proceedings of the IEEE*, 89(10), 1518-1539.
- [8] Everly, R. E., & Limmer, D. C. (2014). Cost-Effectiveness Analysis of Aerial Platforms and Suitable Communication Payloads. (Thesis) *Naval Postgraduate School*, Monterey, California.
- [9] Rothkrantz, L., & Scholte, S. (2013). A Surveillance System of a Military Harbour Using an Automatic Identification System. *Proceedings of the 14th International Conference on Computer Systems and Technologies*, (pp.169-176). Ruse, Bulgaria.
- [10] Sinopoli, B., Sharp, C., Schenato, L., Schaffert, S., & Shankar Sastry, S. (2003). Distributed Control Applications Within Sensor Networks. *Proceedings of the IEEE*, 91(8), 1235-1246.
- [11] Arora, A., Dutta, P., Bapat, S., Kulathumani, V., Zhang, H., Naik, V., et al. (2004). A Line in the Sand: A Wireless Sensor Network for Target Detection, Classification, and Tracking. *Computer Networks*, 46, 605-634.
- [12] Yildiz, E., Akkaya, K., Sisikoglu, E., & Sir, M. (2014). Optimal Camera Placement for Providing Angular Coverage in Wireless Video Sensor Networks. *IEEE Transactions on Computers*, 63(7), 1812-1825.
- [13] Boonsuk, W. (2016). Investigating the Effects of Stereo Camera Baseline on the Accuracy of 3D Projection for Industrial Robotic Applications. *International Journal of Engineering Research and Innovation*, 8(2), 94-98.
- [14] Roggio, B. (2010). Army releases report on battle at Combat Outpost Keating, Long War Journal. Retrieved from http://www.longwarjournal.org/archives/2010/02/army_releases_report_on_combat.php

Biographies

NEBIL BUYURGAN is an associate professor of technology and construction management at Missouri State University. He earned his BS degree (Industrial Engineering, 1998) from Istanbul Technical University, Turkey, MS (Engineering Management, 2000) and PhD (Engineering Management, 2004) from the University of Missouri – Rolla. His research interests include logistics operations in healthcare, military, and retail. Dr. Buyurgan may be reached at NebilBuyurgan@MissouriState.edu

NABIL LAHLOU is a senior platform developer at Womply/Oto Analytics. He earned his BS degree (Computer Science, 2007), MS (Industrial Engineering, 2008), and PhD (Industrial Engineering, 2013) all from the University of Arkansas. Dr. Lehlou may be reached at nabil@otoanalytics.com

KEVIN M. HUBBARD is an assistant professor of technology and construction management at Missouri State University. He earned his BS degree (Aerospace Engineering, 1991), MS (Engineering Management, 1993), and PhD (Engineering Management, 1996), all from the University of Missouri – Rolla. His research interests include automation and device control, manufacturing systems, device design, and process optimization. Dr. Hubbard may be reached at KHubbard@MissouriState.edu

INFLUENCE OF BUILD ORIENTATION AND HEAT TREATMENT ON TENSILE STRENGTH OF EOS MARAGING STEEL MS1

Jennifer G. Michaeli, Old Dominion University; Amit Kulkarni, Old Dominion University; Roman Roxas, Old Dominion University

Abstract

The primary purpose of this study was to analyze the influence of build orientation on material properties in tension of EOS Maraging Steel MS1 parts, manufactured using additive manufacturing (AM), or more commonly known as 3D printing. The secondary purpose was to identify the feasibility of such parts for Navy applications. EOS Maraging Steel MS1 is a steel powder developed by EOS GmbH, which has been optimized for producing solid metal parts by using direct metal laser sintering (DMLS). Mechanical tests like hardness tests and tensile tests were conducted on as-built specimens in vertical (90°), horizontal (0°) and 45-degree (45°) build orientations, and on age-hardened specimens. Test results align well with the given range of published values by EOS GmbH; however, it was observed that the tensile strength greatly depends on the build orientation and heat treatment. The results are encouraging, though researchers advise additional testing on similar specimens to complete the recommendation for naval applications.

Introduction

Additive manufacturing (AM), often referred to as 3D printing, is a process in which an object, part, or component is built up layer by layer by adding material. This is in contrast to traditional so-called “subtractive” manufacturing methods. AM, though a relatively young technology, already displays numerous advantages over traditional manufacturing methods. Because of the speed, versatility, and flexibility of AM, low-production-run parts can be created cheaper and more quickly than ever before. Additionally, some AM methods have shown potential for reducing environmental impact, when compared to traditional production methods [1]. These examples represent only a small sample of the current benefits of using AM and just a glimpse of what is to come. AM is an emerging area for research and application that the Navy has been following for some time. Some naval leaders predict that 3D printers may one day be used on-board naval surface ships, essentially making them floating one-stop print shops and allowing naval personnel to print on demand while at sea [2]. This could be advantageous for the Navy in times of need. However, the Navy is a long way from accepting this technology into the fleet until

leadership has a better understanding of the technology’s benefits and limitations as well as how to standardize the capability and build up a logistical supply chain around it.

Though it seems that AM has a bright future, there are certainly some limitations. One of the largest hurdles that AM needs to overcome is that the parts are not generally as strong as those made by more conventional means. This is a substantial problem for those intending to use 3D-printed parts for actual use. However, recent studies have shown that properly treated printed metal parts have similar mechanical properties to traditionally manufactured material of the same type [3, 4]. Problems with certifying parts/printers and intellectual property concerns also limit uses for AM in the current marketplace. It is hoped that the research performed during the course of this project can address some of the current issues with AM technology and provide Navy leadership with more scientific evidence of the technology’s utility. Previous studies were made regarding the influence of processing parameters on the mechanical properties of AM [5]. Crococo et al. [6] made a similar investigation about the influence of build orientation on the fatigue strength of EOS Maraging Steel. Properties of parts manufactured by DMLS and conventional manufacturing were compared by Gratton [4]. In this current study, an effort was made to identify the feasibility of 3D-printed EOS Maraging Steel MS1 parts for Navy applications.

Mechanical Testing of the Specimen

Maraging steels are high-performance, heat-treatable steels typically used for aerospace applications and for injection molding tools [7]. They derive their name from the crystalline structure ‘mar’tensite, produced as a result of the aging process or precipitation hardening (heat treatment). Material properties of 3D-printed EOS Maraging Steel MS1 are identified using ASTM E8/E8M tensile tests and ASTM E18 hardness tests. Figure 1 shows the anatomy of the “dog-bone” test specimen, and Figure 2 shows an actual test specimen. Tensile and hardness tests were conducted on twenty-four dog-bone test specimens. Table 1 gives the specimen dimensions, while Table 2 lists their classification based on build orientation, heat treatment, and post-manufacturing processing. Each sample displayed minor imperfections, such as warp, extra material, color, and size.

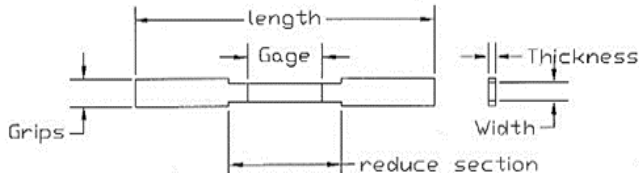


Figure 1. Anatomy of a Test Specimen

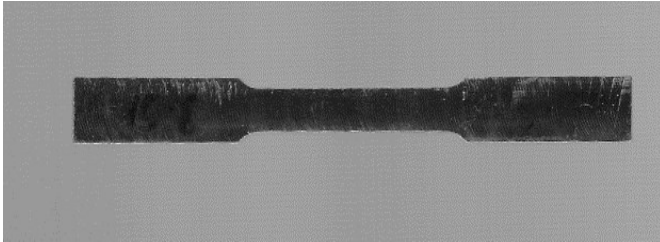


Figure 2. Actual Test Specimen

Table 1. Test-Specimen Dimensions

	Minimum (inches)	Maximum (inches)	Average (inches)
Width	0.2433	0.2567	0.2500
Thickness	0.0773	0.0887	0.0830
Total Length	4.2567	4.3267	4.2917
Gauge Length	0.9403	0.9763	0.9583

Table 2. Test-Specimen Classification

Specimen Group	Print Orientation	Modification	Quantity
V	Vertical	N/A	4
H	Horizontal	N/A	4
45	45 °	N/A	4
SS	N/A	Annealing	2
T	N/A	Tempering	10

To indicate print orientation, V, H, and 45 T were used, while SS indicated tempering and annealing heat treatment, respectively. The type-T specimens were tempered in a high-temperature vacuum furnace for six hours up to 490°C with a heating rate of 10°C per minute then air-cooled overnight. The type-SS specimens were annealed according to standard industrial process requiring the specimens to spend one hour in an oven at 815.5°C and then air cooled. The samples registered a hardness of around 32 HRC pre-annealing and around 32 HRC post-annealing.

Hardness Testing

Table 3 provides a summary of all test equipment. A Vickers hardness test was performed using a Shimadzu micro-hardness tester; the obtained Vickers Pyramid Number (HV) was converted to a Rockwell HRC value. The values were taken before and after age hardening. It is important to mention that the samples were too dark to test without polishing, even using different light sources, since the machine uses an optical viewfinder to calculate the HV. Only one side of the sample was polished so that the hardness value could be calculated. The test was performed on the grips of each sample at three different spots to get the average value. Table 4 gives the average hardness values for all heat-treated samples from the Vickers hardness test and Rockwell test with C scale.

Table 3. Test Equipment

Machine	Location	Description
MTS Alliance RF/300 Electromechanical Load Frame [8]	ODU main campus in Norfolk, VA	Electromechanical frame that is used to calculate tensile data
Shimadzu Vickers Micro-Hardness Tester Type M [9]	William and Mary's Lab co-located with ODU's ARC lab in Newport News, VA	Hardness tester that uses a pyramidal shape cone to indent specimen to calculate hardness
GSL-1100x High-Temperature Vacuum Tube Furnace [10]	ODU ARC lab in Newport News, VA	Furnace used to heat samples
Scanning Electron microscope JEOL JSM-6060LV [1]	ODU ARC lab in Newport News, VA	Used to take Microscopic images of sample
BUEHLER ECOMET VI Polisher/Grinder [11]	ODU ARC lab in Newport News, VA	A wet sander that grinds and polishes samples

Surface Preparation and Microscopic Imaging

A scanning electron microscope (SEM) was used to capture micrographs of the specimens before and after heat treatment. After heat treatment, specimens were subjected to wet grinding using 400-grit sandpaper as a part of surface preparation for microscopic imaging. It should be noted that even after grinding, surface unevenness was observed, as indicated in Figure 3 with the black banding and polished regions, due to the process (3D printing) used to manufacture the specimen.

Table 4. Average Hardness Values

	Specimen before hardening	Specimen after hardening	Vickers	Rockwell C
	Vickers	Rockwell C		
T-1	1244.3		644.3	57
T-2	331.7	34	556.7	52
T-3	357.0	36	571.0	53
T-4	338.0	34	668.3	58
T-5	353.7	36	608.3	55
T-6	348.3	35	629.3	56
T-7	352.3	36	601.7	55
T-8	356.0	36	591.7	54
T-9	287.3	28	581.3	54
T-10	331.3	33	625.0	56



Figure 3. Polished Specimen

Figure 4 shows micrographs of the T-1 specimen before heat treatment, while Figure 5 shows the SEM micrograph of the T-1 specimen after tempering. On close examination, micro-cracks and large particles near the cracks can be observed in Figure 3, which were transformed into small globules after heat treatment.

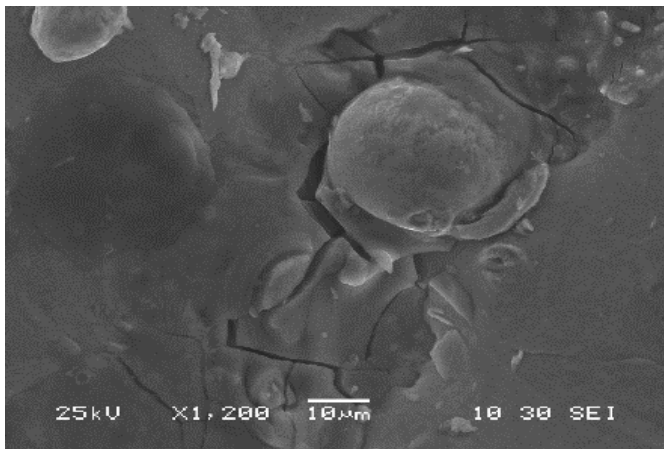


Figure 4. Specimen 1 before Heat Treatment at 1200 Magnification

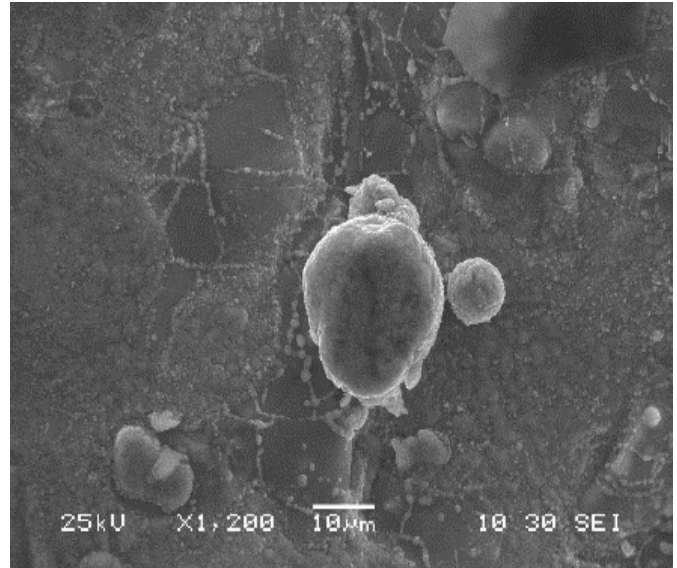


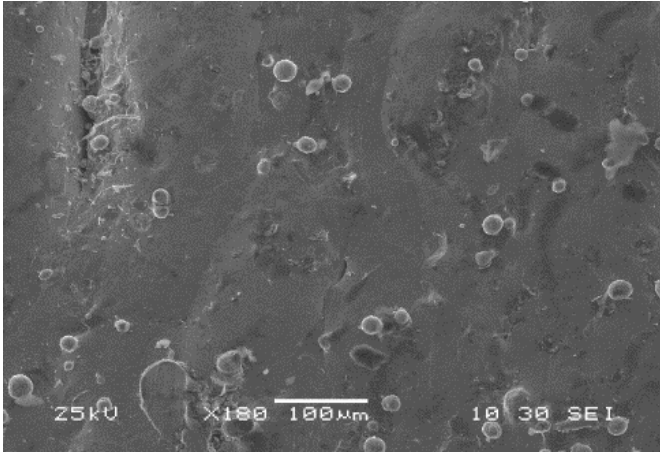
Figure 5. Specimen 1 after Heat Treatment at 1200 Magnification

Figures 6 and 7 show SEM micrographs for a representative type-T specimen, polished and unpolished, both before and after heat treatment. It should be noted that the micrographs were not take at the same location on the specimen before and after the heat treatment cycle. A common pattern for change in microstructure was observed in all of the cases.

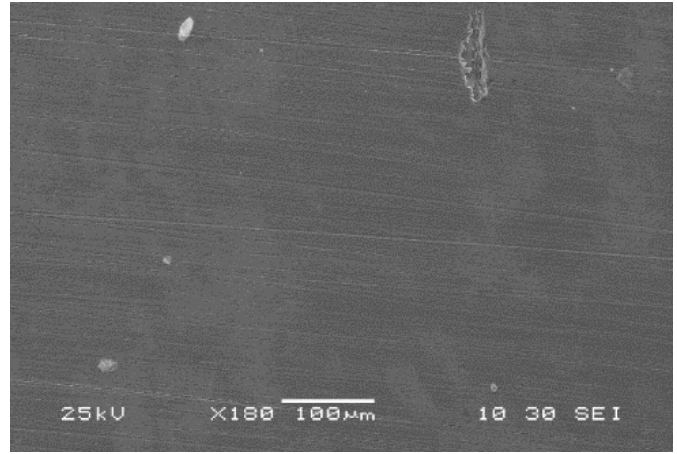
Tensile Testing Results

Tensile tests performed at room temperature are often used to predict material properties such as elasticity, ductility, yield strength, and ultimate tensile strength. An MTS Alliance RF/300 test frame was used for all tensile tests performed during this study. Test parameters were deduced according to the ASTM E8/E8 M standard. Strain was measured using the crosshead travel of the machine for most of the test specimens, and with a one-inch extensometer for the others. Table 5 shows the published properties by EOS GmbH for EOS Maraging Steel MS1 in tension.

Strain gauges were used to measure strain for only two specimens, V-8 and V-9, with little success, as the strain gauge peeled off of the specimen just shy of the elastic limit during the test. After testing all of the type-V and type-45 specimens, the data showed consistent values for peak load, peak stress, and modulus. A typical cup-and-cone failure was observed for non-heat-treated samples, whereas the stress-strain curve for heat-treated samples was parabolic in nature, a typical behavior of brittle materials. This can be seen in Figures 8 and 9, respectively.

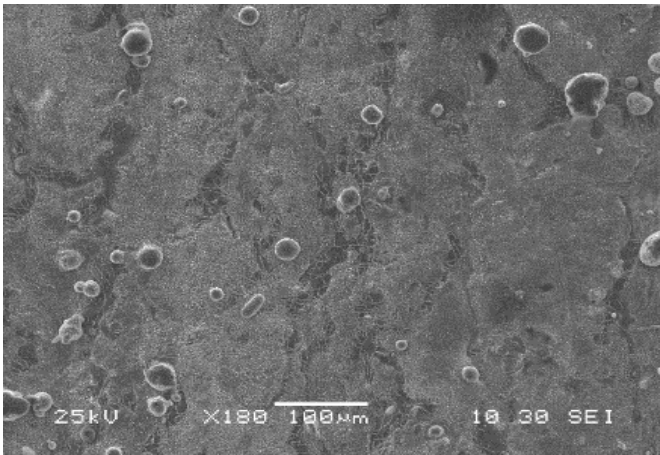


(a) Unpolished Specimen

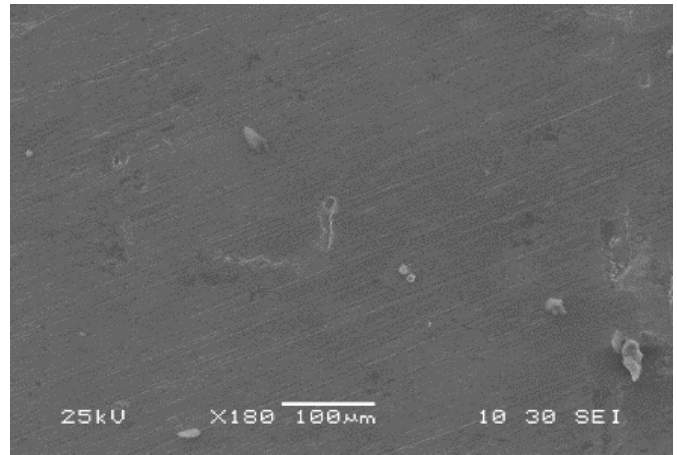


(b) Polished Specimen

Figure 6. Specimen T1 before Heat Treatment



(a) Unpolished Specimen



(b) Polished Specimen

Figure 7. Specimen T7 after Heat Treatment

Table 5. Published Properties of EOS Maraging Steel MS1 by EOS GmbH

	As built	After age hardening
Tensile Strength		min. 280 ksi
H	typ. 160 ± 15 ksi	
V	typ. 160 ± 15 ksi	typ. 297 ± 15 ksi
Yield Strength		min. 270 ksi
H	typ. 152 ± 15 ksi	
V	typ. 145 ± 15 ksi	typ. 289 ± 15 ksi
Hardness (HRC)	typ. 33-37 HRC	typ. 50-56 HRC



Figure 8. Type-V Specimen Necking (ductile behavior)



Figure 9. Type-T Specimen with a Sharp Edge (brittle behavior)

Tests without Extensometers

The samples in the type-V group had good performance, matching up with the properties in the given data sheet. Visually, the V specimens also exhibited greater necking, compared to all of the samples, although the samples in the type -45 group had the most elongation, based on the crosshead data. Samples in the V group failed in a typical cup-and-cone fashion, whereas samples in group 45 failed at a 45-degree angle, the orientation at which they were printed. Specimens V-7 through V-9 were tested in-house, while V-10 was tested at the Applied Technical Services lab. The T specimens underwent a brittle fracture and did not exhibit much necking. Table 6 and Figures 10 and 11 show samples and their results that were tested with no extensometers.

Table 6. Results without Extensometer

Sample	Peak Load (lbf)	Peak Stress (ksi)	Strain at break (%)	Modulus (ksi)
V-7	3379.38	105.60	12.16	1615.17
45-7	3484.43	174.90	35.57	1182.12
T-1	5799.85	269.20	11.80	3125.81
T-2	5747.06	250.6	12.97	2754.57
V-10	3367.52	153.85	NA	2480.00

Tests with Extensometers

Tensile tests were conducted using one-inch MTS axial extensometers on type H group samples, shown in Figure 12. While testing one of the samples (H-7) it was noticed that the data was more accurate on the graph compared to the strain data from cross head measurements. Using the extensometer gives a more precise data output from the test.

Also the extensometer shows the moment the sample breaks because of the sudden change in extension. It was also noticed that using the extensometer changed the values for the modulus compared to our previous test. Researchers believe this discrepancy arises from backlash caused during the specimen failure and also due to the very thin size of the specimens.

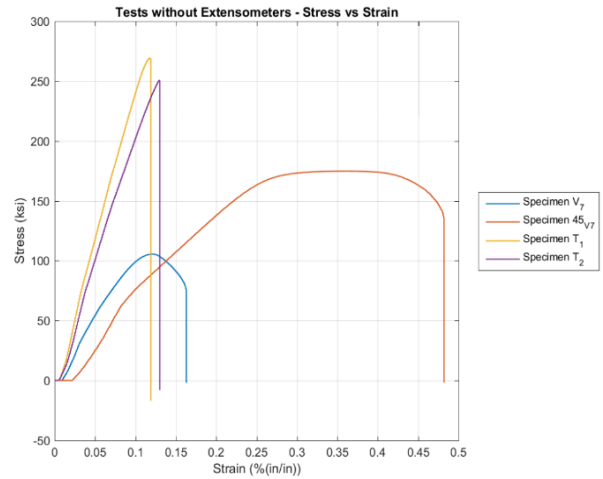


Figure 10. Tests without Extensometers

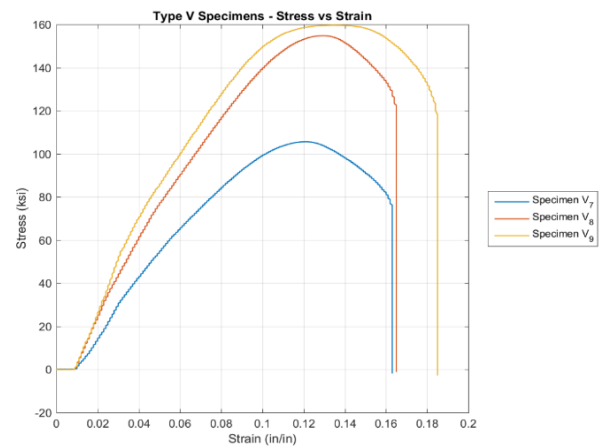


Figure 11. Standard Stress-Strain Curve for Type-V Specimens

Results of Hardened Samples

The type-T group specimens were also tested with the extensometer, with the exception of two samples. It was observed that extensometer slippage depended on the grips used to hold it together in place. Rubber bands are a good alternative to springs. Some of the graphs from the T sam-

ples show exactly where the extensometer was slipping and the extension during the tests. It was observed that heat treatment improved material properties such as peak load, peak stress, and hardness. Table 7 and Figures 13 and 14 show the results of the sample. The heat-treated samples endured a force between 5000 lbf to 6200 lbf. The non-heat-treated samples endured 3379 lbf to 3730 lbf. It can be seen that the tensile strength of age-hardened specimens was 267.21 ksi, with a minimum of 232.1 ksi and a maximum of 280.6 ksi, whereas the published value for the same is 280 ksi. Table 8 shows the results for all of the specimens tested.

Table 7. Results with Extensometer

Specimen	Peak Load	Peak Stress	Strain at	Modulus
V-7	3379.38	105.6	12.16	1615.17
V-8	3479.34	158.8	12.94	2202.15
V-9	3649.84	159.7	13.5	1565.4
V-10	3368.0	117.0	na	na
45-7	3484.43	174.9	35.56	1186.12
45-9	3521.62	172.1	13.77	2795.89
45-10	3592.72	168.5	13.13	2798.89
H-7	3689.73	173.8	3.63	34404.97
H-8	3729.1	172.5	2.92	29286.99
H-9	3668.02	162.1	2.76	25459.62
H-10	3730.68	169.6	4.05	29771.04
T-1	5799.85	269.2	11.8	3125.81
T-2	5754.05	250.6	12.96	2754.57
T-3	5962.96	267.4	1.3	32076.92
T-4	6098.43	278.1	1.39	26552.85
T-5	6012.31	270.2	1.18	25990.52
T-6	6250.26	279.6	1.43	32416.59
T-7	6172.53	274.5	1.58	33719.12
T-8	5236.32	232.1	0.87	30193.82
T-9	6073.81	270.0	1.37	29842.37
T-10	6200.44	280.4	1.51	28400.91

Table 8. Physical Properties for All of the Test Specimens

Sample	Peak Load (lbf)	Peak Stress (ksi)	Strain at Break (%)	Modulus (ksi)	Hardness (HRC)
T-1	5799.85	269.20	11.80	3125.81	57
T-2	5747.06	250.60	12.96	2754.57	52
T-3	5962.96	267.40	1.30	32076.93	53

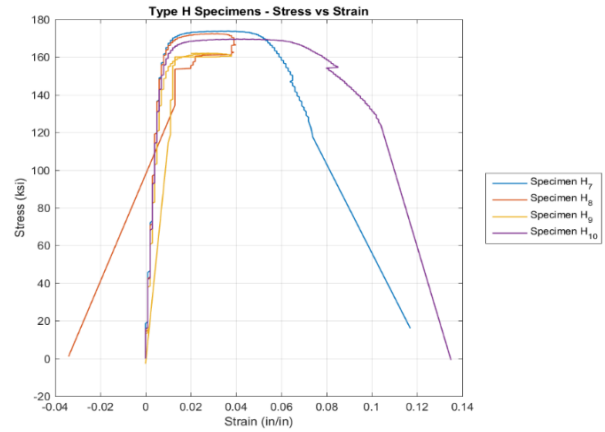


Figure 12. Standard Stress-Strain Curve Type-H Specimen

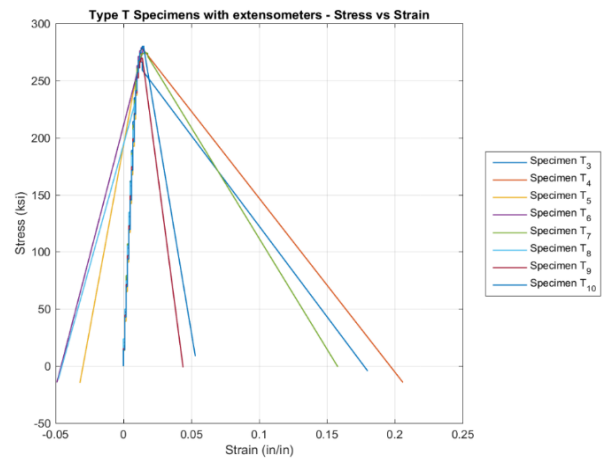


Figure 13. Crosshead-Extensometer Stress-Strain Curve for Type-T Specimens

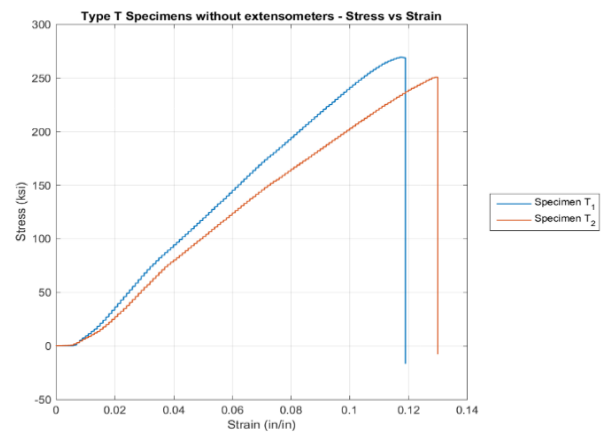


Figure 14. Standard Stress-Strain Curve for Type-T Specimens

Conclusions

Printing direction plays an important role in the physical properties of 3D-printed components using EOS Maraging Steel. Table 8 shows the standard physical properties of EOS Maraging Steel, while Table 7 shows the physical properties of the test specimens. Tensile strength of type-V and type-H specimens ranged from a minimum of 105.6 ksi to a maximum of 173.8 ksi, as compared to the tensile strength of 160 ± 15 (ksi) of as-built MS1. Tests on age-hardened specimens (type T) indicated an average tensile strength of 267.1 ksi. The results are encouraging. Exploration of additive manufacturing for shipboard maintenance applications will benefit from the results of this test program. The authors plan to continue to investigate uses for EOS Maraging Steel and expand the research to include other materials suitable for naval applications.

Acknowledgements

The authors acknowledge the US Navy for funding this work.

References

- [1] Amazing nano world. Retrieved from <http://www.jeol.co.jp/en>
- [2] Joyce, J. (2016). Navy Officials: 3-D Printing to Impact Future Fleet with 'On Demand' Manufacturing Capability. Retrieved from <http://www.navy.mil>
- [3] Yasa, E., Kempen, K., Kruth, J.-P., Thijs, L., & Van Humbeeck, J. (2010). Microstructure and mechanical properties of maraging steel 300 after selective laser melting. *Solid Freeform Fabrication Symposium Proceedings*. Austin, TX.
- [4] Gratton, A. (2012). Comparison of Mechanical, Metallurgical Properties of 17-4PH Stainless Steel between Direct Metal Laser Sintering (DMLS) and Traditional Manufacturing Methods. *2012 NCUR*.
- [5] Hanzl, P., Zetek, M., Baksa, T., & Kroupa, T. (2015). The influence of processing parameters on the mechanical properties of SLM parts. *Procedia Engineering*, 100, 1405-1413.
- [6] Crococo, D., De Agostinis, M., Fini, S., Olmi, G., Vranic, A., & Ciric-Kostic, S. (2016). Influence of the build orientation on the fatigue strength of EOS maraging steel produced by additive metal machine. *Fatigue & Fracture of Engineering Materials & Structures*, 39(5), 637-647.
- [7] Shellabear, M. and Nyrhila, O. Undated. *Materials for Direct Metal Laser-Sintering*, White Paper, EOS GmbH.
- [8] MTS Testing Systems. Retrieved from <https://www.mts.com/en/index.htm>
- [9] Shimadzu Testing Systems. Retrieved from <http://www.shimadzu.com>
- [10] Furnace Heating Module. Retrieved from <http://www.mtixtl.com/FurnaceModuleforGSL-1100X-EQ-GSL1100-Module-110V.asps>
- [11] Tabletop grinder-polisher. Retrieved from <https://shop.buehler.com/grinding-polishing>

Biographies

JENNIFER G. MICHAELI, PE is an assistant professor at Old Dominion University with joint appointment at the Virginia Modeling, Analysis and Simulation Center (VMASC) at the Batten College of Engineering and Technology (BCET). Dr. Michaeli, an SNAME Fellow, is the 2017 recipient of the State Council of Higher Education of Virginia (SCHEV) Rising Star award. At ODU, she has received the BCET Excellence in Research award. She is actively engaged in funded research with the US Navy and shipbuilding industry. Prior to ODU, Dr. Michaeli worked in the naval enterprise and marine industry. For her technical contributions in her field, she is a recipient of the ASNE Young Engineer of the Year award and the Navy's RADM Melville award for outstanding technical achievement. Dr. Michaeli completed her PhD in mechanical engineering from ODU, her MSc in ocean systems management from MIT, and her BSc in naval architecture and marine engineering from the Webb Institute. She is a licensed professional engineer in Virginia. Dr. Michaeli may be reached at jgmichae@odu.edu

AMIT KULKARNI is a PhD candidate at Old Dominion University in the Mechanical and Aerospace Engineering Department. He may be reached at akulkarn@odu.edu

ROMAN ROXAS is an undergraduate research engineering student in the Mechanical and Aerospace Engineering Department. He may be reached at rroxa003@odu.edu

PATTERN LEARNING FOR ECONOMICAL PROSTHETIC HANDS USING LEAP MOTION SENSORS

Wutthigrai Boonsuk, Eastern Illinois University; Noah C Przygoda, Eastern Illinois University

Abstract

The prosthetic hand is an artificial device for assisting people with disabilities achieve independence in their daily tasks. Today, prosthetic hands can be integrated with new innovative technologies and advanced materials that mimic the real human hand in terms of functionality and controllability. However, these advanced prosthetic hands are not affordable for most people who need them, or they are too costly an investment for young children who need to resize as they grow up. Thus, there are still major demands in lower-cost prosthetic hands as well as open-source prostheses proposed in many research studies. Because economical prosthetic hands are focused on the cost of their components, they usually lack user-friendly interfaces to operate or customize their functions for individual needs. The system proposed in this paper is intended to reduce the prosthetic hands' setup complexity by incorporating Leap Motion sensors that allow more natural human-machine interaction and require few to no additional user skills for customizing the functionality of their prosthetic hands.

Introduction

Advances in material science, neuron research, and engineering technology have enabled the development of prosthetic hands that can mimic real human hands in terms of their functionality and controllability. The i-LIMB Ultra prosthetic hand from Touch Bionics, for instance, has the appearance and movement close to those of a real hand [1, 2]. Bebionic from Ottobock is another commercial prosthetic hand that is designed for full functionality, strength, and an appearance similar to the real hand [3, 4]. Both prosthetic hands can be directly controlled by the user's muscles via myoelectric control. However, these prosthetic hands cost anywhere between \$25,000 and \$60,000, so they are not affordable for a majority of Americans with disabilities. According to the American Community Survey (Americans with Disabilities Act Participatory Action Research, 2014), the median income for individuals with a disability in 2014 was \$20,250 [5]. Thus, there is extensive demand for lower-cost prosthetic hands in the market. As an alternative, many researchers have undertaken open-source prosthesis projects with the main goal of providing lower-cost prosthetic hands. Several projects have taken advantage of inexpensive electronic components and 3D printing technology to make these hands more accessible, such as the Open Hand Project

[6], Robohand [7], E-Nable [8], OpenBionics [9], and Tact Hand [10].

Designs of both commercial and open-source prosthetic hands have demonstrated the potential for performing common tasks, such as the basic grasp, pinch, and power grip. While a variety of grip patterns has been offered, it is difficult and inconvenient for users to expand or customize their own patterns for use in performing different tasks. For commercial prosthetic products, users can work with manufacturers willing to assist them customizing the grip patterns for individual usage. In contrast, for open-source prosthetic hands, users must have sufficient knowledge to develop their own computer program codes to modify the prosthetic hands' grip patterns. This presents a major difficulty and hinders users unfamiliar with computer technology to fully and independently utilize their prosthetic hands. In this paper, the authors present a system that enables users to customize and expand the utilization of their prosthetic hands.

Methods

The grip pattern is the arrangement of fingers and hand that forms a pattern used for a specific purpose. Previous studies presented several methods that can be used to develop new grip patterns for prosthetic hands, including directly recording electromyography (EMG) signals, pattern learning gloves, and coding computer programs. EMG signals have traditionally been used for clinical study and diagnosis of neuromuscular disease. For prosthetic hands, these signals can be used to control the desired fingers independently and create particular grip patterns [11]. Pattern learning gloves use motion sensors to capture movements of human hand posture and, at the same time, the system also records EMG signals from the muscles [12, 13]. This method provides an easier way to develop a new grip pattern, but individual adjustment is still needed. The first two methods require an EMG system to capture muscle signals. However, current EMG systems are expensive and only available for commercial or research use, which poses limitations for individual users. Coding methods are usually available in lower-cost prosthesis hands in which a computer program is used to control mechanical movement of the fingers. This method requires the user to have computer programming skills and can be difficult for an average user. In this current study, the authors attempted to address the programming limitation in open-source prosthetic hands using Leap Motion sensors.

In term of usage, commercial prosthetic hands, such as the i-LIMB and Bebionic, come with a limited number of default grip patterns (24 grips and 14 grips, respectively). Users can trigger individual grip patterns via EMG signals (i.e., muscle signals in their limb to move the prosthetic devices). In addition, they can send a trigger via an application control in their smart device using Bluetooth communication. For open-source prosthetic hands, grip patterns are usually controlled by electronic pulses through either switches or microcontrollers. For example, OpenBionics provides six default grip patterns and allows users to pre-define new patterns by modifying an array of input finger positions (0–100) in the program code [14]. As mentioned earlier, this process can be difficult for users unfamiliar with computer programming. Thus, the system proposed here focuses on providing a user-friendly interface for grip pattern manipulation and the ability to expand the custom library of individual grip patterns.

Figure 1 shows the main components of the proposed system, which consists of a) a Leap Motion device [15], b) a computer, c) a low-cost microcontroller, and d) a bionic hand. The flow diagram in Figure 2 illustrates the system process steps.

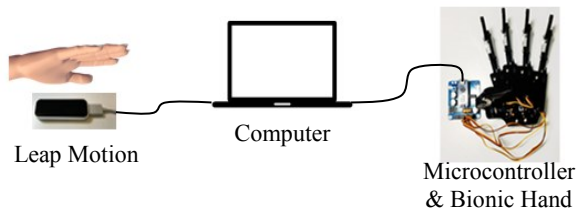


Figure 1. Main Components of the Proposed System

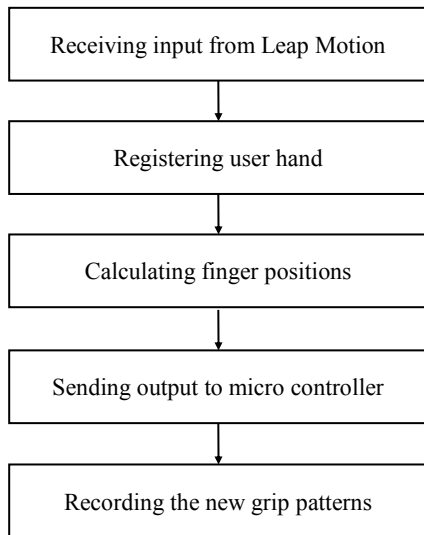


Figure 2. Flow Diagram of Process Steps

The Leap Motion device is a sensor that allows real-time input from the hand and finger motions (see Figure 3). This sensor uses two monochromatic IR cameras and three infrared LEDs to detect and recognize the user’s hand up to one meter in front of the device. In the first process step, the data collected from the sensor is passed to the computer in which Leap Motion SDK software is installed [16]. The software first registers the user’s hand by interpreting data from the sensor, such as the tip of each finger and their respective motions. The data are normalized so the system can automatically recognize different hand and finger sizes. This allows both people with disabilities and their caregivers to use the system. The software then determines the finger position and generates an output message (threshold scaled 0–100) regarding finger motion from closed to open positions. When the microcontroller receives an output from the computer, it creates pulse signals to control the servo motors on the bionic hand. The proposed system uses Arduino Nano and SunFounder servo controller boards, due to their compact sizes and ability to connect up to 12 servo motors (see Figure 4). A low-cost robot claw (left hand) was used in this study to simulate the mechanical control of the bionic hand (see Figure 5). The proposed system can be easily adapted to different bionic hands that use a similar controlling method.



Figure 3. Leap Motion Device

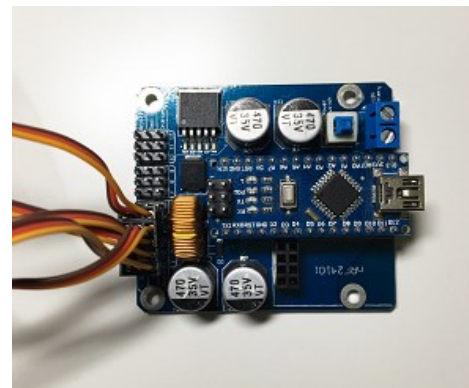


Figure 4. Arduino Nano and SunFounder Servo Controller Boards

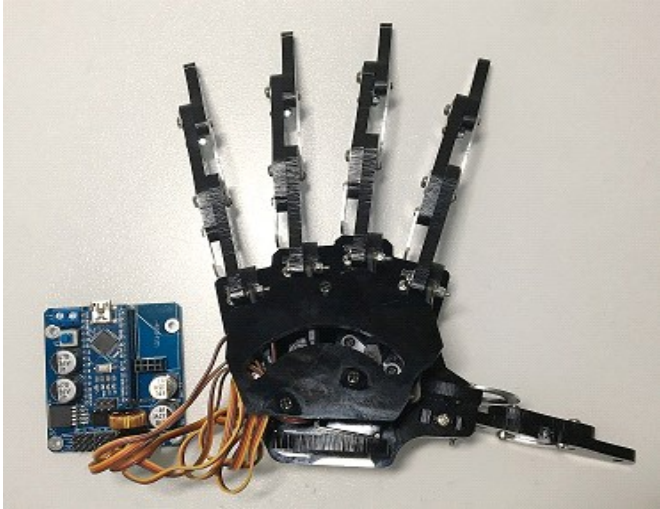
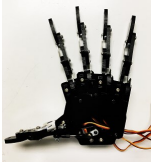


Figure 5. Low-cost Robot Claw

With the proposed system, users can manipulate the grip pattern by moving all of their fingers simultaneously. The fingers of the robot claw are adjusted according to the threshold, scaled from zero (closed position) to 100 (open position). Table 1 shows examples of finger positions adjusted to the threshold values, which, from left to right, represent the positions of the thumb, index, middle, ring, and pinky fingers. Note that the threshold scale number may not reach zero or 100 in actual practice, due to the hand stability and position relative to the sensor.

After the user sets the new grip pattern, the data are then stored in the computer as a text file in the format shown in Figure 6. For example, p3 represents pattern number three, which has a set of thresholds—99, 51, 47, 97, and 96—for the thumb, index, middle, ring, and pinky fingers, respectively.

Table 1. Examples of Finger Positions According to the Threshold Values

Threshold Values	Finger Positions of Robot Claw		
0,0,0,0,0			
100,100,100,100,100			
50, 50, 50, 50, 50			
0,0,100,100,100			
100,100,0,0,100			

```

Untitled - Notepad
File Edit Format View Help
p1:98,96,97,94,98
p2:52,35,98,98,94
p3:99,51,47,97,96

```

Figure 6. Data Format for Grip Patterns

The new pattern data in this text file is then used to generate a code that can be stored in the Arduino’s memory. By using the proposed system, users can easily and independently configure and develop new grip patterns of their own. Custom libraries of individual grip patterns can be simply constructed with the proposed system. Several methods can be used to trigger new patterns, such as a smart device [17] or RFID sensor [18].

Experiment and Discussion

To determine the accuracy and repeatability of the proposed system, an experiment was conducted. Due to the mechanical limitations of the robot claw used in this study, three common grip patterns (see Figure 7) were selected for use in this experiment: 1) open palm, 2) hook hand, and 3) finger point. In the experiment, the robot claw was first set to an idle position in which all fingers were closed (all threshold values were equal to zero). The operator’s hand was registered on the proposed system by opening and closing the hand several times in front of the Leap Motion sensor. The operator was told to make the pattern as close as possible to the given pattern. The threshold data were recorded after the operator reached the desired position. Each grip pattern was repeated 10 times, and each time the robot claw was set to the idle position. To analyze the experimental results and determine the accuracy and repeatability of the system, a repeated-measures analysis of variance (ANOVA) was used. Overall, there was no statistical difference (p -value > .05) between the repeated patterns in the experiment, as summarized in Table 2. Although the hook hand pattern showed no statistical difference in the ANOVA results, its p -value was the lowest and closest to 0.05. This pattern was, in fact, difficult to replicate, due to the lack of any actual reference points for the fingers. However, this difficulty should not present a problem for users developing their own custom grip patterns with the proposed system.

Table 2. Results from ANOVA

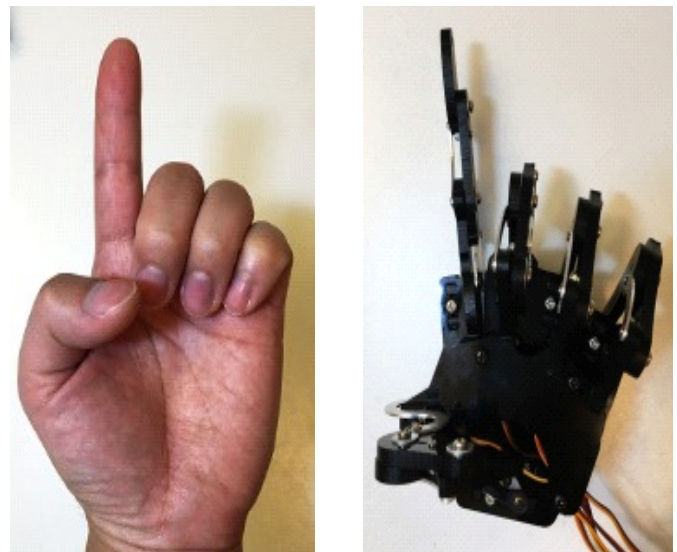
Grip Pattern	$F(1, 9)$	p -value
Open Palm	.192	.684
Hook Hand	5.370	.081
Finger Point	.004	.951



(a) Open Palm



(b) Hook Hand



(c) Finger Point

Figure 7. Grip Patterns in the Experiment

Conclusions

The system proposed in this paper allows people with disabilities, or their caregivers, to easily and independently develop new prosthetic grip patterns that are suited to their individual needs. The Leap Motion sensor was adopted in this system in order to eliminate any complex procedures and the need for computer programming knowledge to customize the grip patterns. This system can be implemented in both commercial and open-source prostheses to provide a more intuitive and user-friendly human-machine interface and to reduce associated costs. This study experimentally validated the accuracy and repeatability of the proposed system. Based on the results, this system has potential not only for the application described in this paper, but also for other applications, such as robotics control systems and teleoperations. Future work can provide benchmarking between the proposed method and existing systems in terms of functionality, durability, and user experience.

References

- [1] Otrand, V. D. N., Heleen, O. A., Bongers, R. M., Bouwsema, H., & Sluis, C. (2010). The i-LIMB hand and the DMC plus hand compared: A case report. *Prosthetics and Orthotics International*, 34(2), 216-220.
- [2] Touch Bionics by OSSUR. (n.d.). Retrieved from <http://www.touchbionics.com>
- [3] Medynski, C., & Rattray, B. (2011). BeBionic Prosthetic Design. *Proceeding of the 2011 MyoElectric Controls/Powered Prosthetics Symposium Fredericton*. New Brunswick, Canada.
- [4] BeBionic into the future with Ottobock. (n.d.). Retrieved from <http://bebionic.com>
- [5] American Psychological Association. (2017). *Disability & Socioeconomic Status*. Washington, DC.
- [6] Gibbard, J. (2013). OPEN HAND PROJECT. (n.d.). Retrieved from <http://www.openhandproject.org>
- [7] Gretsch, K. F., Lather, H. D., Peddada, K. V., Deeken, C. R., Wall, L. B., & Goldfarb, C. A. (2015). Development of novel 3D-printed robotic prosthetic for transradial amputees. *Prosthetics and Orthotics International*, 40(3), 400-403.
- [8] Kuehn, B. M. (2016, January 26). Clinicians Embrace 3D Printers to Solve Unique Clinical Challenges. *Medical News & Perspective*, 315(4), 333-335.
- [9] Liarokapis, M. V., Zisimatos, A. G., Mavrogiannis, C. I., & Kyriakopoulos, K. J. (2014). Openbionics: An Open-Source Initiative for the Creation of Affordable Modular, Light-Weight, Underactuated Robot Hands and Prosthetic Devices. *2nd ASU Rehabilitation Robotics Workshop*.
- [10] Slade, P., Akhtar, A., Nguyen, M., & Bretl, T. (2015). Tact: Design and Performance of an Open-Source, Affordable, Myoelectric Prosthetic Hand. *2015 IEEE International Conference on Robotics and Automation (ICRA)*, (pp. 6451-6456). Seattle, WA.
- [11] Fukuda, O., Tsuji, T., Kaneko, M., & Otsuka, A. (2003). A Human-Assisting Manipulator Teleoperated by EMG signals and Arm Motions. *IEEE Transactions on Robotics and Automation*, 19(2), 210-222.
- [12] Su, Y., Allen, R., Geng, D., Burn, D., Brechany, U., Bell, G. D., et al. (2003). 3-D motion system ("data-gloves"): application for Parkinson's disease, *IEEE Transactions on Instrumentation and Measurement*, 52(3), 662-674.
- [13] Rossi, M., Santina, C. D., Piazza, C., Grioli, G., Catalano, M., & Biechi, A. (2017). Preliminary results toward a naturally controlled multi-synergistic prosthetic hand, *2017 International Conference on Rehabilitation Robotics (ICORR)*, (pp. 1356-1363). London.
- [14] Grip Patterns. (n.d.). Retrieved from <https://www.openbionics.com/obtutorials/artichoke-grip-patterns>
- [15] Weichert, F., Bachmann, D., Rudak, B., & Fisseler, D. (2013). Analysis of the Accuracy and Robustness of the Leap Motion Controller. *Sensors*, 13(5), 6380-6393.
- [16] Spiegelmock, M. (2013). *Leap Motion Development Essentials*. Packt Publishing.
- [17] Benatti, S., Milosevic, B., Farella, E., Gruppioni, E., & Benini, L. (2017). A Prosthetic Hand Body Area Controller Based on Efficient Pattern Recognition Control Strategies. *Sensors*, 17(4), 869.
- [18] Vilarino, M. (2013). *Enhancing the Control of Upper Limb Myoelectric Prostheses using Radio Frequency Identification* (Master's thesis). Retrieved from <https://jscholarship.library.jhu.edu/handle/1774.2/37117>

Biographies

WUTTHIGRAI BOONSUK is an assistant professor of applied engineering and technology at Eastern Illinois University. He earned his master's and doctorate degrees in industrial and manufacturing system engineering from Iowa State University. Dr. Boonsuk also received his second master's degree in human computer interaction from the same university. His research interests include 3D stereoscopic applications, manufacturing systems, rapid prototyping, robotic and controller systems, virtual reality, and geographic information system (GIS). Dr. Boonsuk may be reached at wboonsuk@eiu.edu

NOAH PRZYGODA is a graduate student in the School of Technology at Eastern Illinois University. He earned his BS degree in applied engineering and technology in 2016 from Eastern Illinois University. Mr. Przygoda is currently enrolled and completing a dual MS degree program in sustainable energy and technology management at Eastern Illinois University. His research interests include sustainability, project management, energy management, and automation. Mr. Przygoda may be reached at ncprzygoda@eiu.edu

IMPROVING THE COOLING EFFICIENCY OF PRE-EXISTING RESIDENTIAL AIR CONDITIONING SYSTEMS

Ming Li, University of Michigan-Flint; Ayo Abatan, Miami University; Derick Robinson, Miami University; Jeff Weller, Miami University; Matthew Bello, Miami University

Abstract

As air conditioning becomes the norm in all regions of the U.S., it consumes an ever greater chunk of a household's electricity use each year. In 2016, space cooling accounted for 18% of the 1415 billion kilowatt-hours of electricity consumed by the residential sector. Switching to high-efficiency air conditioners can reduce energy use and carbon dioxide emissions. However, less-efficient air conditioning units running for decades have not been phased out mainly because of financial issues. The objective of this study was to develop simple and cost-effective methods for improving the cooling efficiency of pre-existing air conditioning systems. The authors carried out experiments on improving heat transfer and reducing cooling load of a central air conditioning system by misting the condenser and controlling window shades automatically based on sunlight.

Introduction

The United States Energy Information Administration (EIA) estimated that about 1410 billion kilowatt-hours (kWh) of electricity was consumed by the residential sector in 2016, of which 18% was used for space cooling [1]. It is estimated that more than three-quarters of all homes in the U.S. have air conditioners, which use about 6% of all the electricity produced in the U.S. and cost homeowners about \$29 billion every year [2]. Approximately 117 million metric tons of carbon dioxide are emitted into the atmosphere each year, due to the running of AC units [2]. Thus, improving the efficiency of air conditioners can benefit both economy and environment. Switching to high-efficiency air conditioners and taking other actions to reduce cooling loads can save as much as 50% of home energy use [3, 4]. However, implementing measures to reduce cooling loads usually needs to be considered during the design phase of new construction [5, 6]. And since less-efficient cooling units are usually found in lower-income homes, upgrading air conditioners in older homes often causes financial issues. Thus, less-efficient air conditioning units have been running for decades. For example, from the Residential Energy Consumption Survey data released in 2015 by the EIA, more than 18% of the air-conditioning equipment used in the nation's 103 million homes were more than 15 years old [7].

The objective of this study was to develop simple and cost-effective methods for improving the cooling efficiency of pre-existing air conditioning systems. In order to improve heat transfer and reduce cooling load, misting the condenser of split air conditioners and controlling window blinds automatically based on sunlight were proposed. Experiments were carried out to evaluate the proposed methods, and results were demonstrated and analyzed.

Methods

Air conditioners use energy to transport heat out of the relatively cool interior of a house to the relatively warm environment outside the house. Figure 1 shows that air conditioners are made of two separate coils, an indoor evaporator, an outdoor condenser, and a compressor to circulate the refrigerant through the system. When the compressed liquid refrigerant passes through the evaporator, it evaporates and removes the heat out of the indoor air; it then carries the heat to the condenser. When the refrigerant vapor has been condensed to liquid, it will release the heat to the outside air. The proposed approach was to install a misting system that could cover the condenser with mist when needed, so that it can work together with the condenser fan to further reduce the temperature of the condenser coils (see again Figure 1). The proposed method applies to central air conditioning systems, as they are more efficient than room air conditioners and are in wide use [7].

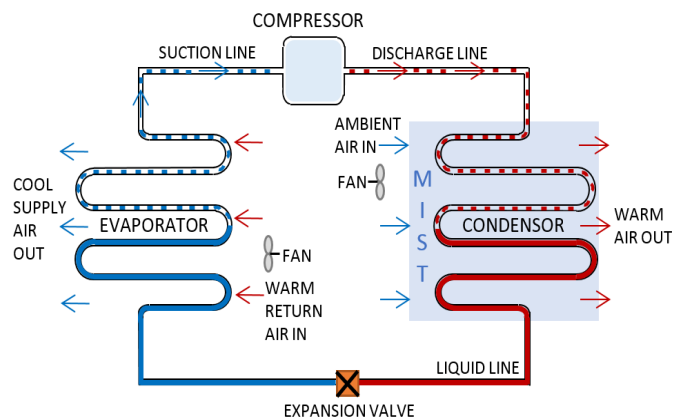


Figure 1. Using Mist to Improve Heat Transfer

Misting System

Figure 2 illustrates the design of a miniature house with the proposed misting system in a full-scale actual residential air conditioning unit [8]. The proposed method uses rain water to mist the condenser. Rain water collected from the eave spout of the house flows through the down spout and into the lidded sump basin installed underground. A piece of gutter guard was installed on the eave spout to clear out leaf litter and trash from the water flow. The sump basin has an outlet for routing the overflow water in order to maintain the needed water level. Then, the rain water is cleansed by filters and pumped into a tube to create mist covering the condenser through nine nozzles around the condenser.



Figure 2. Miniature House Model

A battery set, charged through a solar panel attached on the roof, provides power to the pump. Figure 3 shows how the filters, the pump, and the battery were placed in a waterproof housing. The proposed system is a self-sufficient system, since it uses rain water and a solar panel. After initial installation, follow-up investment is not needed for the misting system.

Automatically Controlled Blinds

In addition to air conditioning, other alternatives can also cool down the house. For example, proper shading can reduce the sunlight shining through windows, especially east and west windows. Sunlight adds the largest amount of unwanted heat in the summer, which may raise the interior temperature of a typical house as much as 20°F [9]. Using horizontal trellises above east and west windows to provide effective shading is the best way to eliminate solar heat gain [9]. A set of automatically controlled window blinds was installed to reduce the cooling load. Figure 4 shows how the blind set is controlled by a DC motor to raise and lower the blinds, and a continuous-rotation servo motor to adjust the angle of the blinds. A photocell measures the amount of

sunlight, and the signal is used to operate the blinds. The blind set is controlled by an Arduino microcontroller and powered by a 5V battery and a 12 battery, which are charged by the solar panel. Figure 5 illustrates the control diagram. The automatically controlled window blinds can also be a part of a smart house, as they are connected wirelessly through a web server on a PC through XBee units and controlled via the Internet.



Figure 3. Waterproof Housing of Filters, Pump, and Battery

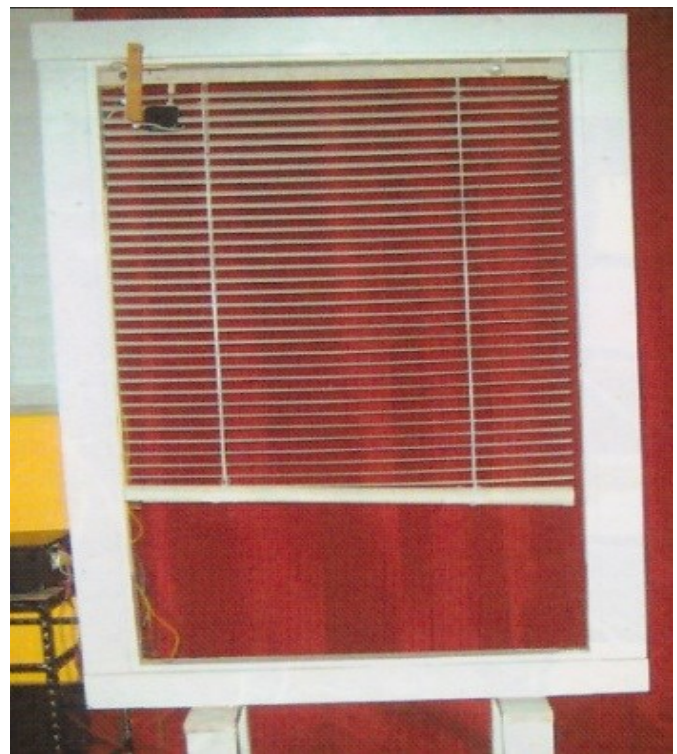


Figure 4. Automatically Controlled Window Blinds

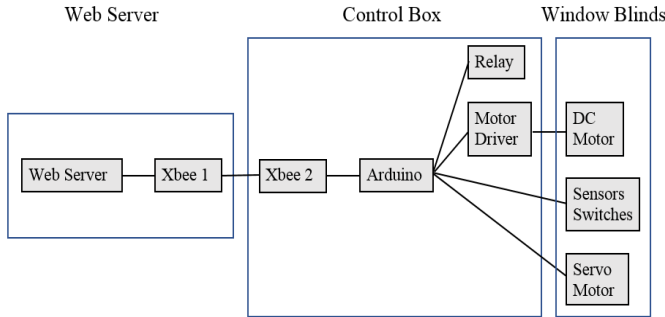


Figure 5. Control Diagram for Window Blinds

Experiment

The air conditioning unit was a 5000-Btu window air conditioner, which was dismantled and reconstructed as a real-life split-system air conditioning unit. The window air conditioner was separated into the condenser coil and the evaporator coil, and the tubing between them was extended so that the evaporator could be installed inside the house and the condenser could be placed outside [10].

Various sensors were installed to verify the operation of the misting unit, including temperature, humidity, pressure, current, and flow-rate sensors. LabVIEW was used to collect the data from the various sensors. Six type-J thermocouples were placed along the liquid line, the suction line, and on the condenser to record the corresponding temperatures. Two humidity sensors were installed on the evaporator to measure the humidity change of the air coming in and out as the system runs. A pressure sensor was embedded in the liquid line to measure the pressure of the R22 refrigerant. A current sensor measured the current drawn by the system in order to determine energy consumption. A digital flow meter indicated the amount of water used during each trial of the misting operation. A Graphtec GL220 data logger processed the sensor inputs, and transmitted the data to LabVIEW through a USB connection.

Figure 6 illustrates the electrical diagram of the output control. A National Instruments multifunction DAQ device, USB 6008, was utilized to output the control signals and control both the misting system and the air conditioning system through two relays. LabVIEW determined the digital output of the USB 6008. Figures 7 and 8 show how LabVIEW simulated a house thermostat and allowed a set temperature to be predefined. Based on the current room temperature, the program would activate the air conditioning system to run until the set temperature was reached. After the air conditioning started running, the misting system could be turned on. A float switch determined if the water level was safe before activating the pump to create the mist.

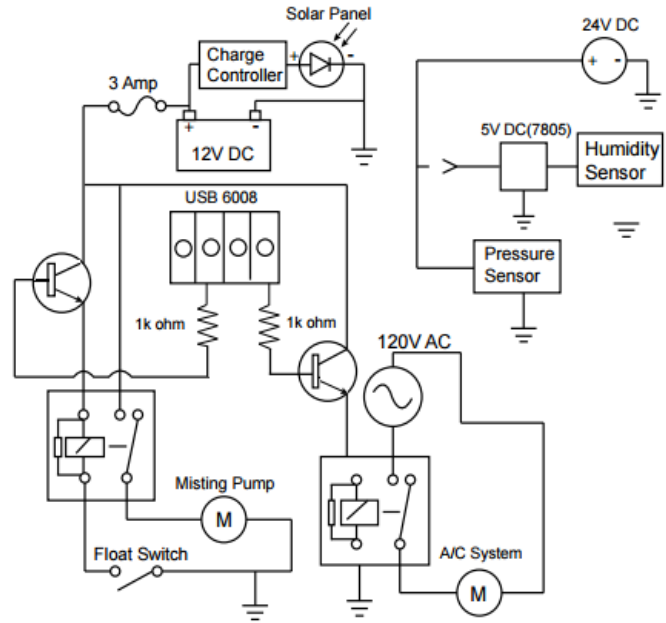


Figure 6. Electrical Diagram of Air Conditioning Using Mist

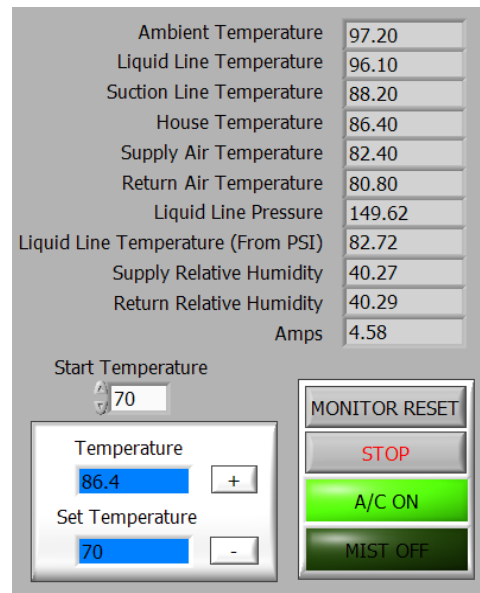


Figure 7. Front Panel of the LabVIEW Program

The experiments were carried out under consistent conditions in order to verify the misting operation. Before each trial run, the air conditioning unit ran for 10 minutes to allow the R22 refrigerant to circulate through the system. A heater was turned on and increased the ambient and house temperatures to 110°F, after which there was a pause of 20 minutes for the temperature to be stabilized. Then, the trial run without mist was started, and the air conditioning system was activated until the predefined temperature—65°F

energy. This was verified by the power calculated, based on the reading of the current sensor. Without mist, the power consumed increased steadily from 266 watts to 288 watts. With mist, the power was kept at 250 watts.

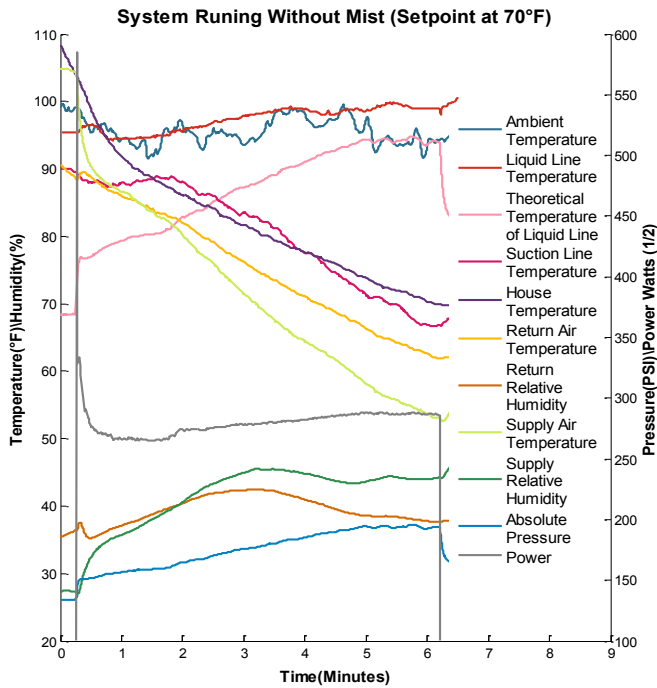


Figure 9. Recorded Sensor Data without Using Mist

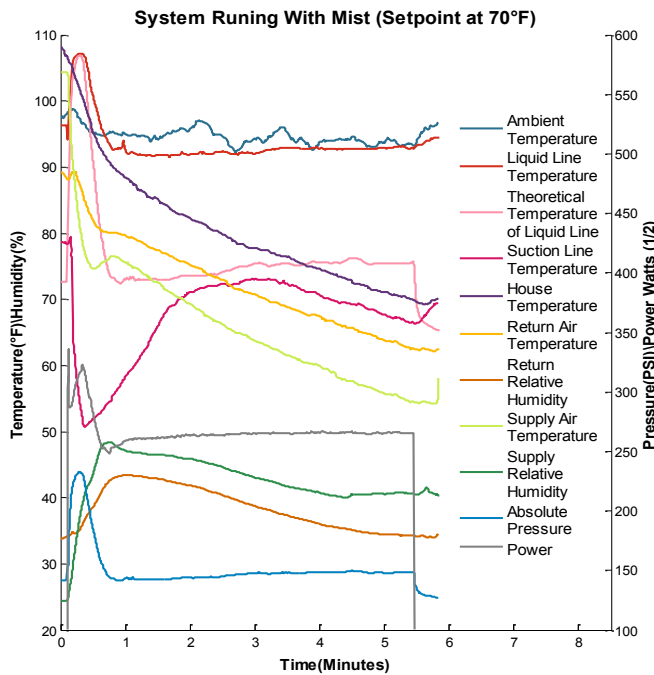


Figure 10. Recorded Sensor Data Using Mist

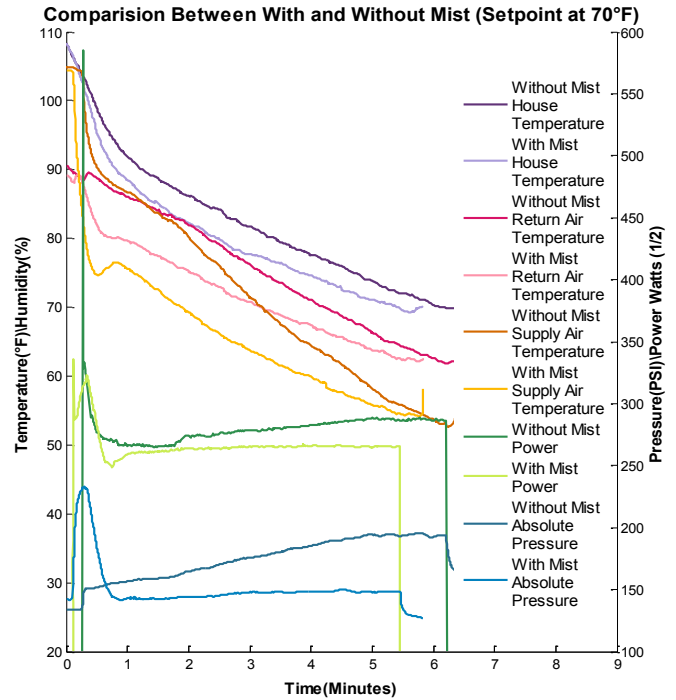


Figure 11. Comparison of Sensor Data

From the experimental results, implementing the misting system can improve the efficiency of an air conditioning system. To lower the temperature from 110°F to 70°F in less than six minutes, the misting system can reduce run time by 13%, reduce system pressure by 15%, and reduce energy consumption by 5%. In the long run, using the misting system can save energy costs for home owners and reduce carbon dioxide emissions, due to the operation of air conditioning systems. The proposed system is self-sufficient, simple, and cost effective. After the first installation, little or no maintenance was needed. In this study, the experiments were carried out on a miniature house model, and the experimental time was relatively short for the automatically controlled window blinds to produce the desired effect. In the future, experiments will be carried out on a real-life residential cooling system over a longer time period, so that both the misting system and the automatically controlled window blinds can improve the heat transfer and reduce the cooling load.

References

- [1] Energy Information Administration (US). (2017). *Annual Energy Outlook 2017: With Projections to 2050*. Government Printing Office.
- [2] Air Conditioning. (n.d.). Retrieved from <https://energy.gov/energysaver/air-conditioning>

-
- [3] Pisello, A. L., Santamouris, M., & Cotana, F. (2013) Active Cool Roof Effect: Impact of Cool Roofs on Cooling System Efficiency. *Advances in Building Energy Research*, 7(2), 209-221.
- [4] Ya, Y., Lia, Z. W., Ho, Z. J., & Zho, X. J. (2004). Optimal Operation of a Large Cooling System Based on an Empirical Model. *Applied Thermal Engineering*, 24(16), 2303-2321.
- [5] Aktacir, M. A., Büyükalaca, O., & Yılmaz, T. (2010). A Case Study for Influence of Building Thermal Insulation on Cooling Load and Air-conditioning System in the Hot and Humid Regions. *Applied Energy*, 87(2), 599-607.
- [6] Yang, L. N., & Li, Y. G. (2008). Cooling Load Reduction by Using Thermal Mass and Night Ventilation. *Energy and Buildings*, 40(11), 2052-2058.
- [7] Residential Energy Consumption Survey (RECS). (2015). Retrieved from <https://www.eia.gov/consumption/residential/data/2015/>
- [8] Li, M., Abatan, A., Robinson, D., Weller, J., & Bello, M. (2017). Improving Energy Efficiency of Pre-existing Home Cooling Systems. *ICCE-25, 25th Annual International Conference on Composite and Nano Engineering*. Rome, Italy.
- [9] Cooling Systems. (n.d.). Retrieved from <http://www.smarterhouse.org/home-systems-energy/cooling-systems>
- [10] American Society of Heating, Refrigerating and Air-Conditioning Engineers. (2009). 2009 ASHRAE handbook: Fundamentals. Atlanta, GA: American Society of Heating, Refrigeration and Air-Conditioning Engineers.

University. Mr. Robinson may be reached at robinsdc@muohio.edu

JEFF WELLER received his bachelor's degree from the Department of Engineering Technology at Miami University. Mr. Weller may be reached at weljef7897@hotmail.com

MATTHEW BELLO received his bachelor's degree from the Department of Engineering Technology at Miami University. Mr. Bello may be reached at bellomm@muohio.edu

Biographies

MING LI is an assistant professor in the Department of Computer Science, Engineering and Physics at University of Michigan-Flint. She earned her PhD from Florida International University. Her research interests include mechatronics, robotics, and structural health monitoring. Dr. Li may be reached at minglilm@umflint.edu

AYO ABATAN is chair and professor in the Department of Engineering Technology at Miami University. He received his PhD in civil engineering from Virginia Polytechnic Institute and State University and his MS in civil engineering from University of Illinois. His research interests include structural health monitoring, smart structures, and analysis of composites. Dr. Abatan may be reached at abatanao@miamioh.edu

DERICK ROBINSON received his bachelor's degree from the Department of Engineering Technology at Miami

USING NANOPARTICLES TO MODIFY THE SURFACE ENERGY OF HIGH-DENSITY POLYETHYLENE FILMS

Rex C. Kanu, Purdue Polytechnic Institute; Thomas Spotts, Ball State University

Abstract

In the plastics, packaging, and printing industries, it is known that printing on high-density polyethylene (HDPE) films is very difficult, because of the smearing of printing inks on HDPE films. The printing problem is attributed to the low surface energy of HDPE films (~30 dynes/cm or ~30 mN/m) compared to that of the printing inks (36–44 dynes/cm or 36–44 mN/m). Thus, considerable efforts have been made to improve the surface energy of HDPE films by flame, corona treatments, and, in some instances, by the addition of inorganic additives such as talc to HDPE films. However, flame and corona treatments remain the primary methods of improving the surface energy of HDPE films in the plastics, packaging, and printing industries. In studies that used inorganic additives to improve the surface energy of HDPE films, researchers observed that the smaller the particle size of the additives, the greater the improvements of the films' surface energy. Since the particle sizes used in these studies were in the micron range (μm or 10^{-6} meters), the authors of this current study proposed that further reduction of the additives' particles sizes to the nanometer range (nm or 10^{-9} meters) might offer additional improvement in the surface energy of HDPE films. Therefore, nanoparticles of montmorillonite clay and graphene oxide (GO) were used in this study. It was expected that this method of modifying the surface energy of HDPE films would not only reduce or eliminate the need for secondary processes—such as flame and corona treatments—but would also increase the tensile strength of the HDPE films, since nanoparticles would also act as reinforcing agents.

Introduction

Polymers, such as polyethylene (PE, which is used here to represent low-density polyethylene, LDPE; high-density polyethylene, HDPE; and linear-low-density polyethylene, LLDPE) and polypropylene (PP) are used in packaging applications, because these materials are inexpensive when compared to paper, metal, or glass. They are also easier to work with and require less energy to process. Figure 1 shows an HDPE packaging application. Despite the advantages that polymers have over other materials in packaging applications, it is known that some commercial polymer

films are difficult to print on or to place adhesive labels on them because of their relatively low surface energy [1-5].



Figure 1. An HDPE Milk Jug

Given the problem of the relatively low surface energy of these films, it is important to improve their surface energy, if printing on them is to be successful. The current methods of increasing the films' surface energy include corona treatment [6, 7] or flame treatment [8]. Other methods that have been used to improve the surface energy of these materials include coatings [4], surface control additives [9]—which are used to lower the surface tension of the printing inks—and polymer additives [1, 10, 11], which are incorporated into the polymer films to increase their surface energy. Regarding additives, Ruiz [5] observed that the addition of 20 wt.% of $1\mu\text{m}$ APS (average particle size) of calcium carbonate to LLDPE films raised their surface energy from 32 dynes/cm² (3.2 N/m²) to 38 dynes/cm² (3.8 N/m²). Arina and Honkanen [11]—while working with talc, mica, and clay—observed that these additives increased the surface energy, and thereby the printability of polyethylene (PE) films. Furthermore, they observed that the surface energy of PE films increased from 32 dyne/cm (mN/m) to 37 dyne/cm (mN/m) by increasing the additive content from 0 to 57 wt.%, while simultaneously decreasing the additives' particle sizes. The particle sizes they worked with were within the range of 1 μm to 74 μm . In this current study, the authors chose to further examine the effects of particle size and weight percent (wt.%) content of additives on surface energy of polyethylene films by using nanoparticles, which are about 1000 times smaller than the micro-sized particles

used in previous studies [10, 11]. The commercial nanoparticles used in this study were Cloisite 20A (natural montmorillonite clay modified with a quaternary ammonium salt) and graphene oxide nanoparticles. Of the two types of nanoparticles, most of the graphene oxide nanoparticles contained polar functional groups such as hydroxyl (–OH), carbonyl (–C=O), and carboxylic (–COOH).

Theory

The mechanisms by which corona and flame treatments increase the surface energy of the polymer films are not well known [1, 12]. It has been proposed that these treatments “roughens the films’ surface, which provides sites for mechanical interlocking, introduces reactive sites on the polymer/plastic films’ surface [13], consequently increasing the wettability and reactivity of the surface” [12]. The functionalities suspected to be introduced to the polymer’s surface include carbonyl, hydroxyl, hydro-peroxide, aldehyde, ether, ester, and carboxylic acid groups. The mechanism of how commercial additives such as calcium carbonate, talc, and clay particles change the surface energy of the polymer/plastic films is not well understood but may be similar to the mechanism described for corona and flame treatment. Specifically, it is suspected that the polar nature of the carbonyl group of calcium carbonate increases the surface energy of polymer/plastic films.

Film Wetting or Wettability

Film wetting (wettability) is defined as the replacement of adherent air at the film surface by a liquid coating or ink material [9]. Without good wetting, it is very difficult to achieve good quality printing. Consequently, it is important to use films that have good wetting properties. This is done by measuring the contact angle, α , of a liquid drop placed on a film under static conditions. Complete wetting of a film occurs when α is zero or close to zero, while partial wetting occurs when the contact angle is greater than zero but less than 90° ($0^\circ < \alpha < 90^\circ$) [14]. Good wetting also equates to a film having a relatively high surface energy, as expressed by Young’s equation [15] [(see Equation (1))] that relates contact angles to interfacial surface energy between the film and ink (liquid).

Equation (1) is used to show graphically in Figure 2 how the contact angle of water on PE films would vary as a function of the surface energy of PE film. Using Equation (1), it was assumed that literature values of the surface energy of PE films (solid, γ_{sv}) equaled 31.6 dyne/cm (mN/m), the surface energy of water (liquid, γ_{lv}) equaled 72.8 dyne/cm (mN/m), and the interfacial surface energy between the solid and the liquid values (γ_{sl}) equaled 39.2 dyne/cm (mN/m)

at a contact angle of 96° [16]. It was further assumed that surface energy of water and the interfacial surface energy between water and the PE film remained in contact as a worst-case scenario. Based on these assumptions, Figure 2 suggests that by increasing the surface energy of PE films, the contact angle of water on PE films decreases, consequently improving wettability and printability of PE films.

$$\text{Cosine}(\theta) = \frac{\gamma_{sv} - \gamma_{sl}}{\gamma_{lv}} \quad (1)$$

where, θ is the contact angle; γ_{sv} is the surface tension of the solid in air; γ_{sl} is the surface tension of the liquid in air; and, γ_{lv} is the interfacial surface tension of the solid and liquid.

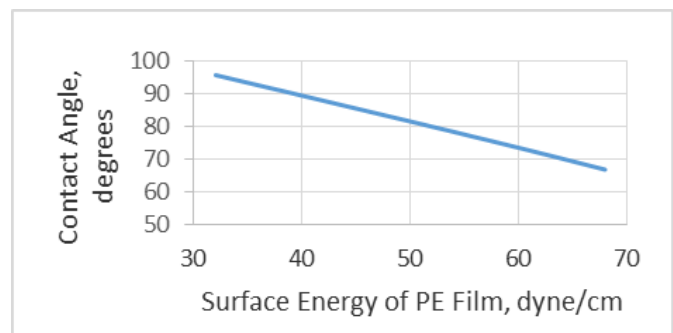


Figure 2. Estimated Contact Angle of Water on PE Film Using Young’s Equation

Experimentation

The authors used two methods to prepare the HDPE films: melt blending and solution film casting. The materials used in the melt blending method included high-density polyethylene (HDPE), and Sclair 19C by NOVA Chemicals used to make the PE film. This polymer was described by the manufacturer as a film extrusion-grade HDPE with a melt-flow index (MI) of 0.95 g/10 min at 190 °C/2.16 kg. The additives used in this melt blending method were the Cloisite 20A (Cly) and Cloisite Na⁺ nanoparticles manufactured by Southern Clay Products. These particles were natural montmorillonite clay, modified with a quaternary ammonium salt, and used as purchased. According to the materials’ specifications, “montmorillonites have a sheet-type or plate-type structure. Although their dimensions in the length and width directions can be measured in hundreds of nanometers, the mineral’s thickness is only one nanometer” [17]. Cloisite Na⁺ nanoparticles (A125 and B250) were also used to increase the presence of polar groups at the film surface. Anhydride Polybond (PB), 3009 and 3029 HDPE/Maleic Anhydride, supplied by Chemtura Corporation, were used to promote the bonding of the nanoparticles to the HDPE matrix.

A paint shaker was used to mix the formulation of HDPE, polybond, and nanoparticles in a gallon paint can for 30 minutes before introducing the mixture into a Brabender counter-rotating twin-screw extruder for melt blending. The extrudates from the extruder were pelletized and introduced into a Brabender blown-film extruder with a mini-tower. The surface energies of the blown films produced were measured using a contact angle goniometer, Tantec model CAM-MICRO and Accudyne test pens. The materials used in the solution film casting method included generic high-density polyethylene (HDPE) powder (purchased from an industrial arts supply company) used in making the PE film by solution casting. The HDPE powder was a rotational molding grade, but was used in this study to facilitate the dissolving of PE in the solvents. The solvents were N, N'-dimethylformamide (DMF), and ortho-dichlorobenzene (ODCB). The additive used with this method was graphene oxide (GO) nanoparticles purchased from Sigma-Aldrich (catalogue #796034-1G). GO sheets are about 1nm (1×10^{-9} m) in thickness and were supplied in layers containing 10-15 sheets [18]. The GO nanoparticles were edge-oxidized [19] and were used as purchased.

Based on the work of Bhattacharyya et al. [20], 1 wt.% of GO (this is based on the weight of HDPE) was exfoliated and dispersed in DMF and ODCB (1:4 ratio of solvent mixture) with a Branson 2200 ultrasonic machine for 30 minutes and then stirred for one hour. This was followed by adding a small amount of HDPE to the solvent mixture at 140°C, while stirring continued until the HDPE was dissolved. Small amounts of HDPE were subsequently added at appropriate intervals until all of the HDPE was dissolved. The dispersion contained a total of 3% HDPE (on a w/v of total solvents used). For control purposes, HDPE, without the GO nanoparticles, was processed similarly. Both the HDPE solutions and HDPE-GO dispersions were cast into films and dried at 70°C for several hours.

Results

Tables 1-3 show the results of this work. Table 1 shows that the formulation of 80/10/10 wt.% of HDPE/Polybond (PB)/Cloisite 20A (Cly) increased the surface energy of HDPE by about 5.3 dynes/cm (5.3 mN/m), while other formulations showed a decrease in the surface energy of HDPE. When these measurements were repeated using Accudyne pens, no difference in surface energy of the films was observed. The authors were not able to explain the difference in these results, except to suggest that further work is required to elucidate this difference. However, based on repeated measurements, it appeared that the Accudyne pens provided more consistent results than contact-angle measurements. Figure 3 illustrates the use of the Accudyne pens

to determine the surface energy of films. If the ink does not "ball up" (form small beads on the surface of the film) after three seconds of drawing a smooth line on the surface of the film, it indicates that the film has a surface energy equal to or greater than that of the pen. A pen with a greater surface energy was used to repeat the process until the ink balls up. When the ink balls up, a pen whose surface energy is lower than the previously used pen (balled-up ink) was used to repeat the process and, if the current pen does not ball up, the film was assigned that surface energy.

Table 1. Contact Angle Measured with Tantec

Material (wt.%)	Contact Angle	Surface Energy (dyne/cm)	Difference (dyne/cm)
HDPE	81±12	34.4	---
HDPE/PB (80/20)	87±17	30.3	-4.1
HDPE/PB/Cly (80/10/10)	72.4±4.8	39.7	5.3
HDPE/PB/A125 (82.5/8.75/8.75)	87±13	30.4	-4.0
HDPE/PB/B250 (85/7.5/7.5)	82.4±3.5	33.4	-1.0

Table 2. Surface Energy Estimated with Accudyne Pens

Materials (wt.%)	Surface Energy (dyne/cm)	Difference
HDPE	32	----
HDPE/PB/Cly (80/10/10)	32	None
HDPE/PB/A125 (82.5/8.75/8.75)	32	None

Table 3. Surface Energy Estimated with Accudyne Pens

Materials (wt.%)	Surface Energy (dyne/cm)	Difference (dyne/cm)
HDPE (control)	32	----
HDPE/GO (99/1)	36	4
HDPE/GO (95/5)	38	6

For example, if a pen whose surface energy is 30 dyne/cm (30 mN/m) does not ball up, another pen whose surface energy is 32 dyne/cm (32 mN/m) is tried on the film. If this pen does not ball up, then another pen whose surface energy is 34 dyne/cm (34 mN/m) is tried. If the ink from this pen balls up, then the pen with the lower surface energy of 32 dyne/cm (32 mN/m) is tried again on the film's surface.

And if it does not ball up, then the film is assigned a surface energy of 32 dyne/cm (32 mN/m). Standard Accudyne pens are calibrated from 30 dyne/cm to 60 dyne/cm in 2-dyne/cm increments, while non-standard Accudyne pens are calibrated from 31 dyne/cm to 61 dyne/cm in 2-dyne/cm increments, and in 1-dyne/cm increments from 62 dyne/cm to 70 dyne/cm.



Figure 3. Illustration of the Use of an Accudyne Pen

Table 3 shows that the addition of 1 wt.% and 5 wt.% of graphene oxide nanoparticles improved the surface energy of HDPE film by 4 dyne/cm (4 mN/m) and 6 dyne/cm (6 mN/m), respectively. These results seem reasonable, given the greater surface energy of graphene oxide (GO) films relative to those of HDPE films reported by Wang et al. [15] in their study of the wettability and surface energy of graphene films. They reported that graphene and graphene oxide films had surface energies of 46.7 dyne/cm (46.7 mN/m) and 62.1 dyne/cm (62.1 mN/m), respectively. Therefore, the addition of 1 wt.% and 5 wt.% of GO to HDPE films resulted in increases in the surface energy of the HDPE/GO films, when compared to that of the HDPE film that was used as a control.

Conclusions

In this study, the authors examined the use of nanoparticles to increase the surface energy of HDPE films based on two hypotheses: (1) the smaller-sized nanoparticle additives will provide greater increases in surface energy of HDPE films than would micro-sized particles used in previous studies [10, 11], and (2) the introduction of polar groups—such as hydroxyl(-OH), carbonyl (-C=O), and carboxylic (-COOH)—to HDPE films will increase their surface energy. The results provided in Tables 1 and 2 do not support the former hypothesis, because the current results were inconsistent across the methods used to measure the surface

energy of the films. However, the results in Table 2 clearly show that incorporating clay nanoparticles at 8.75 and 10 wt.% did not increase the surface energy of HDPE films. The results in Table 3 strongly suggest that the presence of polar groups in GO nanoparticles increased the surface energy of HDPE films. These findings are supported by the work of Wang et al. [15], which showed that GO films have greater surface energy than graphene films, and the main difference between the films is the presence of polar groups in the GO nanoparticles.

References

- [1] Phokhaphaiboonsuk, D. L., Jarupan, L., Pechyen, C., & Nandhivajrin, C. (2012). Surface treatment on low density polyethylene with TiO₂ nanoparticles for packaging printing. *Advanced Materials Research*, 506, 615-618.
- [2] Arkles, B. (2006). Hydrophobicity, hydrophilicity and silanes. *Paints and Coatings Industry*, 1-10.
- [3] Grundke, K., Azizi, M., Ziemer, A., Michel, S., Pleul, D., Simon, F., et al. (2005). Hyperbranched polyesters as potential additives to control the surface tension of polymers. *Surface Coatings International Part B: Coatings Transactions*, 88(2), 101-106.
- [4] Chen, B. (1997). Surface properties of corona-treated polyethylene films containing N-(2-hydroxyethyl) erucamide as slip agent for enhanced adhesion of water-based ink. *Polymers, Laminations, and Coatings Conference*, 427-438.
- [5] Ruiz, F. A. (1996). Modifying film conversion and end-use characteristics with mineral reinforcement. *Polymers, Laminations, and Coatings Conference Proceedings*, 1-4.
- [6] Corona treatment and surface modifications. (n.d.). Retrieved from <http://www.dynetechnology.co.uk/applications/corona>
- [7] Before and after corona treatment. (n.d.). Retrieved from <http://www.dynetechnology.co.uk/Images/DBImages/Products/315.JPG>
- [8] The Surface Flame Treatment System for Extrusion and Converting Lines and Automotive Industry. (n.d.). Retrieved from <http://www.flametreaters.com/company>
- [9] Surface control additives. (n.d.). Retrieved from <http://www.deltaspwll.com/Delta%20PDF/SC.pdf>
- [10] Murthy, N. S., Kotliar, A. M., Sibilgia, J. P., & Sacks, W. (1986). Structure and Properties of talc-filled polypropylene and nylon 6 films. *Journal of Applied Polymer Science*, 31(8), 2569-2682.
- [11] Arina, M., & Honkanen, A. (1979). Mineral fillers in low-density polyethylene films. *Polymer Engineering and Science*, 19(1), 30-39.

-
- [12] Lahti, J., & Tuominen, M. (2007). The effects of corona and flame treatment: Part 1. PE-LD Coated packaging. *11th European Tappi PLACE Conference Athens*, 1-15.
- [13] Polymer surface modifications. (n.d.). Retrieved from <http://www.ekasuga.co.jp/en/product/185/000232.shtml>
- [14] Contact angles and wettability. (n.d.). Retrieved from <http://www.plastix-world.com/cold-plasma-improves-bonding>
- [15] Wang, S., Zhang, Y., Abidi, N., & Cabrales, L. (2009). Wettability and surface free energy of graphene films. *Langmuir*, 25(18), 11078-11081.
- [16] Critical Surface Tension and Contact Angle with Water for Various Polymers. (n.d.). Retrieved from https://www.accudynetest.com/polytable_03.html
- [17] Polymer Grade Montmorillonites. (n.d.). Retrieved from http://www.nanocor.com/tech_sheets/G105.pdf
- [18] Schniepp, H. C., Li, J., McAllister, M. J., Sai, H., Herrera-Alonso, M., Adamson, D. H., et al. (2006). Functionalized Single Graphene Sheets Derived from Splitting Graphite Oxide. *J. Phys. Chem. B*, 110(17), 8535-8539.
- [19] Graphene oxide, Aldrich 796034. (n.d.). Retrieved from <http://www.azom.com/article.aspx?ArticleID=11433>
- [20] Bhattacharyya, A., Chen, S., & Zhu, M. (2014). Graphene reinforced ultra-high molecular weight polyethylene with improved tensile strength and creep resistance properties. *EXPRESS Polymer Letters*, 8(2), 74-84.

interests include product color appearance, the comparison of electronic and paper documents, and package printing. Dr. Spotts may be reached at tspotts@bsu.edu

Biographies

REX C. KANU is an assistant professor of Mechanical Engineering Technology at Purdue Polytechnic Institute. He earned his BS in Chemical Engineering from Northeastern University, MS in Chemical Engineering from the University of Connecticut, SM in Management Science from Massachusetts Institute of Technology, and his PhD in Polymer Science from the University of Connecticut. Dr. Kanu is currently teaching at Purdue Polytechnic Institute. His research interests include polymer nanocomposites, polymer blends, and plastics processing. Dr. Kanu may be reached at rkanu@purdue.edu

THOMAS SPOTTS is an associate professor of technology at Ball State University. He earned his BS degree from The Ohio State University, his MS in printing technology from Rochester Institute of Technology, and his PhD in educational technology from Michigan State University. He currently teaches in the Graphic Arts Management Program at Ball State University. His research

INSTRUCTIONS FOR AUTHORS: MANUSCRIPT REQUIREMENTS

The INTERNATIONAL JOURNAL OF ENGINEERING RESEARCH AND INNOVATION is an online/print publication designed for Engineering, Engineering Technology, and Industrial Technology professionals. All submissions to this journal, submission of manuscripts, peer-reviews of submitted documents, requested editing changes, notification of acceptance or rejection, and final publication of accepted manuscripts will be handled electronically. The only exception is the submission of separate high-quality image files that are too large to send electronically.

All manuscript submissions must be prepared in Microsoft Word (.doc or .docx) and contain all figures, images and/or pictures embedded where you want them and appropriately captioned. Also, for all accepted manuscripts, each figure, image, or picture that was imported into your Word document must be saved individually as a **300dpi or higher JPEG (.jpg)** file and submitted separately; your manuscript and figure numbers must be used in the title of the file (e.g., **J13-F-18 Figure 4**); that means one additional file for each image imported into your manuscript. These 300dpi images do NOT need to be embedded in your manuscript. For tables or graphs created directly in Word, you do not need to submit them as separate files.

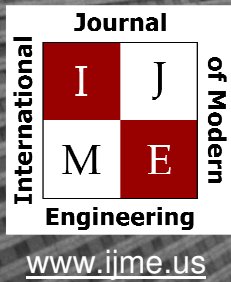
Included below is a summary of the formatting instructions. You should, however, review the [sample Word document](http://www.ijeri.org/formatting_guidelines) on our website (www.ijeri.org/formatting_guidelines) for details on how to correctly format your manuscript. The editorial staff reserves the right to edit and reformat any submitted document in order to meet publication standards of the journal.

The references included in the References section of your manuscript must follow APA-formatting guidelines. In order to help you, the sample Word document also includes numerous examples of how to format a variety of scenarios. Keep in mind that an incorrectly formatted manuscript will be returned to you, a delay that may cause it (if accepted) to be moved to a subsequent issue of the journal.

1. **Word Document Page Setup:** Two columns with $\frac{1}{4}$ " spacing between columns; Top of page = $\frac{3}{4}$ "; Bottom of page = 1" (from the top of the footer to bottom of page); Left margin = $\frac{3}{4}$ "; Right margin = $\frac{3}{4}$ ".
2. **Paper Title:** Centered at the top of the first page with a 22-point Times New Roman (Bold), Small-Caps font.
3. **Page Breaks:** Do not use page breaks.
4. **Body Fonts:** Use 10-point Times New Roman (TNR) for body text throughout ($\frac{1}{8}$ " paragraph indentation); 9-point TNR for author names/affiliations under the paper title; 16-point TNR for major section titles; 14-point TNR for minor section titles; 9-point TNR BOLD for caption titles for tables and figures; other font sizes as noted in the sample document.
5. **In-text Referencing:** List and number each reference when referring to them in the body of your document (e.g., [1]). The first entry must be [1] followed by [2], [3], etc., continuing in numerical order to the final entry in your References section. Again, see the sample Word document for specifics. Do not use the End-Page Reference utility in Microsoft Word. You must manually place references in the body of the text.
6. **Tables and Figures:** Center all tables and figures. Captions for tables must be above the table, while captions for figures are below; all captions are left-justified.
7. **Page Limit:** Manuscripts should not be more than 15 pages (single-spaced, 2-column format).
8. **Page Numbering:** Do not use page numbers.
9. **Publication Charges:** Manuscripts accepted for publication are subject to mandatory publication charges.
10. **Copyright Agreement:** A Copyright Transfer Form must be signed and submitted by all authors on a given paper before that paper will be published.
11. **Submissions:** All manuscripts and associated files must be submitted electronically.

MANUSCRIPTS should be submitted to Dr. Philip D. Weinsier, manuscript editor, at philipw@bgsu.edu along with a copy to editor@ijeri.org.

FILES containing your high-quality images should **ONLY** be submitted to philipw@bgsu.edu.



Print ISSN: 2157-8052
Online ISSN: 1930-6628



INTERNATIONAL JOURNAL OF MODERN ENGINEERING

ABOUT IJME:

- IJME was established in 2000 and is the first and official flagship journal of the International Association of Journal and Conferences (IAJC).
- IJME is a high-quality, independent journal steered by a distinguished board of directors and supported by an international review board representing many well-known universities, colleges and corporations in the U.S. and abroad.
- IJME has an impact factor of **3.00**, placing it among the top 100 engineering journals worldwide, and is the #1 visited engineering journal website (according to the National Science Digital Library).

OTHER IAJC JOURNALS:

- The International Journal of Engineering Research and Innovation (IJERI)
For more information visit www.ijeri.org
- The Technology Interface International Journal (TIIJ).
For more information visit www.tiij.org

IJME SUBMISSIONS:

- Manuscripts should be sent electronically to the manuscript editor, Dr. Philip Weinsier, at philipw@bgsu.edu.

For submission guidelines visit
www.ijme.us/submissions

TO JOIN THE REVIEW BOARD:

- Contact the chair of the International Review Board, Dr. Philip Weinsier, at philipw@bgsu.edu.

For more information visit
www.ijme.us/ijme_editorial.htm

INDEXING ORGANIZATIONS:

- IJME is indexed by numerous agencies.
For a complete listing, please visit us at www.ijme.us.

Contact us:

Mark Rajai, Ph.D.

Editor-in-Chief
California State University-Northridge
College of Engineering and Computer Science
Room: JD 4510
Northridge, CA 91330
Office: (818) 677-5003
Email: mrajai@csun.edu



www.tiij.org



www.ijeri.org

The International Journal of Engineering Research & Innovation (IJERI) is the second official journal of the International Association of Journals and Conferences (IAJC). IJERI is a highly-selective, peer-reviewed print journal which publishes top-level work from all areas of engineering research, innovation and entrepreneurship.



IJERI Contact Information

General questions or inquiries about sponsorship of the journal should be directed to:

Mark Rajai, Ph.D.

Founder and Editor-In-Chief

Office: (818) 677-5003

Email: editor@ijeri.org

Department of Manufacturing Systems Engineering & Management

California State University-Northridge

18111 Nordhoff St.

Room: JD3317

Northridge, CA 91330